GNSS high accuracy algorithms and techniques for Energy domain

EASY-AAL-D3.1

Prepared by
Bilal Muhammad, Marco Nisi, Fabio Menichetti, Alberto Mennella, Graziano Gagliarde, Rosario Di Lascio, Antonio Greco, Davide Marenchino
Verified by
Ernestina Cianca
Approved by
Marco Nisi

Company	
Aalborg University	AALBORG UNIVERSITY DENMARK

DOCUMENT STATUS SHEET

EDIZ.	DATE	§ - CHANGES	AUTHOR
1.0	30/05/2016	Issue 1.0	Bilal Muhammad
1.1	11/07/2016	Issue 1.1, updates as per [AD 2] (PDR)	Bilal Muhammad Marco Nisi
2.0	30/09/2016	Updated Section 4.2, Experimental Results	Bilal Muhammad
2.1	21/11/2016	Issue 2.1, updates as per [AD 3] (CDR)	Bilal Muhammad Marco Nisi
3.0	31/01/2017	Issue 3.0 generating a new document structure by merging version 2.1 of this document with a TN about the end-to-end EASY PV algorithm. In particular, the following main updates are performed ✓ Update of Chapter 1, introduction, where explanation about the new document structure is provided and justified ✓ Creation of Chapter 2 and 3, where the complete end to end algorthm is explained and a focus on computer vision is provided ✓ Chapter 4 and 5 represents the former chapter 2 and 3 with no changes ✓ Chapter 6 has been created to include expected sources of error ✓ Chapter 7 has been created to include experimental tests also including GNSS activities where preliminary outcomes relevant to EDAS and Galielo are also provided ✓ Update of Chapter 8, conclsion.	Bilal Muhammad Marco Nisi Fabio Menichetti Alberto Mennella Graziano Gagliarde Rosario Di Lascio Antonio Greco Davide Marenchino
3.1	03/03/2017	Updates as per [AD 5] (MTR)	Marco Nisi

EDIZ.	DATE	§ - CHANGES	AUTHOR
3.2	30/6/2017	Updates (relevant to TRR) of section 7 "Experimental activties" to include improvement on: ✓ TEST_GSD.0010 (finalised) ✓ TEST_GIM.0010 (on going) ✓ TEST_SEN.0010 (finalised) ✓ TEST_VIS.0010 (finalised) ✓ TEST_GNSS.0060 (on going) ✓ TEST_GNSS.0070 (on going)	Bilal Muhammad Marco Nisi Alberto Mennella
3.3	30/10/2017	Deleted test TEST_GNSS.0070 as focused on CORS network which are experienced not to be interesting due to their low availability. Finalised ✓ TEST_GIM.0010 (section 7.2) ✓ TEST_GNSS.0060 (section 7.5.7) Sections 7.5.7 and 7.6 as well as conclusion (chapter 8.) are updated accordingly Section 7.6 hs been introduced to provide a summary about the end to end performances including all sources of errors	Bilal Muhammad Marco Nisi Alberto Mennella

EDIZ.	DATE	§ - CHANGES	AUTHOR
3.4	22/12/2017	Implemented changes as discussed during AR meeting: All document. ✓ "GNSS module" replaced with "Panel Tracking module" ✓ Section 5.1.5. Added Receiver North RTKite Section 7.2.1 ✓ Removed test session with geodetic measurement performances; the test has been replaced by a second session based on a different approach (see section 7.2.1.2) Section 7.5.1 and 7.5.2 ✓ Objective rephrased to state that precision is not in the scope of the tests and only accuracy is evaluated. Section 7.5.4 ✓ Removed statement where further tests on Galileo receivers are performed as the current target receiver does not include phase measurements of Galileo itself Section 7.5.6 ✓ Presented new results about comparison between single frequency and dual frequency in cinematic conditions Section 7.6 ✓ pointed out each error in a dedicated column in the table Section 8. Conclusions updated accordingly	B. Muhammad

TABLE OF CONTENTS

LIST OF FIGURES

LIST OF TABLES

1 INTRODUCTION

This section provides a description of the core Algorithm, where GNSS info are integrated with Computer Vision techniques to be implemented in EASY-PV project on RPAS/ RGS subsystems.

1.1 SCOPE

This document provides the description of the end to end EASY-PV algorithm aiming at automating the overall process of maintenance, by using an RPAS equipped by a high accuracy GNSS receiver as well as other equipment for computer vision analysis, so that at the end the maintainer is able to know the right defective panel affected by anomalies.

To this purpose high accuracy provided by GNSS is the key enabling technology as the defective panel is straightforwardly identified by comparing the position of a geo-referenced defective panel with the RPAS high accuracy positioning.

The current issue is the one delivered for AR milestone, to support the EASY system design and implementation of the final EASY-PV system including identification of the used configuration and the choice of the EASY PV GNSS receiver.

1.2 APPLICABLE DOCUMENTS

ID	Title
[AD 1]	GRANT AGREEMENT NUMBER - 687409 - EASY PV (25/11/2015)
[AD 2]	RDS of EASY-UNIA-D3.1 (PDR)
[AD 3]	RDS of EASY-UNIA-D3.1 (CDR)
[AD 4]	RDS of EASY-UNIA-D3.1 Annex (CDR)
[AD 5]	RDS of EASY-UNIA-D3.1 (MTR)

Table 1-1: Applicable Documents

1.3 REFERENCE DOCUMENTS

ID	Title
[RD 1]	http://www.ftexploring.com/solar-energy/tilt-angle2.htm
[RD 2]	http://www.gogreensolar.com/pages/solar-panel-tilt-calculator
[RD 3]	http://www.flir.com/suas/content/?id=70728
[RD 4]	http://developer.dji.com/
[RD 5]	http://navspark.mybigcommerce.com/s2525f8-bd-rtk-evb-rtk-module-evaluation-board/
[RD 6]	https://www.u-blox.com/en/product/c94-m8p
[RD 7]	D2.1 - User Needs, Operational Concepts and System Requirements document

ID	Title
[RD 8]	EASY-SIST-D5.2 EASY PV platform Architecture Design
[RD 9]	EASY-UNIA-D3.2-Test and Verification Campaign Methodology
[RD 10]	EASY-AAL-D9.1-Test and Verification Campaign Report
[RD 11]	Unmanned Rotorcraft Systems, Advances in Industrial Control, Springer-Verlag London Limited 2011 - cap 2: Coordinate Systems and Transformations
[RD 12]	Ed Williams, Aviation Formulary (http://williams.best.vwh.net/avform.htm#LL)
[RD 13]	Vincenty T, Direct and inverse solutions of geodesics on the ellipsoid with application of nested equations(https://www.ngs.noaa.gov/PUBS_LIB/inverse.pdf)
[RD 14]	C. F. F. Karney, Algorithms for geodesics (http://dx.doi.org/10.1007/s00190-012-0578-z)
[RD 15]	Charles Karney, GeographicLib (http://geographiclib.sourceforge.net/)
[RD 16]	MySQL Spatial Relation Functions (http://dev.mysql.com/doc/refman/5.7/en/spatial-relation-functions-object-shapes.html)
[RD 17]	PostGIS Spatial Relationships and Measurements (http://postgis.net/docs/manual-2.2/ST_Contains.html)
[RD 18]	Hughes, William J. "Global positioning system (GPS) standard positioning service (SPS) performance analysis report." *Tech. Cntr. NSTB/WAAS T and E Team* 87 (2014)
[RD 19]	SOLSDD, EGNOS. "EGNOS Safety of Life Service Definition Document. "*European Commission, Directorate-General for Enterprise and Industry* (2014)
[RD 20]	Petovello, M. How do you compute relative position using GNSS? , Insidegnss, GNSS Solutions, May/June 2011.
[RD 21]	Realini, E. "goGPS-free and constrained relative kinematic positioning with low cost receivers." Politecnico di Milano (2009).
[RD 22]	Novatel, Precise Positioning with NovAtel CORRECT Including Performance Analysis", *Novatel White Paper,* 2015
[RD 23]	Takac, Frank, and Oliver Zelzer. "The relationship between network RTK solutions MAC, VRS, PRS, FKP and i-MAX. "*Proceedings of ION GNSS 2008*: 348-355
[RD 24]	Vollath, Ulrich, et al. "Network RTK versus single base RTK–understanding the error characteristics." *Proceedings of the 15th International Technical Meeting of the Satellite Division of the Institute of Navigation, Portland, Oregon, USA*. 2002
[RD 25]	Laurichesse, D., F. Mercier, and J. P. Berthias. "Zero-difference integer ambiguity fixing on single frequency receivers." Proceedings of ION ITM-2009, Anaheim (2009): 26-28.
[RD 26]	Standard, R. T. C. M. "10403.2." Differential GNSS (Global Navigation Satellite Systems) Services–Version 3.
[RD 27]	Dettmering, Denise, and Georg Weber. "The EUREF-IP Ntrip Broadcaster: Real-time GNSS data for Europe." *Proceedings of the IGS2004 Workshop, Astronomical Institute University of Bern, Switzerland*. 2004
[RD 28]	Weber, Georg, et al. "Networked transport of RTCM via internet protocol (Ntrip)-IP-streaming for real-time GNSS applications." *ION GNSS 18th International Technical Meeting of the Satellite Division*. 2005
[RD 29]	SDD, EDAS. "EGNOS Data Access Service (EDAS) Service Definition Document. *European Commission, Directorate-General for Enterprise and Industry* (2014)

ID	Title
[RD 30]	T. Vincenty, "Direct and Inverse Solutions of Geodesics on the Ellipsoid with Application of Nested Equations," Survey review, vol. 23, no. 176, pp. 88–93, 1975.
[RD 31]	C. F. Karney, "Algorithms for Geodesics," Journal of Geodesy, vol. 87, no. 1, pp. 43–55, 2013. [5] K. Kraus, Photogrammetry. Ferdinand Dummlers Verlag, 1993, vol. 1.
[RD 32]	C. F. Karney,, Photogrammetry. Ferdinand Dummlers Verlag, 1997, vol. 2.
[RD 33]	M. Cramer, "Performance of gps/inertial solutions in photogrammetry," 2001.
[RD 34]	H. P. VC, "Method and means for recognizing complex patterns," Dec. 18 1962, US Patent 3,069,654.
[RD 35]	C. Mongrdien, J.-P. Doyen, M. Strom, and D. Ammann, "CentimeterLevel Positioning for UAVs and Other Mass-Market Applications," in Proceedings of the 29th International Technical Meeting of the Satellite Division of the Institute of Navigation (ION GNSS+), Portland, Oregon, 2016.
[RD 36]	C. Bruyninx, "The euref permanent network: a multi-disciplinary network serving surveyors as well as scientists," GeoInformatics, vol. 7, no. 5, pp. 32–35, 2004.
[RD 37]	Multi-object tracking using color, texture and motion. Takala, V., & Pietikainen, M. s.l. : IEEE Conference on Computer Vision and Pattern Recognition, 2007, Vol. (pp. 1-7).
[RD 38]	Finding trajectories of feature points in a monocular image. I.K. Sethi, R. Jain. 1987, IEEE Trans. Pattern Anal. Mach. Intell. 9, p. 56-73.
[RD 39]	Establishing motion correspondence. K. Rangarajan, M. Shah. 1991, Computer Vision and Pattern Recognition (CVPR), p. 56-73.
[RD 40]	Real-time closed-world tracking. J.W.D. Stephen S. Intille, A.F. Bobick. IEEE Conf. on Computer Vision and Pattern Recognition, p. 697-703.
[RD 41]	W4: Real-time surveillance of people and their activities. I. Haritaoglu, D. Harwood, L.S. David. 2000, IEEE Trans. Pattern Anal. Mach. Intell. 22, p. 809-830.
[RD 42]	Multi-object tracking using dynamical graph matching. Hwann-Tzong Chen, Horng-Horng Lin, T.-L. Liu. 2001, Proc. of the IEEE Conf. on Computer Vision and Pattern Recognition, p. 210-217.
[RD 43]	You'll never walk alone: Modeling social behavior for multi-target tracking. S. Pellegrini, A. Ess, K. Schindler, L. van Gool. 2009, IEEE 12th International Conference on Computer Vision, p. 261-268.
[RD 44]	Robust multiperson tracking from a mobile platform. A. Ess, B. Leibe, K. Schindler, L. van Gool. 2009, IEEE Trans. Pattern Anal. Mach. Intell. 31, p. 1831-1846.
[RD 45]	Pedestrian detection and tracking in infrared imagery using shape and appearance. C. Dai, Y. Zheng, X. Li. 2007, Comput. Vis. Image Understand. 106, p. 288-299.
[RD 46]	Homography based multiple camera detection and tracking of people in a dense crowd. R. Eshel, Y. Moses. 2008, IEEE Conference on Computer Vision and Pattern Recognition, p. 1-8.
[RD 47]	A novel multi-planar homography constraint algorithm for robust multi-people location with severe occlusion. X. Tong, T. Yang, R. Xi, D. Shao, X. Zhang. 2009, Fifth International Conference on Image and Graphics, p. 349-354.
[RD 48]	Tracking multiple occluding people by localizing on multiple scene planes. S. Khan, M. Shah. 2009, IEEE Trans. Pattern Anal. Mach. Intell. 31, p. 505-519.
[RD 49]	Real-time tracking of non-rigid objects using mean shift. D. Comaniciu, V. Ramesh, P. Meer. 2000, Proc. of the IEEE Conf. on Computer Vision and Pattern Recognition, p. 142-149.

ID	Title
[RD 50]	Object tracking with bayesian estimation of dynamic layer representations. H. Tao, H. Sawhney, R. Kumar. 2002, IEEE Trans. Pattern Anal. Mach. Intell. 24, p. 75-89.
[RD 51]	Detection of multiple, partially occluded humans in a single image by Bayesian combination of Edgelet part detectors. B. Wu, R. Nevatia. 2005, Tenth IEEE Int. Conf. on Computer Vision, p. 90-97.
[RD 52]	Edgelet based human detection and tracking by combined segmentation and soft decision. K. Bhuvaneswari, H. Abdul Rauf. 2009, International Conference on Control, Automation, Communication and Energy Conservation, p. 1-6.
[RD 53]	Combined feature evaluation for adaptive visual object tracking. Z. Han, Q. Ye, J. Jiao. 2011, Comput. Vis. Image Understand. 115, p. 69-80.
[RD 54]	Detecting and tracking people in a homogeneous environment using skin color model. B. Yogameena, S. Roomi, S. Abhaikumar. 2009, Seventh International Conference on Advances in Pattern Recognition, p. 282-285.
[RD 55]	Vision-based multiple interacting targets tracking via on-line supervised learning. X. Song, J. Cui, H. Zha, H. Zhao. 2008, Proceedings of the 10th European Conference on Computer Vision, p. 642-655.
[RD 56]	A new algorithm for robust pedestrian tracking based on manifold learning and feature selection. M. Wang, H. Qiao, B. Zhang. 2011, IEEE Trans. Pattern Anal. Mach. Intell. 12, p. 1195-1208.
[RD 57]	Automatic extraction of moving objects from uav-borne monocular images using multi-view geometric constraints. M. Kimura, R. Shibasaki, X. Shao, and M. Nagai. 2014, International Micro Air Vehicle Conference and Competition.
[RD 58]	Motion-based object segmentation using hysteresis and bidirectional inter-frame change detection in sequences with moving camera. M. G. Arvanitidou, M. Tok, A. Glantz, A. Krutz, and T. Sikora. s.l. : Signal Processing: Image Communication, 2013, Vol. 28.
[RD 59]	Robust global motion estimation oriented to video object segmentation. B. Qi, M. Ghazal, and A. Amer. s.l. : IEEE Transactions on Image Processing, 2008, Vol. 17.
[RD 60]	A human motion estimation method using 3-successive video frames. Minoh, Y. Kameda and M. s.l. : International conference on virtual systems and multimedia, 1996.
[RD 61]	Moving object detection and tracking from video captured by moving camera. W.C. Hu, C.H. Chen, T.Y. Chen, D.Y. Huang, and Z.C. Wu. s.l. : Journal of Visual Communication and Image Representation, 2015.
[RD 62]	A computational approach to edge detection. Canny, J. s.l. : IEEE Transactions on pattern analysis and machine intelligence, 1986, Vol. 679-698.
[RD 63]	Takasu, T. "RTKLIB: An open source program package for GNSS positioning." 2013-04-29)[2014-03-25]. http://www. rtklib. com (2011)
[RD 64]	Donahue, Brian. Guidelines for RTK/RTN GNSS Surveying in Canada. Natural Resources Canada, 20
[RD 65]	O'Keefe, Kyle. Single Versus Multiple: How Frequencies Make a Difference in GNSS Receivers. InsideGNSS, September 2016

ID	Title
[RD 66]	Cécile Mongrédien et alias, u-blox Switzerland, " Centimeter-Level Positioning for UAVs and Other Mass-Market Applications", Proceedings of the 29th International Technical Meeting of the ION Satellite Division, ION GNSS+ 2016, Portland, Oregon, September 12-16, 2016
[RD 67]	NORTH Surveying and Positioning Systems 'GNSS RTK RTKite Receiver', http://northsurveying.com/Datasheets/North%20RTKite%20GNSS%20RTK%20Receiver%202016%20EN.pdf

Table 1-2 Reference Documents

1.4 ACRONYMS

Acronym	Description
AGC	Automatic Gain Control
APC	Antenna Phase Center
API	Application Program Interface
ARMA	Auto Regressive Moving Average Model
C&C	Communication and Control
CCD	Charge Coupled Device
CEP	Circular Error Probable
CG	Centre of Gravity
CORS	Continuously Operating Reference Station
COTS	Commercial Off-The-Shelf
CP	Contact Point
CPS	Central Processing System
DB	Data Base
DGPS	Differential GPS
DRMS	Distance Root Mean Square
EDAS	EGNOS Data Access Service
EGNOS	European Geostationary Navigation Overlay Service
EMC	Electro Magnetic Compatibility
EPN	EUREF Permanent Network
EUREF	European Reference Frame
EUREF-IP	EUREF Internet Protocol
EWAN	EGNOS Wide Area Network
FKP	Flachen Korrektur Parameter
FMU	Flight Management Unit
FOV	Field Of View

Acronym	Description
FPS	Frames Per Second
GEO	Geostationary Earth Orbit
GLONASS	Globalnaya Navigazionnaya Sputnikovaya Sistema, or Global Navigation Satellite System is Russion version of GPS
GNSS	Global Navigation Satellite System
GPS	Global Positioning System
GPU	Graphical Computer Unit
GS	Ground Speed
GSD	Ground Sample Distance
HSPA	High Speed Data Access
HTTP	Hypertext Transfer Protocol
IMU	Inertial Measure Unit
KPI	Key Performance Indicator
MCC	Mission Control Centre
MSAS	Multifunction Transport Satellite Augmentation System
NAVCOM	NAVigation and integrated COMmunication
NDGPS	North America DGPS
NED	North East Down
NLES	Navigation Land Earth Station
NRTK	Network RTK
NTRIP	Networked Transport of RTCM via Internet Protocol
OBC	On Board Computer
OEM	Original Equipment Manufacturer
OOP	Object Oriented Paradigm
OS	Open Service
PCS	Panel Cross Section
PIC	Pilot in Command
PPM	Part Per Million
PPP	Precise Point Positioning
QZSS	Quasi Zenith Satellite System
RGS	RPAS Ground Station
RIMS	Ranging and Integrity Monitoring Station
RMS	Root Mean Square
RPAS	Remotely Piloted Aircraft System
RTCM	Radio Technical Commission for Maritime Services
RTK	Real Time Kinematic
S/S	Sub System

Acronym	Description
SBAS	Satellite Based Augmentation System
SDCM	System for Differential Correction and Monitoring
SDK	Software Development Kit
SoL	Safety of Life
TIR	Thermal Infra Red
UHF	Ultra High Frequency
UMTS	Universal Mobile Telecommunication System
VHF	Very High Frequency
VRS	Virtual Reference Station
WP	Work Package

Table 1-3: Acronyms

1.5 DOCUMENT STRUCTURE

The document includes the following sections:

- ✓ Section 2 illustrates the end to end algorithm, pointing out the importance of GNSS and computer vision technologies and providing the technical reference for further implementation;
- ✓ Section 3 focuses on Computer vision techniques which are in particular used for panel detection and tracking along with data collecting.
- ✓ Section 4 focuses on GNSS. It outlines the key performance indicators for selecting a high accuracy GNSS solution to aid RPAS operation in identifying the defective panel. Various GNSS solutions, which meet the RPAS accuracy requirements as per SR.0210 mentioned in [RD 8], are discussed taking in to account the operational complexity and technological challenges.
- ✓ Section 5 includes a market survey of various GNSS receiver manufacturers and GNSS error correction service provider aiming to suggest a final receiver brand and configuration.
- ✓ Section 6 provides the system error sources assessment, where preliminary outcomes are issued for each critical EASY PV component
- ✓ Section 7 supports considerations analysed in section 6 by reporting experimental activities also performed with a real RPAS on-field for algorithm application feasibility. Section 7 and 6 also provides recommendations to be used for EASY-PV platform development.
- ✓ Finally, Section 8 summarises the conclusion of this experimental activity.

2 END TO END EASY-PV ALGORITHM

This section provides a description of the core Algorithm, where GNSS info are integrated with Computer Vision techniques to be implemented in EASY-PV project on RPAS / RGS subsystems.

2.1 GNSS & COMPUTER VISION FUSION

The experience of PV thermal inspections acquired on field by TopView with PV_WATCH service (thermal inspections with manual anomalies recognition and manual report analysis – no automation) complements the user's needs provided in EASY-PV from an operational point of view, when RPAS are involved in flight operations.

Figure 2-1: RPAS TOPVIEW APIS 550 during thermal inspections

Medium size PV plant (1,2 MW) may contain over 3.000 PV panels to be inspected; state-of-the-art and affordable thermal cameras available on the market do not exceed a resolution of 640 x 480 pixels.

Therefore, the target height of RPAS for thermal inspection results in a trade-off among different items such as:

- ✓ The number of PV Panels covered by the SWATH of the Camera;
- ✓ The GSD achievable (cm/pixel) especially when lower resolutions cameras are used (e.g. 336x254 pixels);
- ✓ The image deformation introduced when a short focal length optic is used;
- ✓ The time needed for inspections.

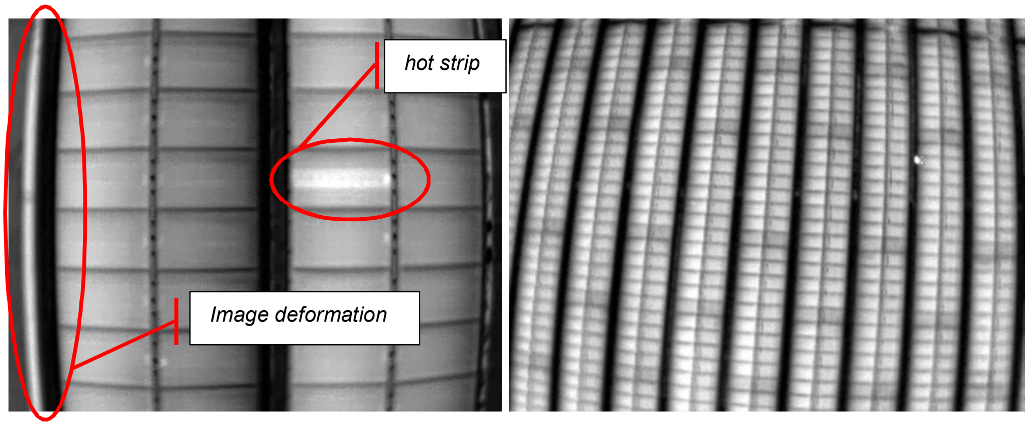

Figure 2-2: Thermal images captured by RPAS at different heights:hot strip visible (LEFT); hot strip not visible (RIGHT)

In Figure 2-2 (LEFT) it is shown a hot-strip thermal anomaly as specified in EASY-PV User's needs document (D2.1). The hot strip can be recognized at lower height (RPAS closer to the Panels), but it cannot be recognized at higher height (RIGHT) because of the greater GSD (more centimeter per pixel). Moreover, flying at low height with short focal length optics (e.g. 6.8 mm as in Figure 2-2-LEFT) introduces image distortion that is acceptable for manual inspections, but it is not for automatic shapes recognition to be used in image processing analysis.

Maximizing the number of Panels falling over the camera SWATH with reasonable resolution on ground, lowering distortions issues, is the first steps towards automation. The importance of one unique identifier for each Panel, based on its precise position is evident when it is not possible to obtain from the images acquired, any reference ground points or geometric recognizable shapes from the PV plant geometry.

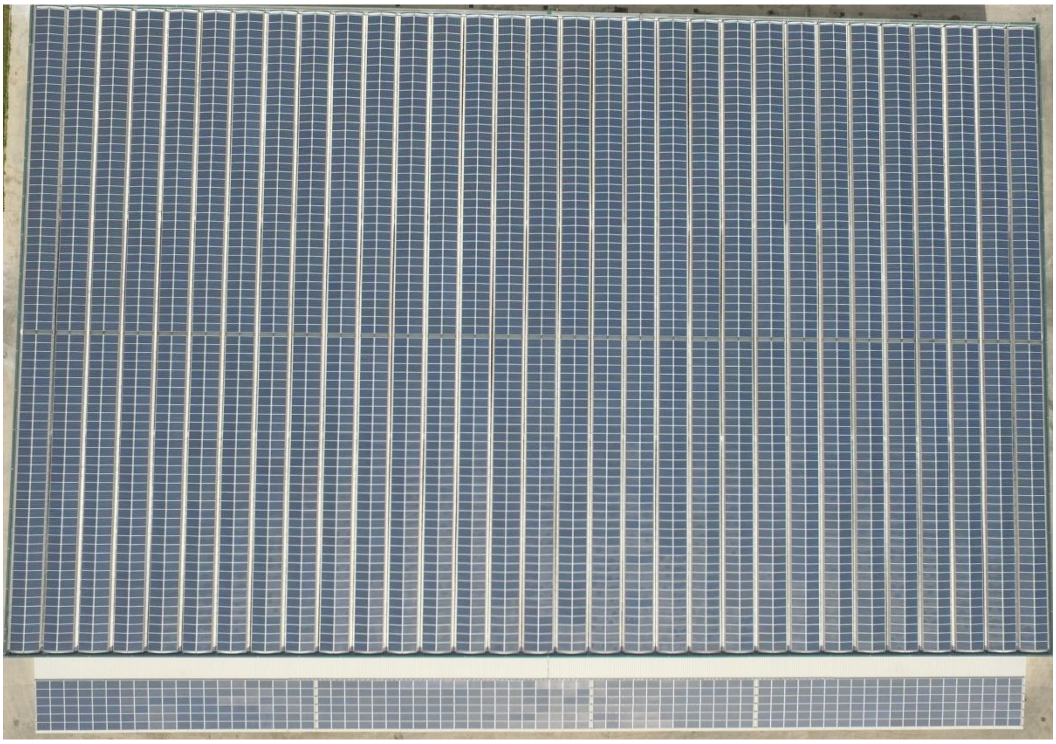

Figure 2-3: "Lo Uttaro" PV Plant (Caserta - South Italy) - nadiral optical view

Figure 2-3 shows a nadiral optical view of “Lo Uttaro” PV plant (Caserta - South Italy); a PV Plant owned by one of the stakeholders interested in EASY-PV projects outcomes. It is very easy to “get lost” during RPAS inspections, therefore RPAS Pilot and RPAS ground crew have to implement different strategies to enhance the probability to identify the precise panel affected by anomaly during inspections.

In PV planimetry like the one in Figure 2-3 the best strategy is to count PV plant’s raws and columns (composed by Panels) from the beginning for each flight (due to battery change). This simple strategy is the best operational technique for thermal inspections implemented manually by RPAS operators. However, PV plants may have many different configurations and layouts, therefore this strategy cannot always be applied.

High accuracy and precision are required to assign to each panel horizontal coordinates precise enough to allow unambiguously its identification/detection. Such capability is needed to enhance PV inspections for all kind of PV Plants with different kind of geometry factors and planimetry.

Other aspects such as inclination of modules, sun position, reflexes and shadows are also very important issues [RD 7] to be taken into account as confirmed by on-field operations experience.

The choice of a WGS-84 geographic coordinates system is one of the possible choices justified by some simplification in software development and configuration (e.g. using C/C++ GeographicLib [RD 15]). In principle a local relative reference system could be also used, introducing a new configuration parameter for EASY-PV system, taking into account also the local datum used for each PV plant of the network.

Given the importance of one unique identifier for each PV panel related to each panel’s horizontal position, it is essential to identify and investigate the feasibility of following aspects:

- ✓ The Reference systems that will be adopted;
- ✓ The Algorithm idea and its logical steps including I/O variables and transformation functions;
- ✓ The possible sources of error to make the algorithm application affordable before any development;
- ✓ A preliminry feasibility provided with internal on-field tests;
- ✓ A draft SW design of the core function of the algorithm with envisiged SW COTS and SW libraries available.

2.2 COORDINATE REFERENCE SYSTEMS

Reference systems are introduced to handle the data required by the algorithm with respect of the "producer" unit of the information (Drone, Payload or Payload Sensors).

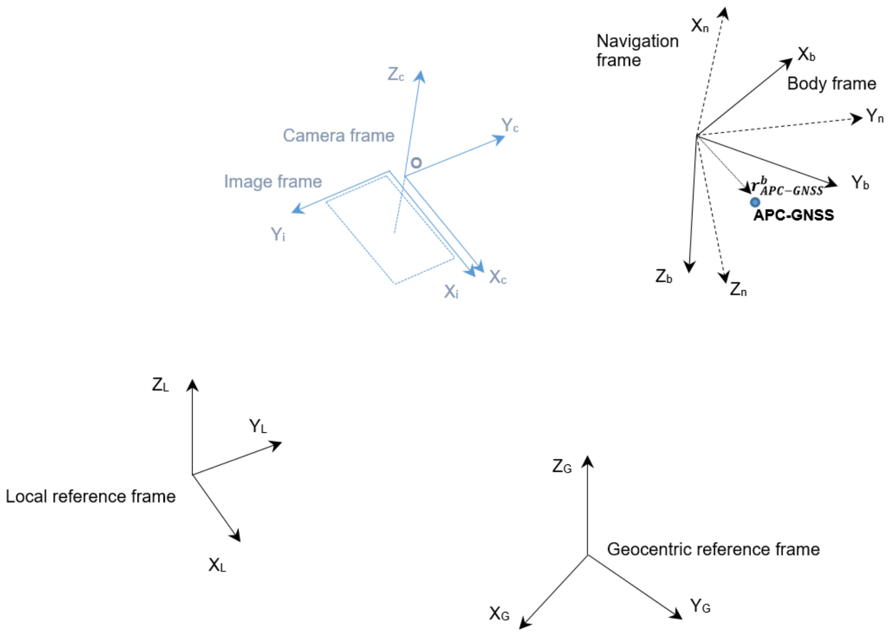

Figure 2-4: frames involved in the algorithm

The reference systems involved in the procedure are:

- ✓ **Geocentric reference frame**. It is the frame in which the GNSS provides the coordinates. The following geodetic frames are possible to be used
  - o WGS 84 datum. Applicable to GPS;
  - o PZ-90 datum applicable to Glonass;
  - o CGCS2000 datum applicable to Beidou;
  - o GTRF datum applicable to Galileo

A proper transformation will be applied in the receiver to take into account all the above references in case of multiconstellation solution.

- ✓ **Navigation frame**. It is a local tangential system and it represents the second reference frame to which the body frame rotation matrix are referred. This system is defined as a cartesian frame with origin at the IMU (Inertial Measure Unit) instrumental centre and orientation according to NED convention:
  - Origin at IMU instrumental centre;
  - X_n axis (North axis) directed from origin to Earth's geographic North;
  - Y_n axis (East axis) perpendicular to N axis directed from origin to Earth's geographic East;
  - Z_n axis (Down axis) perpendicular to N and E axis directed towards Earth.

- ✓ **Body frame**. It is fixed with respect to the drone axis and it is used as internal reference system to describe RPAS attitude (Heading, Elevation and Banking) and orientation. This system is usually materialized by IMU sensor, which is installed in the RPAS. Moreover, it is the first reference frame to which the IMU rotation matrix are referred.

It is identified as having:
- Origin at IMU instrumental centre;
- X_b axis (roll axis), longitudinal, passing through drone "nose" to "tail" in the plane of symmetry of the drone;
- Z_b axis (yaw axis) perpendicular to the X_b axis, in the plane of symmetry of the aircraft, positive below the drone;
- Y_b axis (pitch axis), perpendicular to the X_b Z_b plane, positive determined by the right-hand rule (generally, positive out the right wing).

For the sake of completeness, it is noteworthy that also a **GNSS BODY reference system** is used, which is translated (with no rotation) to the above BODY frame as centred in the GNSS antenna phase centre (APC-GNSS in the figure). The offset of APC-GNSS from Body frame origin is a vector called $r^b_{APC-GNSS}$

✓ **Local reference frame. It is also called object reference system**. It is a local tangential Cartesian reference system (eulerian plan), with the origin is usually located in the surveyed area.
- Origin in a point defined by the operator;
- X_L axis (East axis) perpendicular to Y_L axis directed from origin to Earth's geographic East;
- Y_L axis (North axis) perpendicular to X_L axis directed from origin to Earth's geographic North;
- Z_L axis (Elevation axis) perpendicular to X_L and Y_L axis directed upward.

✓ **Image frame**. This is a 2 - dimension reference system, located in the sensor plane (CCD plane), it has origin in the upper left corner of image X_i axis direct toward right side and Y_i axis direct downward in the image plane.

✓ **Camera frame**. It is the frame which defines the image space. The origin of this frame is in the projection centre of camera *O*, X_c, Y_c axes are parallel to image frame axes, Z_c axis is perpendicular to the sensor plane and directed upward.

2.3 EASY PV CORE ALGORITHM

The EASY-PV core algorithm merges high accuracy GNSS techniques with computer vision algorithms largely used in literature (from [RD 37] to [RD 62]) for fixed camera processing.

The algorithm is the core of the system and has in charge the analysis of all panels of the PV plant with the aim of detecting possible thermal anomalies and create a data base of all panels. The algorithm shall be able to recognize the PV panels of a PV plant and assign them an unique identifier, related to its WGS-84 geographical coordinates.

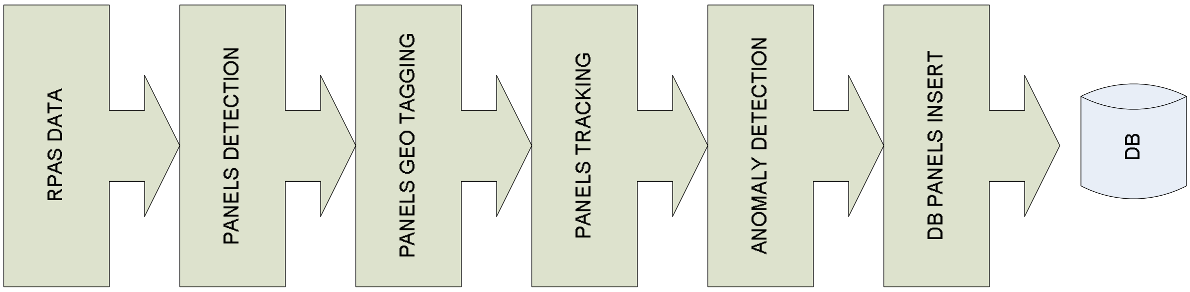

Figure 2-5: Core Algorithm functions

In Figure 2-6 are represented the working spaces of the algorithm and the significant transformations. The variables used as input for the algorithm and the internal software structures created are intended to work in the Spaces described.

- ✓ **(X,Y) Space** is the space of the Pixels with respect to the CCD reference system previously defined.
- ✓ **(φ,λ) Space** is the space of the geographic coordinates with respect of both NED and BODY reference system.

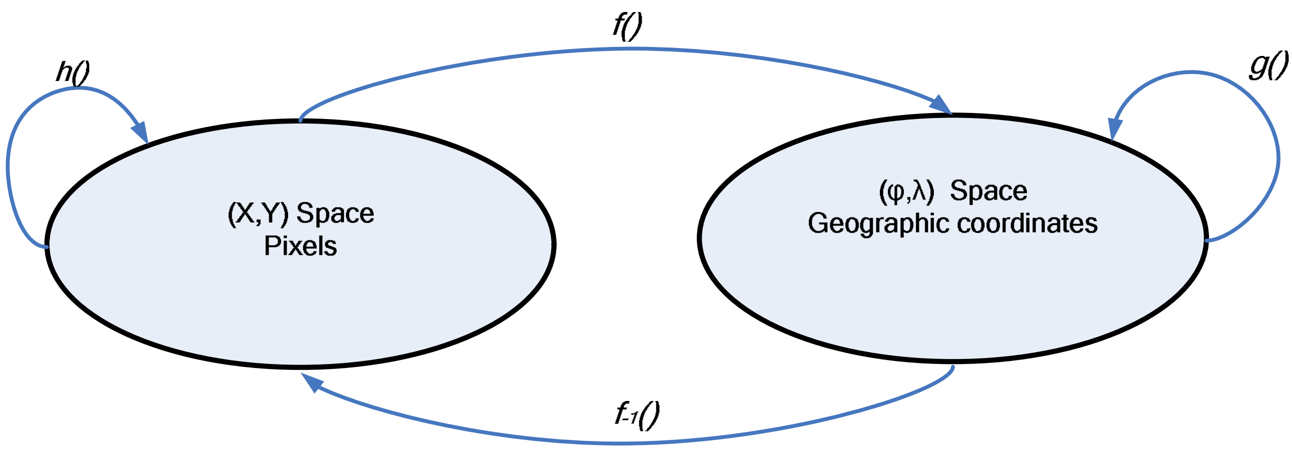

Figure 2-6: EASY-PV Core Algorithm Spaces and transformations

The two spaces defined are linked with three functions:

- ✓ **function h():** The function h is responsible for panels shape recognition, detection and tracking;
- ✓ **function f():** allows the transformation of an array of (X,Y) points in (φ,λ) points and vice-versa by means of $f^{-1}()$ inverse function
- ✓ **function g():** generates for each Panel a center in WGS-84 coordinates (φ,λ), providing one unique identifier for each panel.

As specified in §2.2, the **(X,Y)** Space represents the 2 dimensional space expressed in pixels (CCD reference system). The point O(0,0) is the centre of the camera; the generic point P1(0,320) is the last pixel on the **Y** axis for a FLIR TAU2 640x480 pixel camera. The **(φ,λ)** Space represents WGS-84 geographic coordinates with respect to WGS84 geodetic system.

2.3.1 $\boldsymbol{h}()$ FUNCTION

The *h()* function is responsible for panel shape and anomalies recognition (i.e.: shape detection) in **X,Y**. In particular it needs the variables $\boldsymbol{\alpha}, \mathbf{h}$ (slant angle, RPAS height) in input to work:

$$Array[Panels] = h(\boldsymbol{\alpha}, \mathbf{h})$$

The function *h()* returns an array of recognized panels; each panel is an element identified by the 4 vertex points:

(x1,y1; x2,y2; x3,y3; x4,y4)

each element (Panel) of the array will also carry the information:

- ✓ anomaly/no anomaly (e.g. 95% probability of true positive)
- ✓ possible anomaly

In case the algorithm is not capable of taking decisions on possible anomaly (anomalies falling under the given threshold of decision), the panel is tagged (see *Figure 2-19* for tagging concept) and the issue resolved at back-end side with the help of a thermal professional operator.

The output of *h()* is updated with a given refresh rate (e.g. 1 to 9 Hz).

2.3.2 $\boldsymbol{f}()$ FUNCTION

2.3.2.1 Theoretical fundamentals

The estimation of a point P in an object reference frame can be carried out through the acquisition of at least two images (stereoscopic acquisition) of the same point. This is the fundamental of photogrammetry. The geometrical approach of this subject is shown in the following figure (Kraus).

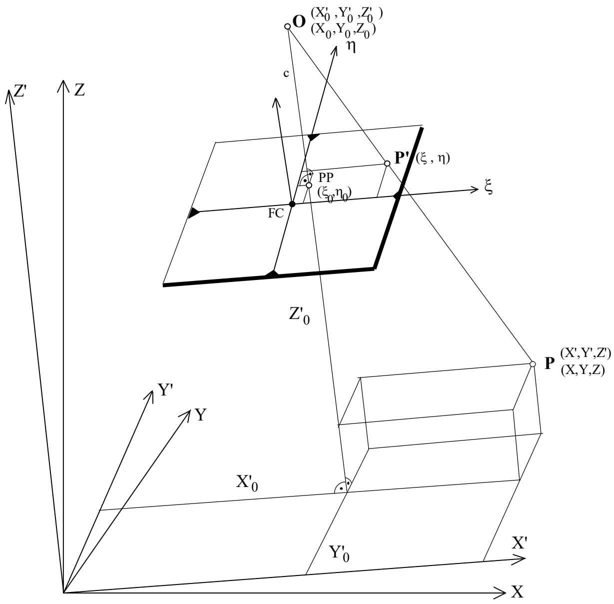

Figure 2-7: photogrammetric geometry conditions

The mathematical equations that relate the image coordinates (ξ, η) and the object coordinates of point P (X, Y, Z) are called collinearity equations:

$$\xi - \xi_o = -c \cdot \frac{r_{11}(X - X_o) + r_{21}(Y - Y_o) + r_{31}(Z - Z_o)}{r_{13}(X - X_o) + r_{23}(Y - Y_o) + r_{33}(Z - Z_o)} = \xi_o - c \cdot \frac{Z_x}{N}$$

$$\eta - \eta_o = -c \cdot \frac{r_{12}(X - X_o) + r_{22}(Y - Y_o) + r_{32}(Z - Z_o)}{r_{13}(X - X_o) + r_{23}(Y - Y_o) + r_{33}(Z - Z_o)} = \eta_o - c \cdot \frac{Z_y}{N}$$

where r_{11}, r_{22}, ….r_{33} are the elements of rotation matrix *R* between image and object systems, which depend on angles ω, φ, κ (roll, pitch, yaw).
The equations can be also written in vectorial format:

$$r_P^{XYZ} = r_O^{XYZ} + R_{\xi\eta}^{XYZ} \cdot s_{P'} \cdot r_{P'}^{\xi\eta}$$

where:

- ✓ r_P^{XYZ} is the position of point P in the object space;
- ✓ $r_{P'}^{\xi\eta}$ is the position of image point in the camera reference system;
- ✓ $r_O^{XYZ}, R_{\xi\eta}^{XYZ}, s_{P'}$ are the external orientation parameters of the image (position of the projection centre, rotation matrix, scale factor for image point *P'*).

These equations show that the three unknown variables, coordinates of point *P* (*X, Y, Z* coordinates), can be estimated through:

- ✓ the measurement of four image coordinates of the same point (homologous points);
- ✓ the knowledge of the "internal orientation parameters" (focal length *c*, position of optical centre projection on the sensor plane ξ_0, η_0, camera distortion parameters) which depend on the camera features;

- ✓ the knowledge of the "external orientation parameters" (X,Y,Z, ω, φ, κ) which represent the geometrical position of camera in the object space.

Internal orientation parameters are usually known. They are supplied with camera in a document called "calibration certificate". Instead, the external orientation parameters are usually unknown and have to be estimated through a procedure called "aerial triangulation". In order to perform this operation, a topographical survey of object points (called Ground Control Points, GCP) is necessary.

According to these fundamentals, it is possible to define a "photogrammetric process", that concerns these operations:

- ✓ topographical survey of GCP;
- ✓ stereoscopic image acquisition;
- ✓ aerial triangulation (external orientation parameters estimation);
- ✓ stereoplotting (object points coordinate estimation).

2.3.2.2 Direct georeferencing approach

Since the first years of 2000 (OEEPE, 2002), the integration between photogrammetric cameras, global navigation systems (GNSS) and inertial measurement units (IMU) has allowed the development of a Direct Sensor Orientation (DSO) approach. In this way, the external orientation parameters of an image can be directly estimated from measures provided by GNSS/IMU systems. Consequently, it does not have to proceed to the aerial triangulation operation in the photogrammetric process and topographical survey of GCP can be limited or deleted.

The geometrical and analytical fundamentals of direct georeferencing approach are represented in the following figure.

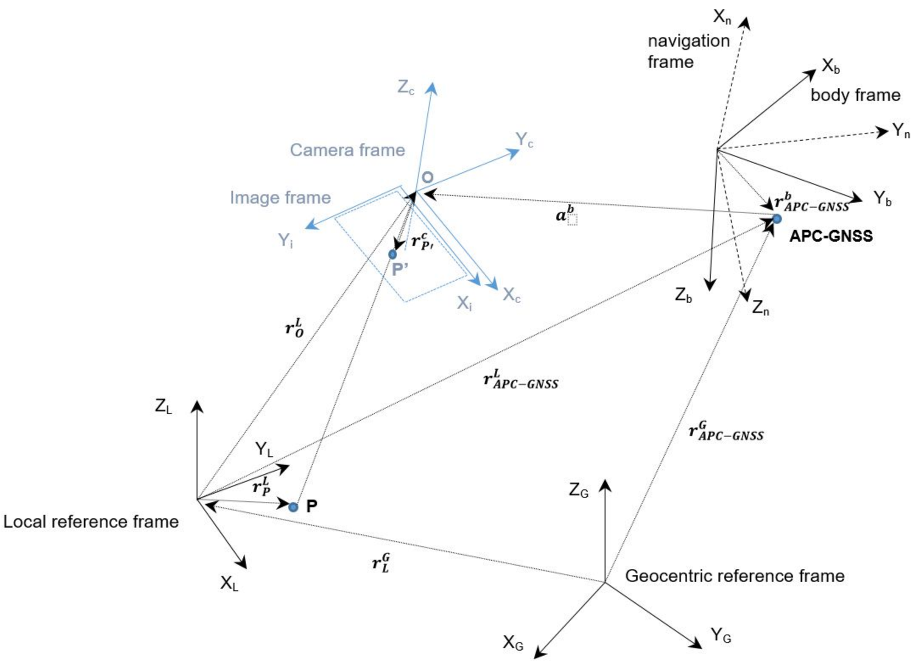

Figure 2-8: frames involved in the DSO procedure

According to the figure above, the collinearity equation can be written as:

$$r_P^L = r_O^L + R_c^L \cdot s_P \cdot r_{P'}^c$$

$$r_P^L = r_{APC-GNSS}^L + R_b^L \cdot a^b + R_b^L R_c^b \cdot s_P \cdot r_{P'}^c$$

where:

- ✓ $r_{APC-GNSS}^L$ is the position of APC - GNSS in the instant t. This vector is known thorough GNSS measures;
- ✓ R_b^L is the rotation matrix between the body frame and the local reference frame in the instant t. This matrix is composed by angles, which are known through IMU measures. In particular, this matrix is computed through this relation:

  $$R_b^L = R_G^L R_n^G R_b^n$$

  where:

  R_b^n: rotation matrix measured by IMU;

  R_n^G: rotation matrix from N frame to G frame, which depends on the geographic coordinates of the N frame origin in G system;

  R_G^L: rotation matrix from G frame to L frame, which depends on the geographic coordinates of the L frame origin in G system;
- ✓ a^b is the offset between APC - GNSS and optical projection centre of camera;
- ✓ R_c^b is the rotation matrix between the camera frame and the body frame.

The last two parameters (a^b , R_c^b) are also called DSO calibration parameters. These values can be directly measured, or estimated by means of calibration procedures.

In conclusion, the measures provided by GNSS an IMU allow to directly compute the exterior orientation parameters of the camera frame. Therefore, the estimation of object coordinates of a point P can be directly performed with the measure of image coordinates of at least two homologous points (Direct geo-referencing approach).

2.3.2.3 f() Function – Direct geo-referencing approach

The purpose of EASY PV project is the development of a product that allows the automatic detection of PV module faults through IR image acquisition from RPAS and direct geo-referencing processing. Regarding the direct geo-localisation, the task of EASY PV is the identification of a point P in the object space (local reference frame L) measuring just a single image point P'. This operation can be performed introducing two geometrical constraints in the analytical model of photogrammetric collinearity:

- ✓ Nadiral image acquisition. In this condition, the optical axis of camera (Zc) is parallel to the Z axis of the local reference plane (Z_L). Therefore, the rotation matrix R_c^L depends only on a parameter (κ angle) and the geometric relation between camera frame and object frame is a roto-traslation with a scale factor. In order to reach a nadiral acquisition from RPAS, the rotation matrix R_c^b has to be known. In particular the parallelism between the axes $X_b – Y_c$; $Y_b – X_c$; $Z_b – Z_c$ has to be verified.
- ✓ Assumption of planar object space. Analytically, this means to consider the object space as a plane with altitude $\bar{Z}_P^L$ in the local reference system L. This constraint allows to identify the scale factor between object point P and image point P'.
- ✓ Temporal synchronization between IMU, GNSS and camera frames.

According to that assumption, the synthetic geometrical model can be represented such as in the figure below.

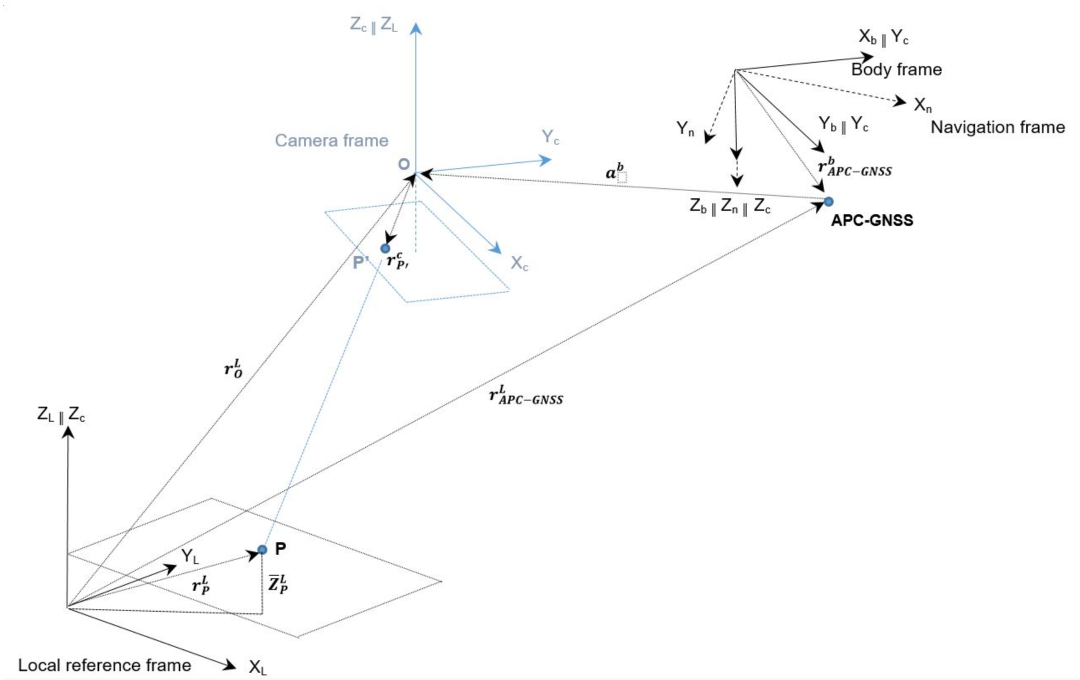

Figure 2-9: EASY PV – Direct georeferencing procedure

In this condition, it is possible to define the f() function, that relates the object point P with the point P':

$$r^L_P = r^L_{APC-GNSS} + R^L_b(\omega, \varphi = o) \cdot a^b + \frac{Z^L_0 - \overline{Z^L_P}}{c} \cdot R^L_b(\omega, \varphi = o) \cdot R^b_c \cdot r^c_{P'}$$

$$r^L_P = r^L_{APC-GNSS} + R^L_G R^G_n R^n_b(\omega, \varphi = o) \cdot a^b + \frac{Z^L_0 - \overline{Z^L_P}}{c} \cdot R^L_G R^G_n R^L_b(\omega, \varphi = o) \cdot R^b_c \cdot r^c_{P'}$$

This function can be solved with the measure or knowledge of these parameters:

- ✓ angular orientation of camera frame, computed by means of IMU or compass measures. In this condition, two attitude parameters (pitch and rool angles) has to be zero.
- ✓ position of centre phase GNSS antenna, provided by RTK - GNSS sensor installed on board the RPAS;
- ✓ internal orientation camera parameters (focal length c, position of optical centre projection on the sensor plane, camera distortion parameters), usually known or estimated by means of calibration assessments;
- ✓ DSO calibration parameters, usually estimated through calibration procedures;
- ✓ temporal synchronization of GNSS/IMU and camera systems.

In conclusion, the solution of f() function allows the estimation of P object point coordinates (X^L_P, Y^L_P) can be performed through the measure of only a *P'* image point $(x^c_{P'}, y^c_{P'})$.

2.3.3 $g(h)$ FUNCTION

The aim of g() function is to provide one unique identifier for each PV panel detected; it is intended to work in **(φ,λ)** space only. The output of the transformation is an array of Panels, each with one unique identifier related to WGS-84 geographical position and the insertion into a relational DB.

$$Array[Panels]_{(\mathbf{ID})} = g\left(Array[Panels]_{(\boldsymbol{\varphi},\boldsymbol{\lambda})}, clock, tol\_dist\right)$$

- $Array[Panels]_{(\mathbf{ID})}$ is the output of the transformation; the unique identifier for each Panel as final result;
- $Array[Panels]_{(\boldsymbol{\varphi},\boldsymbol{\lambda})}$: is the Array of Panels being fed to the transformation function at each algorithm clock cycle;
- $clock$: it is the frame recognition tick (e.g. 5 FPS) provided by the algorithm;
- tol_dist: is the tolerance distance allowed (e.g .0,45 m).

The unique identifier provided by the g() function is related to all the positions falling inside the "Bounding box" surrounding the Panel, detected by the h() function. The function shall be able to add only new Panels and do not consider panels already counted.

The "Bounding box" is a rectangular shape generated by the image processing software which surrounds the cross section of the panel as seen from the sky.

The unique identifier is a related to WGS-84 coordinates position $(\boldsymbol{\varphi}, \boldsymbol{\lambda})_i^k$ representing the centre of *i-th* Panel at *k-th* measurement.

Each panel surrounded by its Bounding box is tracked by the algorithm ***N*** times, therefore its centre is evaluated N times; when the *i-th* Panel is no more present inside the camera view, then its centre is averaged and calculated:

$$(\boldsymbol{\varphi_m}, \boldsymbol{\lambda_m})_i = \sum_{k=1}^{N} \frac{(\boldsymbol{\varphi}, \boldsymbol{\lambda})_i^k}{\boldsymbol{N}}$$

The function is justified by the computer vision algorithm Tracking Module (ref. §2.4.2), requesting the average of the "Centroid" of the Bounding Box at each iteration. The average in geographical coordinates is needed when the Bounding Box (surrounding the Panel) is outside the FOV of CAMERA. Moreover, using a moving average does not require to store all the previous values, but only the average and the actual value for each Panel.

Now, $(\boldsymbol{\varphi_m}, \boldsymbol{\lambda_m})_i$ is the geographical centre of the *i-th* panel updated by means of a moving average; such information will be used to generate the alphanumeric primary key to access the data base and do relational operations on the DB tables**;** The primary key will be related to the *i-th* panel center $(\varphi_m, \lambda_m)_i$ by means of a geographical matching function. In order to insert only new Panels in the DB the g() function shall perform the following control loop expressed in the following meta language:

while(1) *// always do*

do:

for i:1=N do: // *for each panel in the thermal video frame*

$\boldsymbol{If\ (distance|(\varphi_m, \lambda_m)_i - (\varphi, \lambda)_i| \leq tol\_dis}$

DO NOTHING

// $(\boldsymbol{\varphi}, \boldsymbol{\lambda})_i$ *actual measure of i-th panel compared with its mean*

else

INSERT$(\boldsymbol{\varphi}, \boldsymbol{\lambda})_i$ ***INTO DB***

end

end

end

This simple "snippet" in meta-language explains the logic by which the function recognizes new panels. In fact, during PV inspections new panels may be discovered, but also panels already inspected can be captured by the detection software. The metadata included in each thermal video frame allow to calculate each time new centres $(\boldsymbol{\varphi}, \boldsymbol{\lambda})_i$ of the i panels detected in a video frame. The $(\boldsymbol{\varphi}, \boldsymbol{\lambda})_i$ are compared to the $(\boldsymbol{\varphi_m}, \boldsymbol{\lambda_m})_i$ centres already stored and if their geometrical distance is more than the given tolerance distance (e.g .45 cm) , a new Panel entry is inserted into DB.

Open source tools such as MySQL [RD 16] or PostgreSQL with spatial database extender PostGIS [RD 17] implements in part such conditional control for geographical queries.

2.3.4 I/O parameters and Transformations

Table 2-1 summarises the main variables that the algorithm shall handle.

VARIABLE / STRUCTURE NAME		**TYPE**	**DESCRIPTION**	**NOTES**
h	*height* [m]	INPUT	RPAS barometric height w.r.t. starting point pressure	height information can be overridden as experimented in §7.1.1.3.2
α	*slant angle* [°]	INPUT	Lesser angle between the two angles formed from x (BODY) and the borders of a Panel. (see *Figure 2-18*)	During inspections such angle shall be kept close to 0° degrees for best performance under pilot's visual feedback control. Acceptable range is [-8°,+8°]
psi	*yaw angle* [°]	INPUT	yaw angle w.r.t. drone z axis (BODY) rotations	psi is equivalent to azimuth when NED reference system is used.
lat_rtk	*latitude* [°]	INPUT	Geographic latitude of GNSS Antenna "centre of phase"	The geographic latitude is intended already augmented by RTK technology and it is expected to be acquired in NMEA format by OBC
lon_rtk	*longitude* [°]	INPUT	Geographic longitude of GNSS Antenna "centre of phase"	The geographic longitude is intended already augmented by RTK technology and it is expected to be acquired in NMEA format by OBC
g_roll	*gimbal roll* [°]	INPUT	angle formed by gimbal roll axis and y (BODY) axis	Gimbal roll angle is always kept = 0° by gimbal control. However, it is considered as an input used to correct small offsets due to wind or vibrations.
g_pitch	*gimbal pitch* [°]	INPUT	angle formed by gimbal pitch axis and x (BODY) axis	Gimbal pitch angle is always kept = 90° (NADIR pointing) by gimbal control. However, it is considered as an input to correct small offsets due to wind or vibrations.

VARIABLE / STRUCTURE NAME		TYPE	DESCRIPTION	NOTES
TIR	*thermal Infrared image Matrix of Pixels* [Kbit]	INPUT	Complex structure representing the array of the temperature acquired from the camera	The Matrix can have 640x480 or 336x256 pixel resolution. Each Pixel has 14 bit (raw image full scale) or 8bit RGB (color-map). It is recommended a 640x480 pixel matrix for better performance of the algorithm.
VIS	*visible Image Matrix of Pixels* [Kbit]	OUTPUT	Standard Picture in 4/3 or 16/9, available in different formats (e.g. RAW, JPG)	The visual images are not needed as input by the Algorithm; but can be used to shot visual pictures in case of anomaly.
f_rate_TIR	Thermal frame rate [Hz]	INPUT	Number of Thermal frames per second that sensor can generate.	9 Hz is the maximum allowed rate in Europe for imported ITAR free thermographic equipment.
GNSS_p	*GNSS performance*	OUTPUT	Overall GNSS performance indicator (float or fixed solution)	This indicator is provided as visual feedback to the pilot to have knowledge of the overall GNSS performance during operations.
GSD	*Ground Sampling Distance* [cm/pixel]	OUTPUT	distance between two pixels on the ground	GSD is important for pixel transformation in geographic coordinates.
Panel	Photovoltaic Panel identified by the algorithm	OUTPUT	Structured Object defined by: • Center in **X,Y** • 4 corners represented in **X,Y** • Anomaly (Boolean) • Panel_ID (Unique Identifier)	Structured Object (Class - OOP) defined by unique identifier, center, 4 corners and the related information (anomaly/no anomaly). The function f() defined in §2.3.2 allows Panel reference system transformation.

VARIABLE / STRUCTURE NAME		TYPE	DESCRIPTION	NOTES
Panel_ID	Panel unique identifier	OUTPUT		It is based on Panel's WGS-84 center position considering a suitable tolerance distance from the center of panel to the sides.
tol_distance	Tolerance Distance [m]	INPUT	System constant (e.g. 0,50 m)	The tolerance distance expressed in meters represents the maximum error allowed by the system considering all the possible sources of errors and not only GNSS (see §4)
RPAS_DB	Data Base Software Structure	OUTPUT	Data Base to insert Panels	Internal SW Structure (DATA BASE) of Panels to be queried (or inserted) with panel_ID as primary key. The panel_ID unique identifier is based on geographical WGS-84 position and tolerance distance.

Table 2-1: main I/O variables and SW structures handled by the algorithm

2.4 ALGORITHM LOGICAL BLOCKS

The Easy PV core algorithm has in charge the analysis of all the PV panels of the PV plant with the aim of detecting possible anomalies. The algorithm, to be implemented in the form of a software library in RGS S/S, shall be able to recognize the PV panels of a PV plant and assign them an unique identifier, related to WGS-84 geographical coordinates.

Once the identification process of the PV panels has been successfully achieved , the Easy PV Core algorithm checks whether the Panel identified has thermal anomalies.

The image processing alone is unable to achieve these goals for the following reasons:

1) The size in pixels, that is a discriminant feature for the detection of the PV panels, continuously varies according to the RPAS position, height and the orientation of the camera with respect to them

.

2) The transformation between coordinates in pixels and the geographical coordinates requires information that are not available with the image alone.

3) The tracking of the PV panels, that allows the algorithm to assign a unique identifier to each Panel and eventually the presence of anomaly, cannot be carried out without high accuracy positioning of each Panel.

For these reasons the Easy PV core algorithm requires the interaction of four software modules that interact through well-defined interfaces:

1) **Space Transformation**: it is the SW module able to perform the PV panels geo-localization (transformation between coordinates in pixels and the geographical coordinates and vice-versa as detailed in §2.3.2) and to compute dynamically the relation between real measures (e.g. PV panels size in metres) and the size of the objects in pixels.

2) **Panel Tracking**: it is the module that allows to detect all the PV panels inside the scene and to univocally identify. It is able to geo-localize the panels using the GNSS functions.

3) **Anomaly detector**: it is the module that allows to detect the thermal anomalies on the PV Panels.

4) **Event storage**: this module manages the communication with a database for the storage of the anomalies and of the PV panels information (as detailed in §2.3.3)

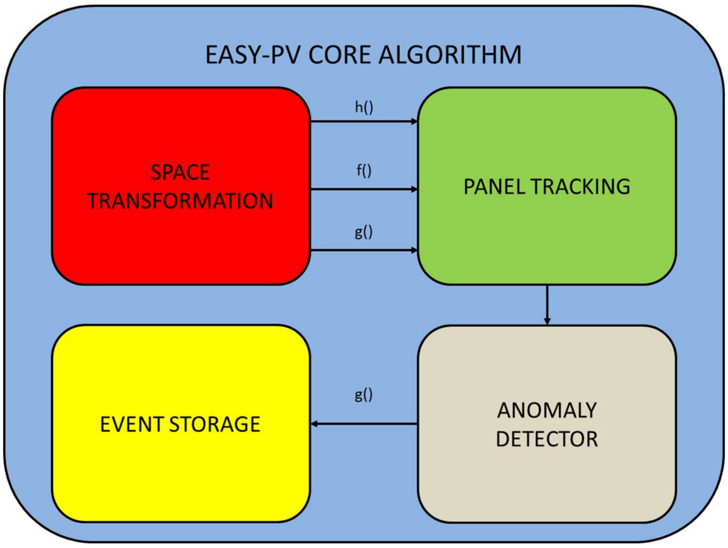

Figure 2-10: Software logical blocks

A brief description of each SW module I/O and interaction is hereafter reported.

2.4.1 SPACE TRANSFORMATION

2.4.1.1 Module inputs

The module receives the input from GNSS receiver and Payload sensors:

- Temporal Time Stamp (e.g., from UTC time)
- RPAS height
- GNSS Antenna Centre of Phase Position.
- Gimbal roll and pitch angles Pointing Error
- FOV camera (fixed)
- Thermal Video Stream.

2.4.1.2 Module outputs

The module provides the following outputs:

- Transformation between pixels and geographical coordinates
- Relation between real measures and dimensions in pixels
- Temporal Time Stamp (e.g., from UTC time)
- RPAS height
- Centre of Camera O(0,0) position in WGS-84;

Thermal video stream augmented with relevant metadata information.

2.4.2 PANEL TRACKING

2.4.2.1 Module inputs

The module receives the following inputs:

- Current frame
- Temporal Time Stamp (e.g., from UTC time) associated to the image
- Thermal image range (e.g. [40,140] °C)
- Inputs that can be required to the Image Geo-Localization SW section

2.4.2.2 Module outputs

The module provides the following outputs:

- Unique ID for Each Panel
- ID of Each Panel linked to a Geographical WGS-84 coordinate
- Automatic recognition of each Panel shape
- Annotated frame with tracking information (shape and ID of each panel)

2.4.3 ANOMALY DETECTOR

2.4.3.1 Module inputs

The module receives the following inputs:

- Current frame
- Temporal Time Stamp (e.g., from UTC time) associated to the image
- Thermal image range (e.g. [40,140] °C)
- Inputs that can be required to the Image Geo-Localization SW section
- Panel Tracking module output

2.4.3.2 Module outputs

The module provides the following outputs:

- ID of Each Panel linked to a Geographical WGS-84 coordinate
- Presence/ no Presence of Anomaly
- Rejection of false positive (e.g. Panel hot junctions)
- Temperature associated to the anomaly
- Annotated frame with anomaly detection information

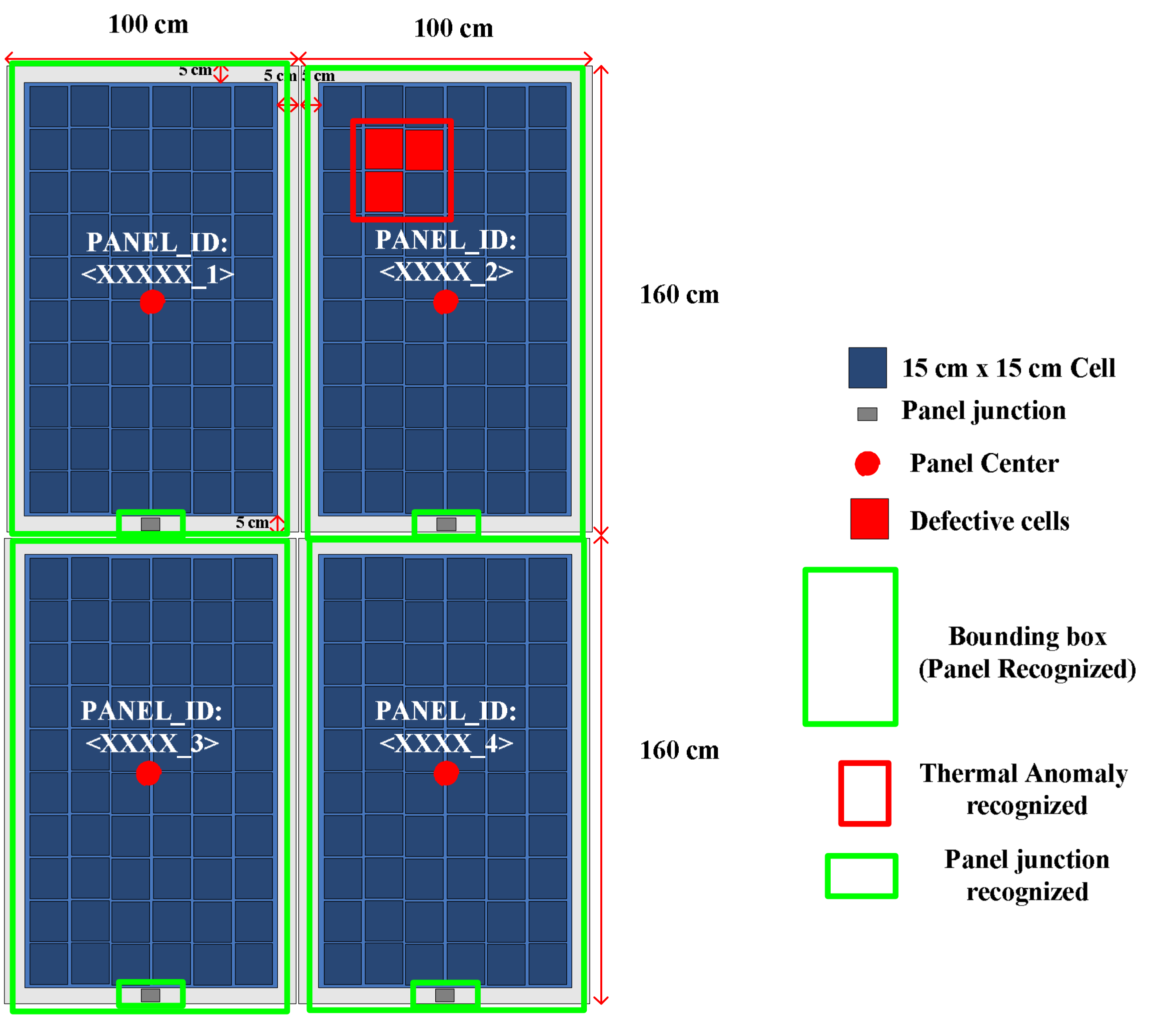

Figure 2-11: SW recognition of PV Panels, Thermal anomalies and thermal false positives

2.4.4 EVENT STORAGE

2.4.4.1 Module inputs

The module receives the following inputs:

- PV panels information
- Anomalies detected
- Images where the anomalies have been detected

2.4.4.2 Module outputs

The module provides the following outputs:

- Records in the database with the information related to the PV panels
- Report of the plant status

MODULES INTERACTION

The sequence diagram in *Figure 2-12* shows the interaction between the "*Panel Tracking*", the "*Anomaly Detector", the* "*Space Transformation*" and the "*Event Storage*" modules. For each frame analysed, the computer vision algorithm implemented in the *"Panel Tracking"* needs to communicate with the *"Space Transformation"* module.

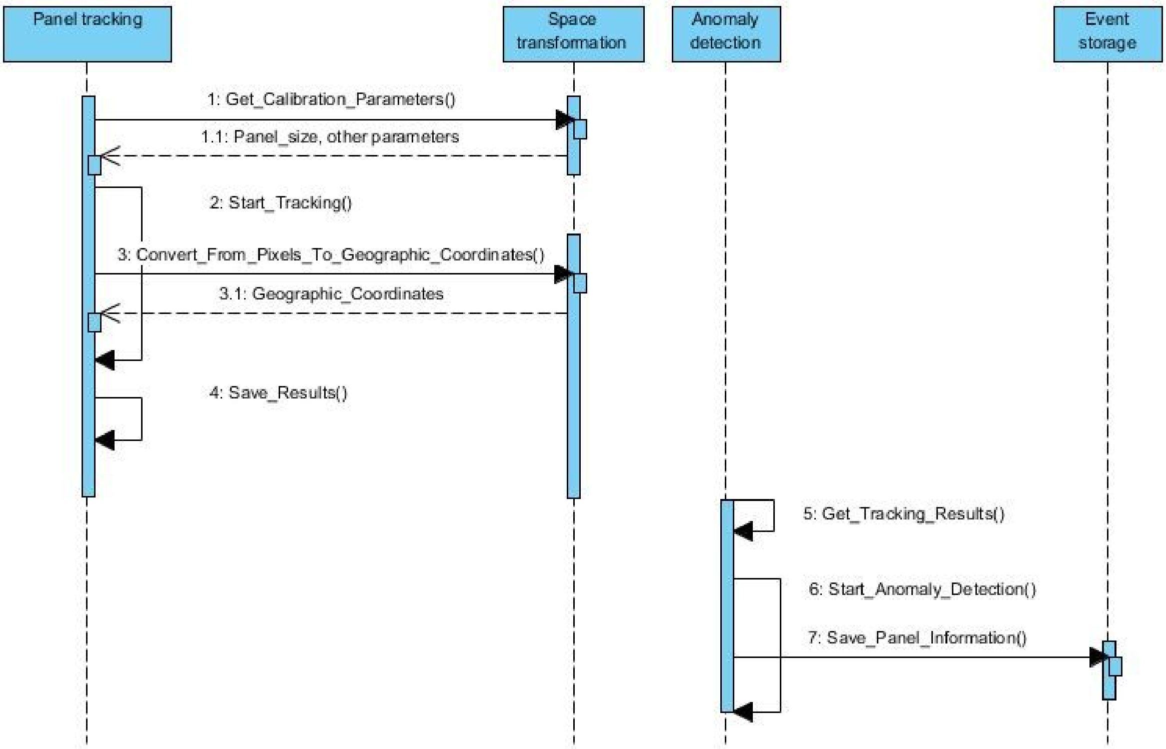

Figure 2-12: Communication among SW modules

The "*Space Transformation"* is basically managed by the *"Panel Tracking"* module, however its output is available for other modules also in case of need.

The first interaction is necessary for the parameters calibration, because the algorithm has to know the precise size in pixels of the PV panel and its cells. Using this information, the algorithm, after the image acquisition and the pre-processing, is able to detect all the PV panels (*Figure 2-13*) in a frame acquired by the camera. Every PV panel is surrounded with a white rectangle that includes its area (i.e. the bounding box).

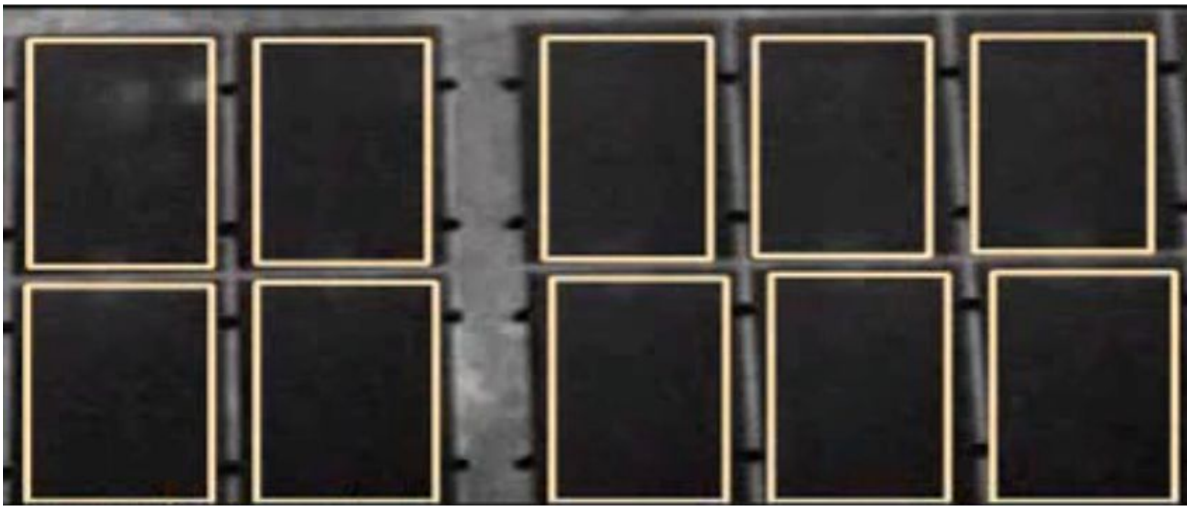

Figure 2-13: PV panels detection example

Then the algorithm needs to identify and to track each PV panel. For this operation the *"Panel Tracking"* module needs to use the functions provided by the *"Space Transformation"* module. The tracking algorithm flow chart is represented in *Figure 2-14*

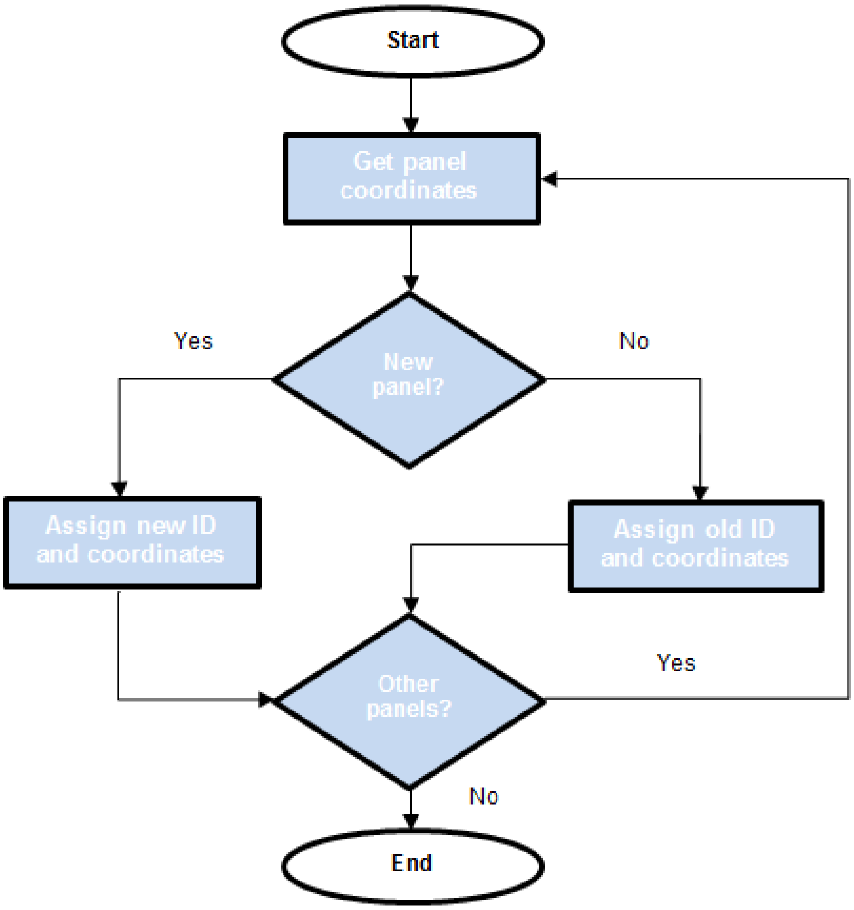

Figure 2-14: Tracking algorithm flow chart

For each PV panel detected, the Easy PV Core algorithm computes the coordinates in pixels of the bounding box center. The function provided by the Panel Tracking transforms these points in the correspondent geographical coordinates (as detailed in f() function - §2.3.2)

All the PV panels detected are then compared with the PV panels already tracked in the previous frames (see g() function §2.3.3 and Figure 2-15). If the geographical coordinates of the centre of the PV panel detected are not in the range of a PV panel already analysed (tolerance distance), a new identifier is assigned and the coordinates are associated to the new PV panel; otherwise, the PV panel results already identified and its geographical coordinates are updated with a moving average (rif. §2.3.3)

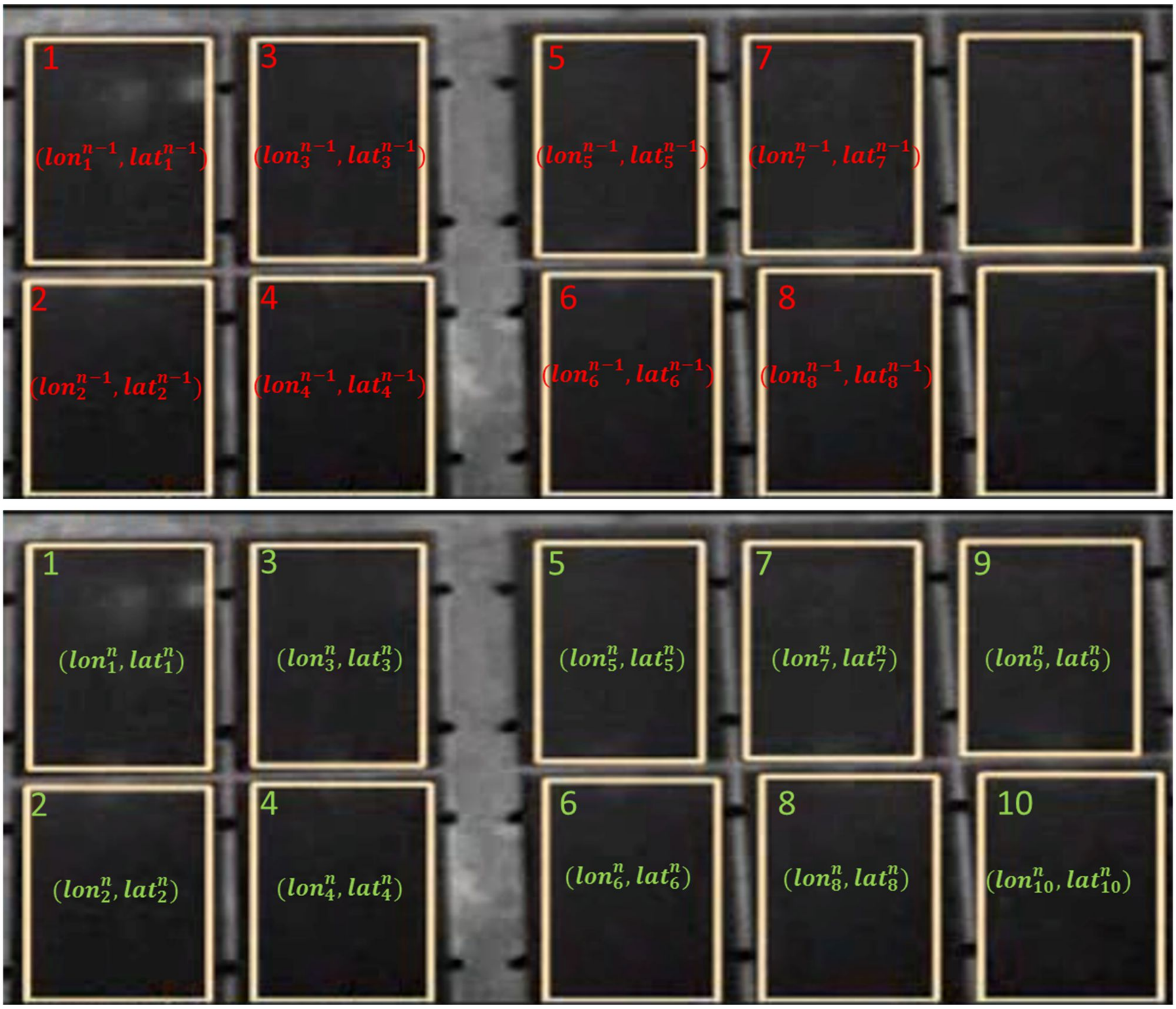

Figure 2-15: Example of PV panels tracking frame; frame n-1 (red), frame n (green)

The results of the tracking before analysing the current frame *n* (namely *n-1*) are shown in red. The results after the processing of the current frame are highlighted in green. The panels already analysed retain their identifiers (1-8), while their geographical coordinates are updated with a moving average. The new panels (9-10) receive a new identifier and their geographical coordinates are associated to the new structure.

The range of geographical coordinates used to match the panels detected in different frames is determined considering the system sources of errors, that are investigated in the next chapter.

Each PV panel is finally analysed in order to detect the anomalies (see *Figure 2-16*). At the end of the processing, the anomaly detector interacts with the event storage module to store the information about the PV panels, namely the geographical coordinates, the anomalies and the images related to them.

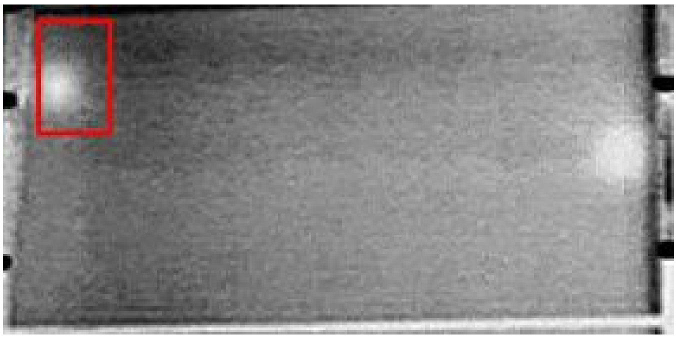

Figure 2-16: Example of thermal anomaly (hot spot) detected

2.5 ANOMALY DETECTOR FLOW CHART

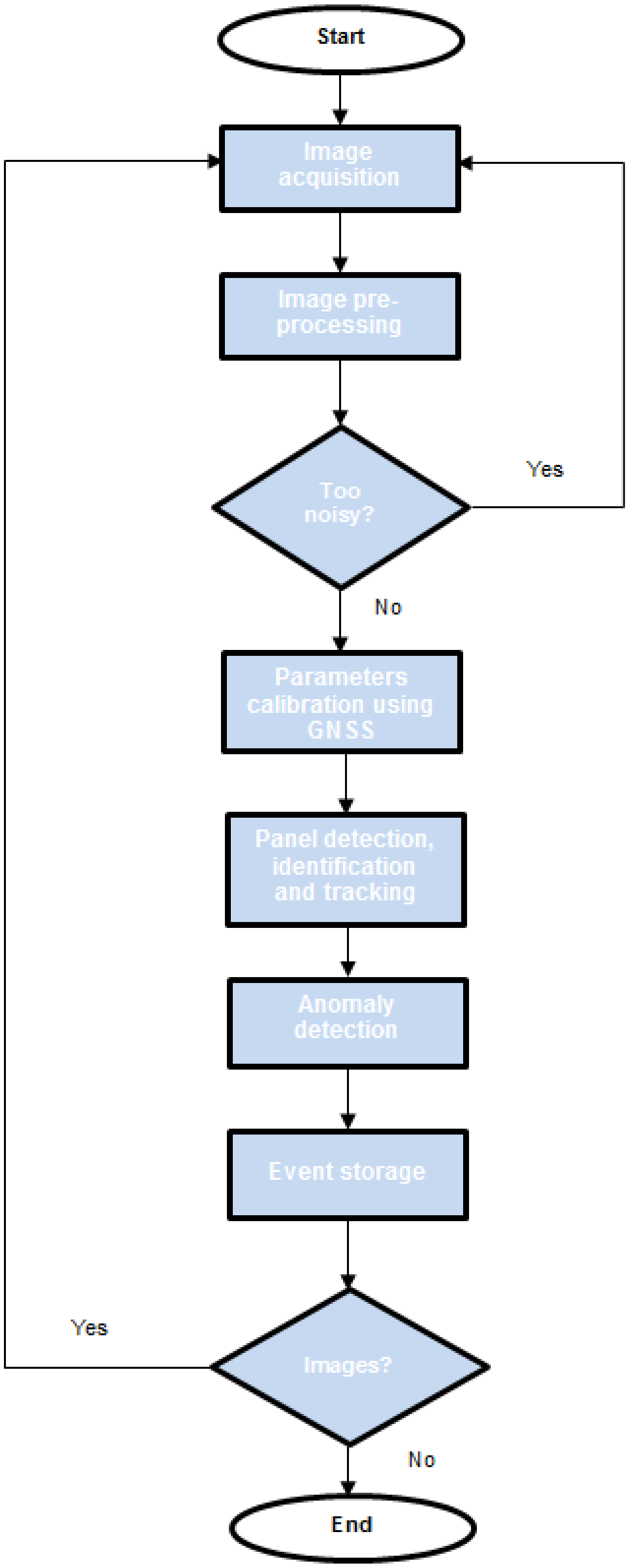

Figure 2-17: Anomaly detection flow chart

The anomaly detection algorithm involves, for each image, the following steps:

- **Image acquisition:** during this step the image is read from the video stream and the timestamp associated to the current frame is stored in an internal structure.

- **Image pre-processing:** the image is pre-processed in order to reduce the noise and the brightness and to enhance the objects of interest within the image (i.e. the PV panels). If the image is too noisy, the algorithm doesn't analyze it, because the noise is a symptom of poor image quality due to sudden movements of the RPAS. So in this case it's better to discard the image in order to avoid false positives and give a visual feedback to the pilot whom can take corrective actions.

- **Parameters calibration using GNSS:** the anomaly detector algorithm needs to know the size in pixels of the PV panel and of its cells. This dimension continuously varies according to the position and orientation of the camera with respect to the PV panels. For this reason these parameters shall be updated for each frame using the information provided by the Panel Tracking module.

- **Panel detection, identification and tracking:** the PV panels in the scene are detected using a specific computer vision algorithm (see §3.4). In order to understand if each PV panel has been already analysed or not, a tracking algorithm using the geographical coordinates is provided. Such functionality is offered by the Panel Tracking module to identify and geo-localize the PV panels.

- **Anomaly detection:** each PV panel is analysed in a way to detect possible anomalies (e.g. hot spots) and to discriminate them with respect to false positives (e.g. panel hot junctions).

- **Events storage:** for each panel the system stores the geographical coordinates, the identifier and the anomalies detected. Moreover, all the images where the anomalies have been detected are stored in the database according with the *g()* function detailed in §2.3.3.

2.6 ALGORITHM CONSTRAINTS

In order to simplify the scenario in which the Easy PV Core algorithm will carry out PV panels geo-localization and anomaly detection, it is necessary to define the following constraints:

- **Minimum cell dimension in pixels**: the successful detection performed by the algorithm also depends upon the minimal dimension of the area to be recognised. However, considering the PV panel methodology of construction this doesn't represent a constraint as the panel has a minimum cell size of 15x15 pixels. It will impose a limit on the RPAS height during the flight (considering the FOV and the resolution of the camera (15-20 panels expected per frame).

- **Maximum slant tolerance of the panel**: the algorithm has to distinguish real anomalies (e.g. hot spots) from false positives (e.g. panel's hot junctions). The only way to discriminate between hot spots and panel hot junctions is the analysis of the position of the thermal anomaly in the PV panel region. For this reason it is important to guarantee that the PV panel is framed in horizontal or vertical position. Thus, the maximum slant tolerance with respect to the PV panel sides is of ±8 degrees (see *Figure 2-18*). This constraint requirement will impose constraints on the pilot's visual feedback. If this constraint is not respected, the precision of the algorithm may be reduced.

- **Minimum number of frames for each panel**: the algorithm needs to analyse a minimum number of images of the same PV panel in order to achieve a good accuracy for tracking and anomalies detection. Thus, a minimum number of 5 frames for each PV panel is required. This constraint will impose a limit on the RPAS velocity (5-8 m/s expected) and height (10-15 metres from the modules expected, considering the FOV and the resolution of the camera).

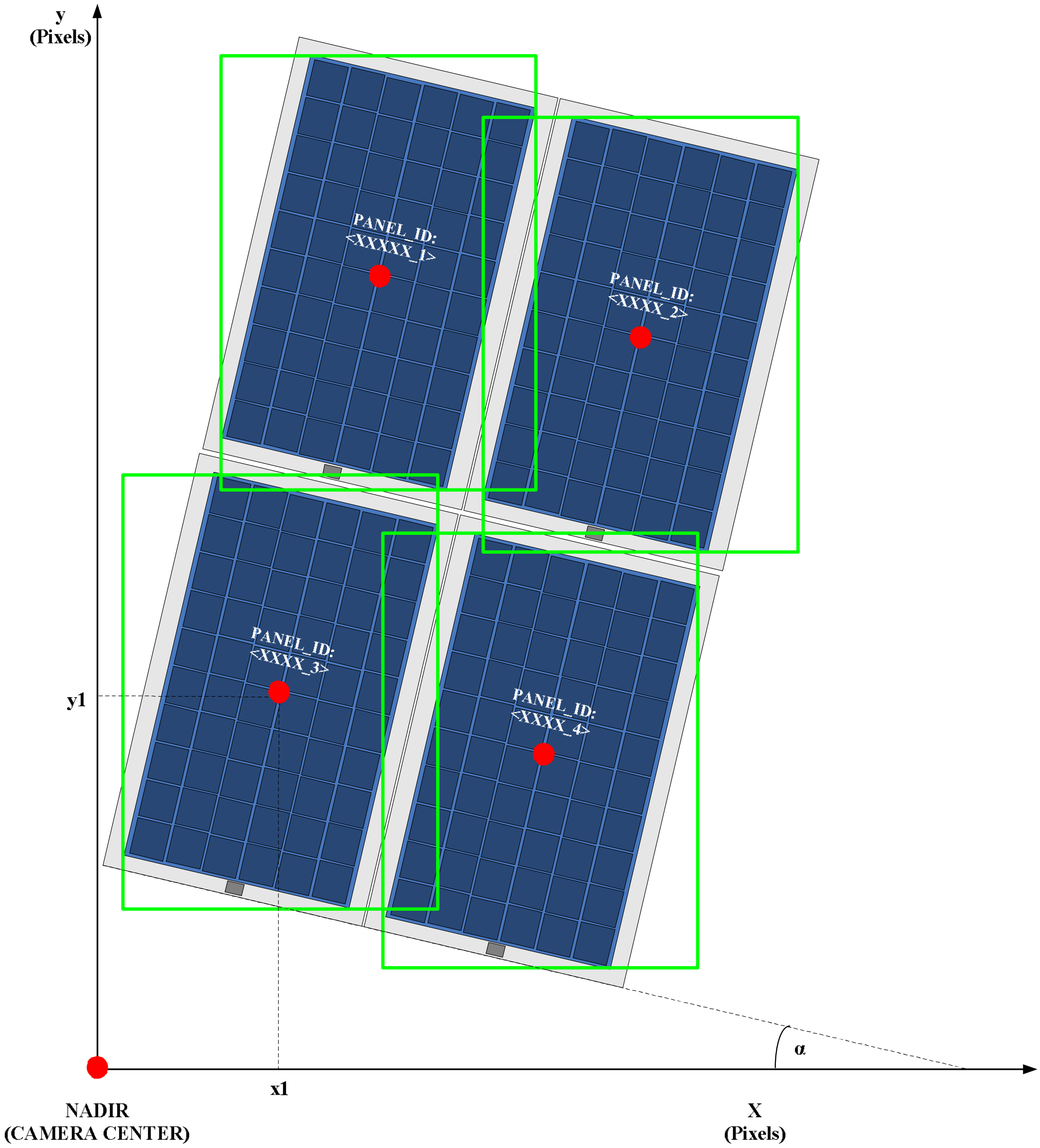

Figure 2-18: Longitudinal acquisition of PV Panels with maximum slant angle (α) allowed

2.7 PILOT'S FEEDBACK

A feedback to the Pilot, by means of a dedicated HMI (e.g. Android application) is needed during flight operations. The best design can be achieved with integration of Pilots on-field experience and SW engineers.

The most relevant parameters to be controlled are:

- GNSS real time performance (e.g. estimated accuracy);
- Configurable thermic parameters provided by FLIR API (e.g. AGC, temperature ranges, …)

- Slant angle indicator with visual warning in case of high values if needed (diagonal inspections reduce algorithm performance);
- Tilt angle indication about the inclination of Group of panels if needed;
- Live recognition of Panels Bounding box (Real time algorithm execution to be verified)
- Mean temperature inside each Bounding box (Real time algorithm execution needed to be verified)
- Panel Checked if counted (Real time algorithm execution needed)

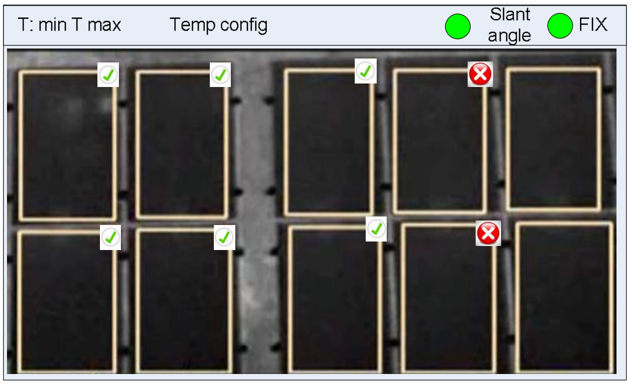

Figure 2-19: Example of Pilot HMI (e.g. Android App) in case of Real time processing capabilities

In case of real time processing capabilities, it will be possible to give the pilot the possibility to manually tag (e.g. with his fingers on the touch display) unrecognized panels or force the algorithm detection in case of conflict; this is a very appealing feature that will be soon verified in early development stage.

The feasibility of real time software elaboration feedback is a "*nice to have*" feature very challenging to obtain that can also "*help*" the algorithm at back-end side to make decision in case of uncertainness on a given thermal anomaly.

Such feature will be supported in case of positive testing, without excluding the possibility to resolve the recognition conflict at back-end side.

3 COMPUTER VISION FOR OBJECT DETECTION AND TRACKING

3.1 STATE OF THE ART

Object tracking plays a fundamental role in several video analysis applications, including video surveillance, traffic monitoring, ambient intelligence, human–computer interaction.

Classical approaches focus on moving objects tracking with fixed camera: given a video sequence containing one or more moving objects, the desired result is the set of the trajectories of these objects. In the last few years the researchers investigated also the challenging problem of tracking with moving camera. In this field it is interesting to deal with both stationary objects (e.g. PV panels) or moving objects (e.g. cars, people), whose movement can be confused with that of the camera itself.

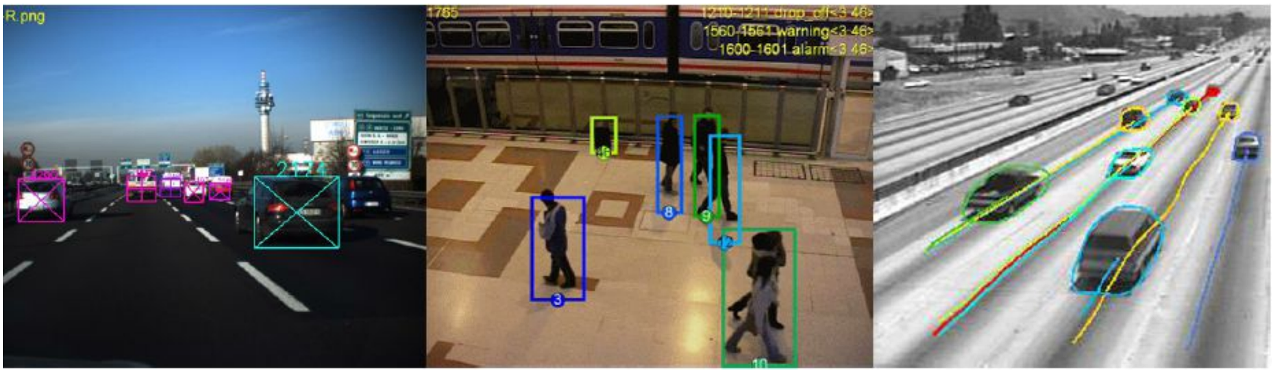

Figure 3-1: Tracking with fixed or moving Camera

In the first part of this document we give a comprehensive review of the most important methods proposed in the literature in recent years.

In the second part we describe the approach that we propose to solve the problem of PV panels detection and tracking.

3.2 TRACKING WITH FIXED CAMERA

The algorithms proposed in the literature can be divided into two categories: in the first category tracking is performed after an object detection phase, using differences from a background model or an a priori model of the objects; in the second category detection and tracking are performed together, usually on the basis of an object model that is dynamically updated during the tracking.

Figure 3-2: Example of background substraction

Algorithms in the first category are usually faster, but they have to consider also the errors of the detection phase as spurious and missing objects, objects split into pieces, multiple objects merged into a single detected blob. These algorithms tipically build an appearance model of the objects, considering their position in the image or intrinsic properties such as color, texture and shape. The appearance model is used by the tracking algorithm to follow the same object in different frames and to reconstruct the complete trajectory covered during the video sequence, dealing with occlusions, splitting and merge.

Figure 3-3: Example of occlusion, merge and split (1)

The simpler tracking methods use only the position of the object to compute the measure of appearance. As an example, the methods proposed in [RD 38], [RD 39] and [RD 40] use a greedy algorithm that matches each object to its nearest neighbour, with constraints based on proximity. The system described in [RD 41] uses the overlap of the areas as a criterion to find a correspondence between the objects at the current and at the previous frame.

Other approaches use more accurate techniques in order to deal with detection errors and occlusions. The method proposed in [RD 42] formulates the tracking problem as a bipartite graph matching, recognizing the occlusions and solving the problem with the well-known Hungarian algorithm. The method described in [RD 43] tries to predict the trajectories on the scene using a set of behaviour models learned using a training video sequence. The approach in [RD 44] uses stereo vision, coupled with a motion dynamic model and an object appearance model to perform the tracking. Other authors have proposed in [RD 45] a method able to track pedestrians by using shape and appearance information extracted from infra-red imagery.

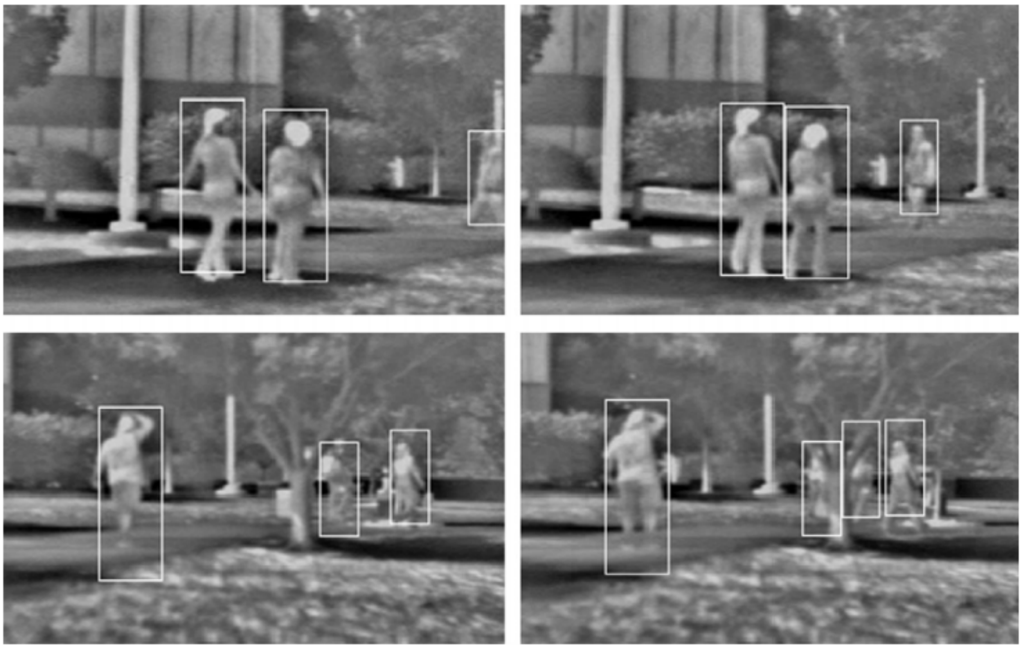

Figure 3-4: Pedestrian detection using shape and appearance (9)

Several recent methods, such as [RD 46], [RD 47] and [RD 48], use the information from different cameras with overlapping fields of view in order to perform the occlusion resolution. The data provided by each camera are usually combined using a probabilistic framework to solve the ambiguities.

Figure 3-5: Example of Multi-view tracking (12)

Algorithms in the second category are computationally more expensive, and often have problems with the initial definition of the object models, that in some cases has to be provided by hand. In [RD 49] the authors propose the use of Mean Shift, a fast, iterative algorithm for finding the centroid of a probability distribution, for determining the most probable position of the tracking target. It requires a manual selection of the objects being tracked in the initial frame, and deals only with partial occlusions. In [RD 50] other researchers proposed a method based on a layered representation of the scene, that is created and updated using a probabilistic framework. Their method is able to deal with occlusions, but is extremely computational expensive, requiring up to 30–40 s per frame. The method in [RD 51]tracks people in a crowded environment. However it uses an a priori model of a person, that is not extendable to other kind of objects.

Figure 3-6: Example of mean-shift application (13)

The approach in [RD 52] uses edge-based features called edgelets and a set of classifiers to recognize partially occluded humans; the tracking is based on the use of a Kalman filter. The method does not handle total occlusions, and, because of the Kalman filter, it works better if the people are moving with uniform direction and speed. The method proposed in [RD 53] detects and tracks objects by using a set of features, assigned with different confidence levels. The features are obtained by combining color histograms and gradient orientation histograms, which give a representation of both color and contour. The algorithm is not able to handle large scale changes of the target objects. The method in [RD 54] uses a skin colour model to detect and then track the faces in the scene. The algorithm is able to deal with crowded scenes where the persons are dressed with very similar attire, but it works only as long as the face of each person remains clearly visible.

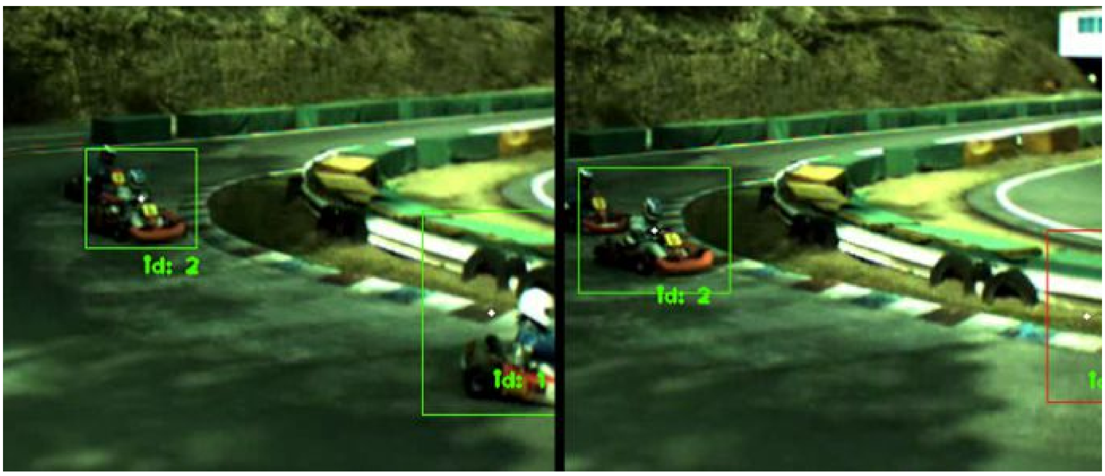

Figure 3-7: Tracking using Kalman Filter

A recent, promising trend in tracking algorithms is the use of machine learning techniques. As an example, the method in [RD 55] improves the ability of tracking objects within an occlusion by training a classifier for each target when the target is not occluded. These individual object classifiers are a way of incorporating the past history of the target in the tracking decision. However, the method assume that each object enters the scene unoccluded; furthermore, it is based on the Particle Filters framework, and so it is computationally expensive. Another example is the method in [RD 56] that uses manifold learning to build a model of different pedestrian postures and orientations; this model is used in the tracking phase by generating for each object of the previous frame a set of candidate positions in the current frame, and choosing the candidate that is more close according to the model.

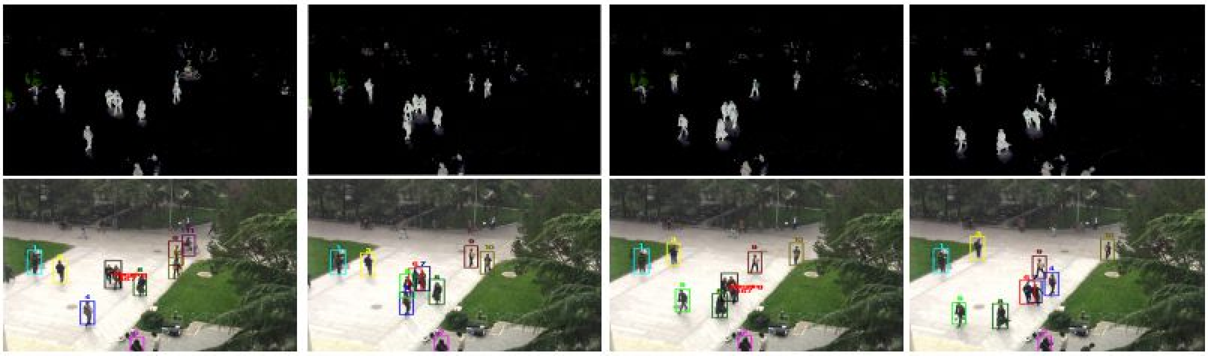

Figure 3-8: Tracking with particle filters framework (19)

3.3 TRACKING WITH MOVING CAMERA

The previous case of objects tracking with fixed camera, that is typical for video-surveillance applications, takes advantage that the background is fixed or slowly variable. So there are many algorithms for background modelling able to separate the dynamic parts of the scene (moving objects) from the static background. When both the camera and the scene move, the classic background subtraction algorithms cannot be used, because the stationary background requirement is not respected.

Some of the methods proposed in the literature to solve the problem of objects tracking with moving camera need the a priori knowledge of the environment. An example is the method proposed in [RD 57] that is able to achieve very good results if certain constraints are respected. The a priori knowledge of the environment is exploited for the optimal configuration of the optical flow, using the Lucas-Kanade algorithm, and the application of the epipolar geometry.

Figure 3-9: Optical flow with Lucas-Kanade Algorithm (21)

All the algorithms proposed in the last few years, instead, use different techniques to estimate the misleading movement due to the moving camera in order to separate the background pixels from the foreground ones. In [RD 58]the authors describe an algorithm for unsupervised motion-based object segmentation employing bidirectional inter-frame change detection. For every frame, two error frames are generated using motion compensation. They are combined and a segmentation algorithm based on thresholding is applied. The method proposed in [RD 59] defines a hierarchical differential Global Motion Estimation. The initial estimation of the motion is performed using a scheme which combines three-step search and motion parameters prediction. The objects are recognized using a robust estimator able to reject outliers introduced by local motion. In [RD 60] the authors use a double-difference image, an estimation of the background, to detect the motion regions from the video frames. The algorithm computes the double-difference image in two steps: in the first phase, it generates two difference images from the corresponding two next images; then it binarize the difference images and execute AND operation. The moving objects are then detected analyzing the foreground regions in the double-difference image. The method described in [RD 61] use the epipolar geometry in order to discriminate between background and foreground salient points. The features are extracted using the Sobel filter and the Harris corner detector. The moving object regions are obtained through an integration scheme based on foreground feature points and foreground regions, which are obtained using an image difference model. Then, a compensation scheme based on the motion history of the continuous motion contours obtained from three consecutive frames is applied to increase the regions of moving objects. Finally, the moving object are tracked using the Kalman filter.

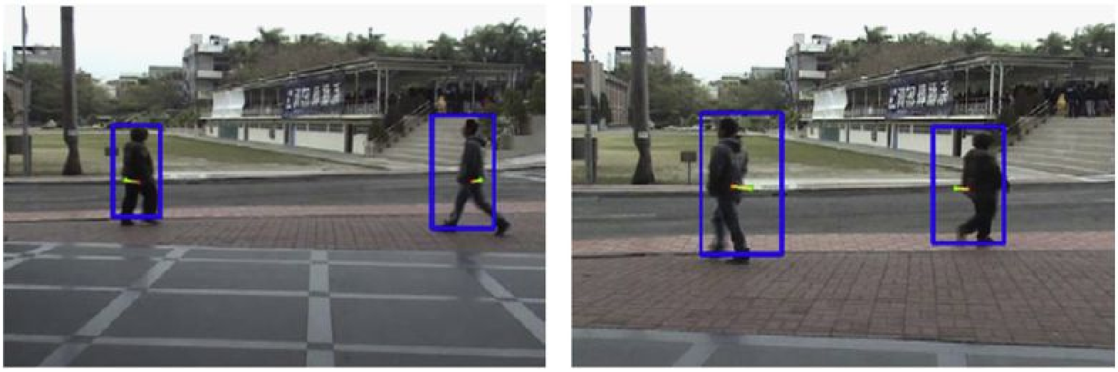

Figure 3-10: Tracking using foreground salient points and epipolar geometry (25)

3.4 PROPOSED METHOD FOR PV PANELS DETECTION

PV panels detection is very challenging due to their regular chromatic and geometric characteristics. Our idea is to exploit their regularity. The PV panels detection algorithm analyses the image trying to find the grid structure of the PV plant. After this step, we process the grid in order to find each PV panel and to perform anomaly detection.

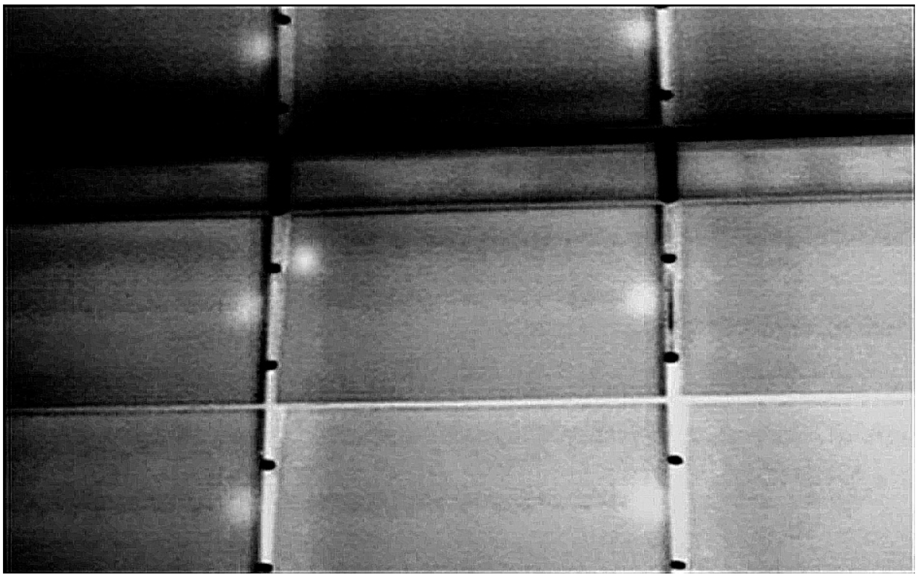

Figure 3-11: Example of PV panels thermal image acquired by a drone

We noticed that the images acquired by the drones are very noisy, so we need to pre-process the image so as to normalize the luminosity. This operation gives us a two-fold benefit: first, it allows to reduce the noise and to point out the lighter areas; second, we can decide, after the normalization, to discard the image if it is still too noisy.

Then we apply the Canny algorithm [RD 62] to the image in order to detect the edges of the PV plant grid (*Figure 3-12*)

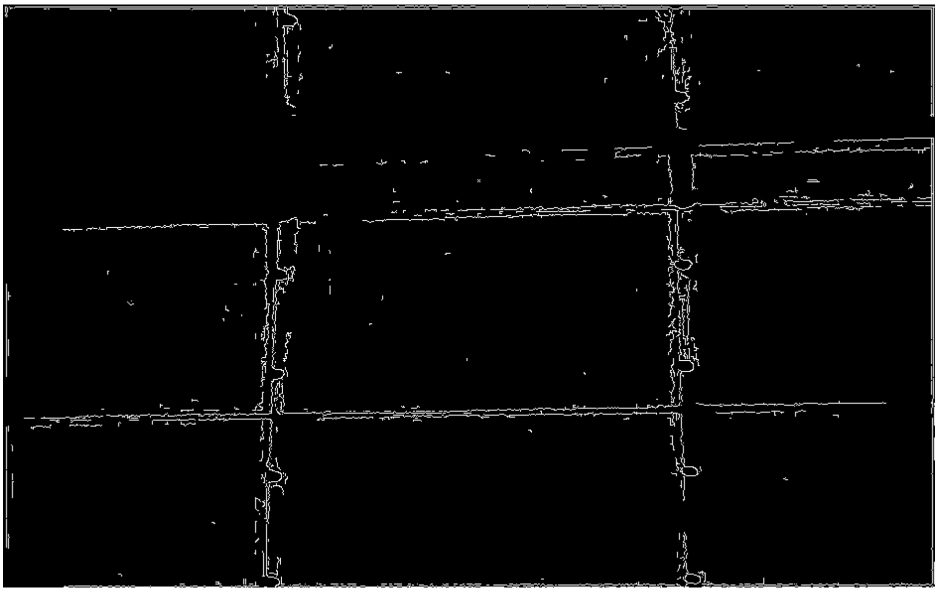

Figure 3-12: PV panels edge detection using Canny Algorithm

We use the binary image with the edges to find the contours of the PV panels applying the Hough transform. *Figure 3-12*shows that there are a lot of lines for each PV panel border and some false positives.

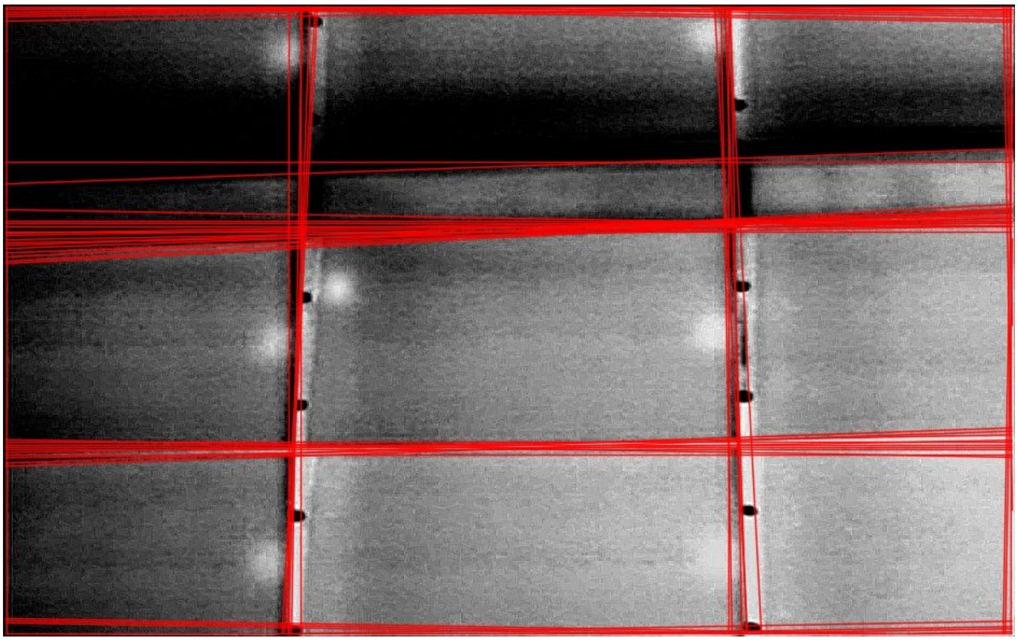

Figure 3-13: Application of the Hough Transform

We solve both the false positives and the multiple lines using a clustering algorithm that consider a line as a panel border if it is composed of at least a certain number of lines detected by the Hough transform. Then we are able to find the borders of the panels and the intersection between the lines.

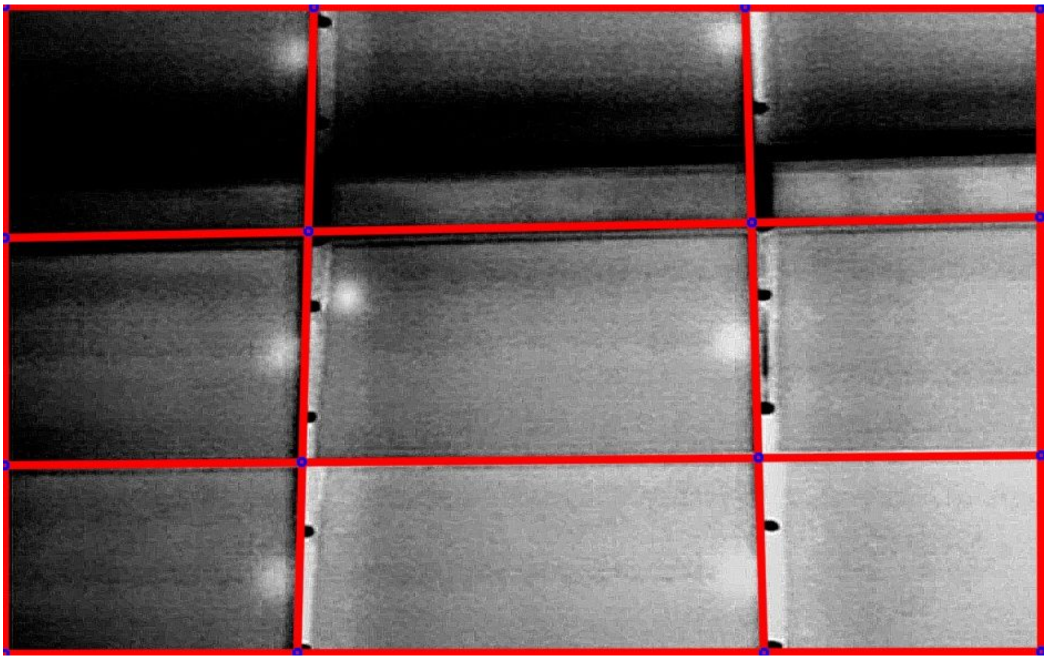

Figure 3-14: Lines clustering, intersection detection and ROI extraction

Using the size in pixels of a PV panel, we are now able to determine a region of interest (ROI) for each panel. So we can analyze and track all the detected panels in order to recognize the anomalies.

The current implementation of the algorithm requires the minimum and maximum size in pixels of a PV panel as input parameters. This is a strong requirement because it force the pilot to drive the drone always at the same altitude so as to allow the algorithm to recognize the PV panels. Our idea is to remove this constraint using the GNSS system and other UAV sensors. Indeed, starting from the knowledge of the flight parameters of the UAV (geographic coordinates and orientation obtained from UAV compass) and the field of view of the camera, we can find relation between dimensions in pixels and in meters. Since all the PV panels have the same size in meters, we can infer approximately the size in pixels of the ROI where the algorithm will detect the anomalies.

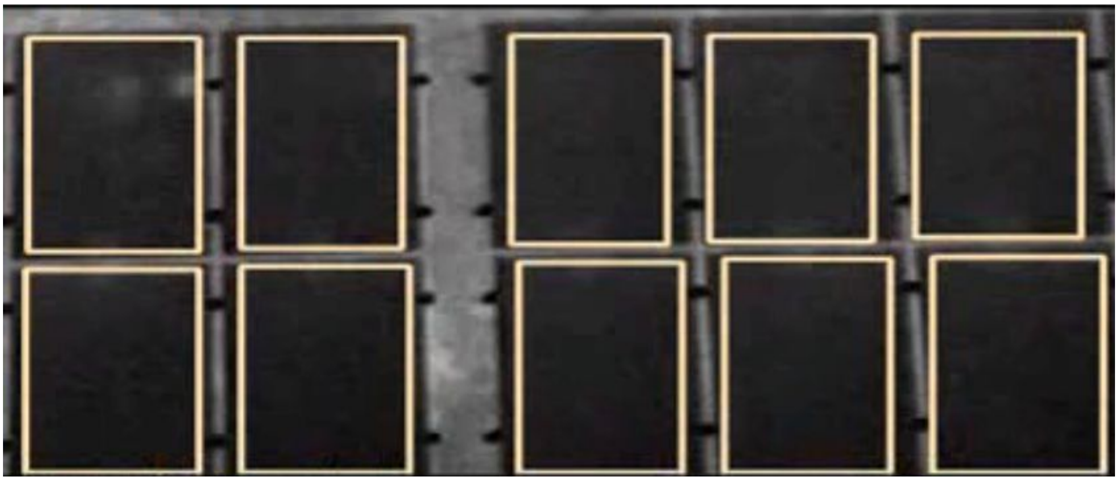

Figure 3-15: Example of PV panels detection

3.5 PROPOSED METHOD FOR PV PANELS TRACKING

The classic aim of the tracking is the pursuit of the moving objects. The movement is the most used feature to track the objects and several background subtraction algorithms have been proposed to detect the dynamic pixels in the scene. The researchers often use additional features in order to improve the accuracy of the appearance model, such as colour, texture and shape of the objects. The same features may be used to detect stationary objects with specific characteristics, using a model-based approach.

It is evident that the classic approaches are not able to deal with PV panels tracking. This problem falls within a particular category: indeed, the PV panels are stationary objects framed by a moving camera. Moreover, the PV panels, as well as being stationary, are identical to each other, so it is not possible to use colour, texture and shape to track them.

Starting from these observations we conclude that the PV panels can be uniquely identified only knowing their geographical coordinates. More accurate is the system that associates the geographic coordinates to a point in the image, the greater will be the precision of the tracking algorithm. The accuracy required by the algorithm has to be compliant to requirement SR.0210 (ref. 5.2 [RD 8]); This component is only one of the sources of error identified (ref. §4), so it shall be handled as all the other sources using a best effort approach. This case study could lay the foundations for a new class of algorithms for tracking objects.

After the panel detection, we propose to use the geographic coordinates as basis to compute the appearance model of the specific panel. The similarity measure used to compare each detected panel with all the panels previously tracked is the distance in terms of their WGS-84 geographic coordinates. The precision of the measure provided by the GNSS system will be basic for the accuracy of the proposed tracking algorithm. Under this assumption we can use a simple overlap tracking algorithm, for example one of those proposed in [RD 38], [RD 39], [RD 40] and [RD 41]. If the detected PV panel is within a certain interval with respect to the geographic coordinates of a previous tracked panel, it will inherit the same identifier and its position will be updated in order to have a more accurate estimation. Otherwise the detected panel is analysed for the first and it is considered as a new object by the tracking algorithm. The range of geographical coordinates used to match the panels detected in different frames will be determined considering the system sources of errors.

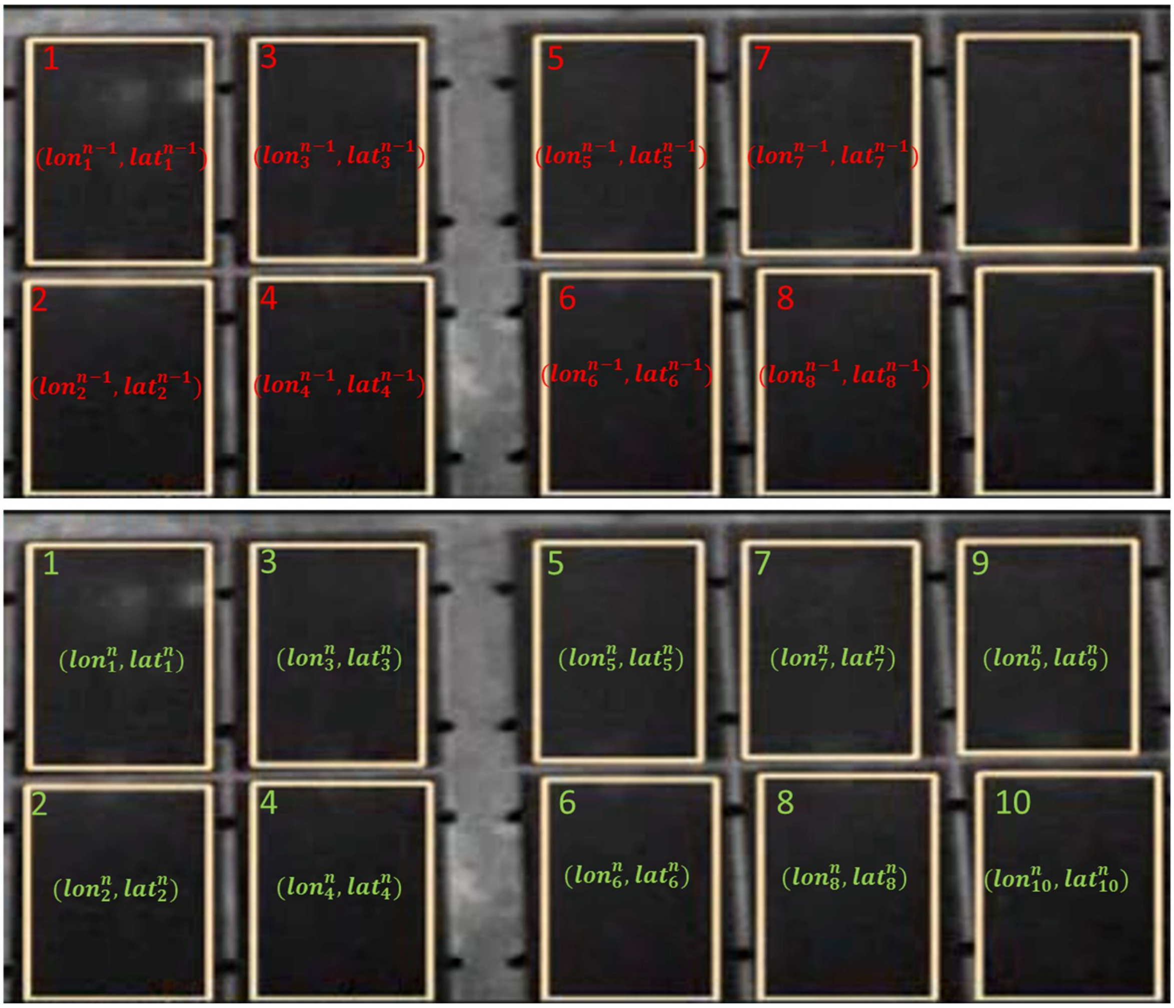

Figure 3-16: Example of PV panels Tracking

4 GNSS SOLUTIONS FOR EASY-PV APPLICATION

4.1 KEY PERFORMANCE INDICATORS

4.1.1 GNSS Positioning Accuracy

EASY-PV solution requires decimetric positioning accuracy according to SR.0210 indicated in [RD 8] for the operation of RPAS in identifying a faulty solar element within a solar panel. The accuracy requirement, however, depends on several factors; for instance, the quality of image captured by thermal camera at a certain altitude and other related practical factors. Therefore, a complete RPAS subsystem error budget (including additional equipment other than GNSS receiver) needs to be calculated to freeze the accuracy requirement to SR.0210. Details are provided in the annexed note "End to end EASY-PV algorithm", where GNSS positioning accuracy is only one of the source of error to be considered to achieve the requested performance stated in SR.0210.

4.1.2 GNSS Availability

GNSS availability refers to the percentage of time that the services of the GNSS are usable for EASY-PV service. The RPAS subsystem availability, defined as the percentage of time that the computer vision algorithm is usable to detect an anomaly, is conditioned by the availability of GNSS (as well as contingent external correction information) as the anomaly geo-tagging is referenced to the RPAS GNSS positioning

4.1.3 GNSS Receiver cost

One of the objectives of EASY-PV is to develop a low-cost solution for monitoring of photovoltaic plants, for this reason, the final GNSS solution must be low-cost yet fulfils the accuracy RPAS requirements SR.0210 reported in [RD 8].

4.1.4 Deployment constraints

The Easy-PV primary solution is based on a custom easy-to-use payload to be installed on a suitable RPAS, controlled by a dedicated RGS. As consequence the GNSS receiver should be chosen according to the constraints explained in [RD 8]. The user of this solution will be the large community of registered RPAS pilots and aerial operators widely spread over the area of operations, as well as new professionals attracted by new business opportunities.

4.2 TECHNICAL SOLUTIONS

4.2.1 Standalone positioning

GNSS provides position, navigation, and timing solution anytime anywhere across the globe. Currently, NAVSTAR GPS and GLONASS are fully operational constellation, whereas, Galileo and BeiDou are going through full constellation deployment phases. Typical positioning accuracy (95%) provided by NAVSTAR GPS is 9m and 15m in horizontal and vertical dimension respectively under normal user conditions[RD 18]. Though, GNSS accuracy is the key enabler for variety of user applications, however, there exists numerous applications that demand higher positioning accuracy and precision as their operational requirement. In order to improve GNSS positioning accuracy several techniques are used that are briefly described in the following subsections.

4.2.2 GNSS Correction Services

4.2.2.1 Differential Corrections Using Ground Stations

Differential correction system augments GNSS users by providing pseudorange error corrections to improve positioning accuracy, navigation, and timing services. Existing differential correction systems primarily augments GPS civil users in real-time, these systems are known as DGPS (GPS for representing NAVSTAR GPS). For instance, the American NDGPS, the Canadian DGPS, and the European DGPS covering Finland and Sweden. DGPS systems provides positioning accuracy ranging from 1-5 meters by broadcasting ranging correction either using radio beacons or L-band satellites. The correction coverage is limited to several hundred kilometres.

Differential systems such as, SBAS, provides correction and integrity information through GEO satellites, thus covering a large region typically a continent. Though, SBAS system is primarily designed for SoL applications, such as aircraft landing, nevertheless, it is widely used by various applications that demand certain level of positioning accuracy. Existing SBAS systems include the European EGNOS, the American WAAS, the Japanese MSAS, and the Russian SDCM.

EGNOS Space Segment consists of three GEO satellites broadcasting pseudorange corrections and integrity information for single-frequency GPS users using the L1 frequency band used by GPS satellites[RD 19]. The EGNOS Ground Segment comprises of a network of RIMS, MCC, and NLES. The components of the ground segment network are connected through EWAN, which provides the communication mechanism between the network components. Figure 4-1 depicts the EGNOS system architecture.

EGNOS offers SoL service designed for safety-critical applications and OS for non-safety critical applications. EGNOS services are open and free of charge. Using the EGNOS corrections, standalone GPS L1 users achieve positioning accuracy (95%) of 3 m in the horizontal direction and 4 m in the vertical direction [RD 19].

4.2.2.2 L-band Corrections using satellite: PPP solution

L-band is just like EGNOS, but with privately owned reference stations and communication infrastructure, rather than provided by a state agency. EGNOS primarily focuses on integrity and accuracy, whereas L-band corrections are mainly focused on providing high accuracy to end-users. The L-band corrections offer sub-meter through centimetre positioning accuracies. Such accuracies are achieved by making use of PPP technique, which utilizes precise orbit and clock correction and carrier phase pseudorange measurements for position estimation.

The PPP service provider estimates in real-time precise orbit and clock correction using a global GNSS reference network and broadcasts this information to the end-user via geostationary satellites and/or through Internet as depicted in Figure 4-2. The end-user utilizes these corrections along with carrier-phase pseudorange observations to achieve sub-meter to centimetre level accuracy.

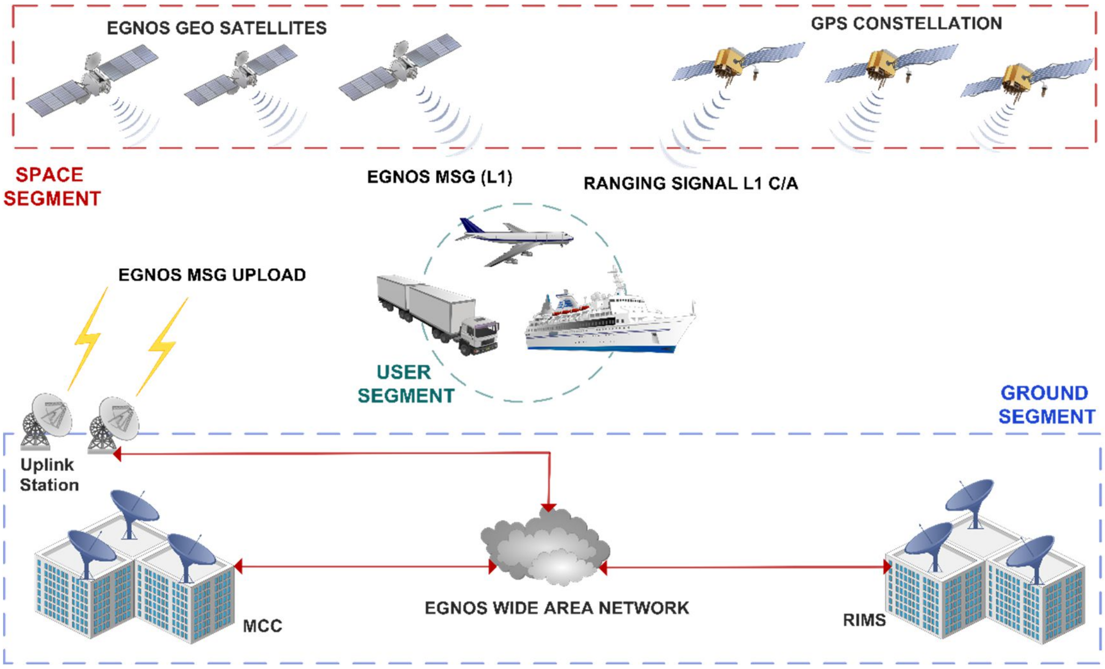

Figure 4-1: EGNOS System Architecture

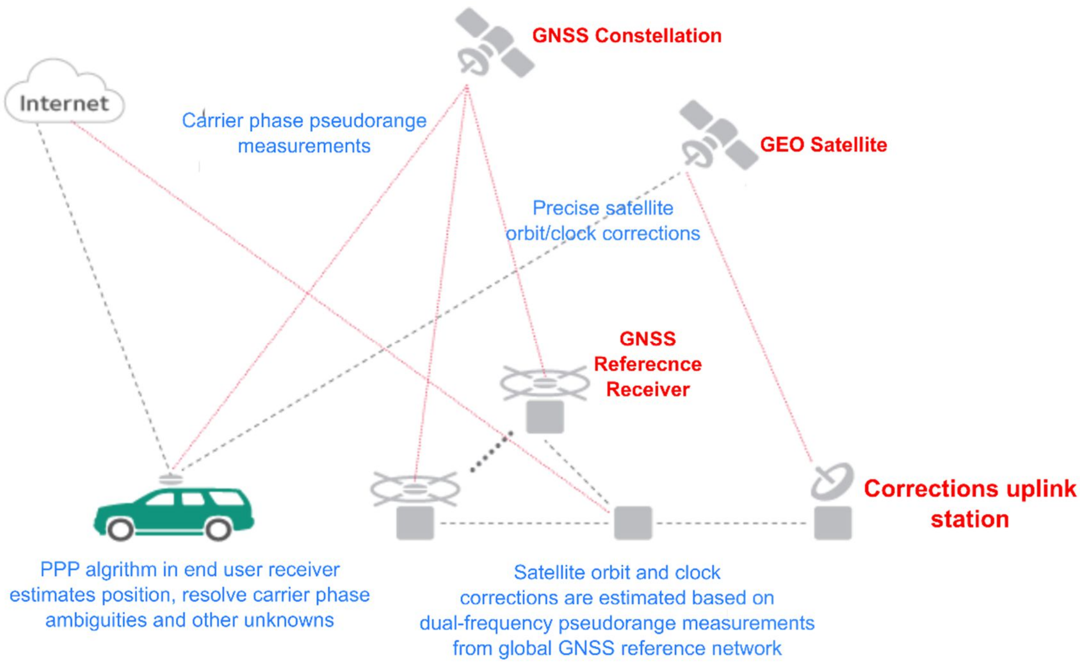

Figure 4-2: Depiction of Precise Point Positioning Service. Image courtesy Novatel [RD 20]

4.2.2.3 *Real Time Kinematic*

RTK is a relative positioning method that estimates the position of one receiver the rover relative to another receiver the base. If the location of the base receiver is precisely known in absolute sense, an absolute position of the rover can be estimated with centimetre level accuracy [RD 20]. Most GNSS error sources are common to both the rover and base receivers, and therefore can be mitigated by differencing measurements across receivers [RD 21], thus reducing the magnitude of the errors significantly. This is done by base station transmitting its raw carrier-phase pseudorange observations and base station coordinates to the rover in real-time and the rover uses both the rover and base observations to compute its position relative to the base as depicted in Figure 4-3.

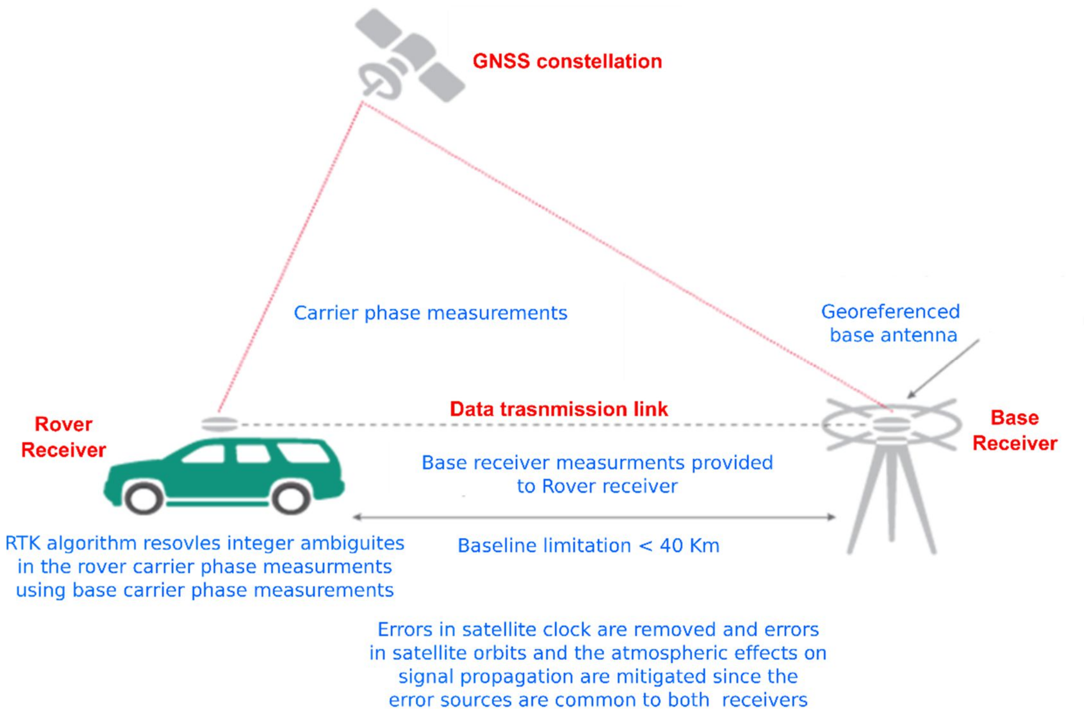

Figure 4-3: Typical RTK setup. Image courtesy Novatel [RD 22].

RTK system is generally classified as Single Baseline and NRTK. A single baseline RTK comprises of single base station serving one or more rovers. The single baseline RTK station can be personally/privately owned or a part of CORS. A NRTK is based on a network of reference receivers, which collects GNSS observations and sends them in real- time to a CPS. The CPS then combines the observations from all (or a subset) of the reference receivers and computes a network solution. From this network solution, the observation errors and their corrections are computed and broadcast to rovers within the working bounds of NRTK.

There exist several methods to compute NRTK solution, for instance, VRS, MAC, and FKP [RD 23]. NRTK approach reduces the distance dependent errors, consequently, improving the accuracy, reliability, and operating range [RD 24]. Figure 4-4 shows the depiction of single baseline and NRTK appr0oach. The black dots represent single baseline base station, whereas the blue circles represent the operating range. In case of single baseline approach, user A is provided with RTK correction within a given area. In NRTK approach, all five single baselines would operate together in providing NRTK solution even if the user B is not within operating range of each individual base station..

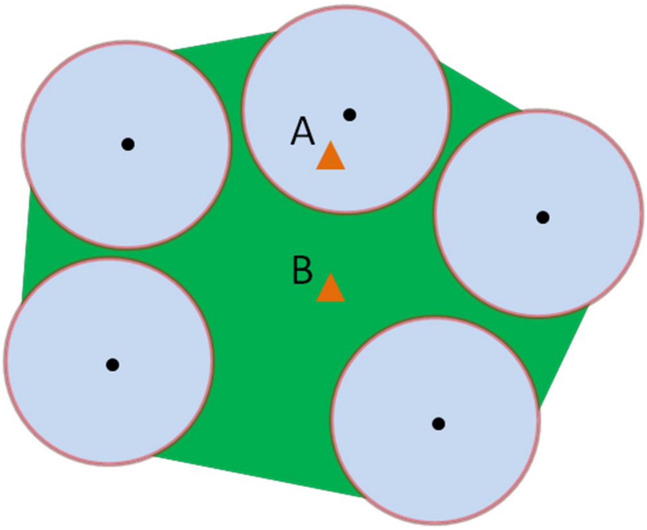

Figure 4-4: Depiction of Single baseline and NRTK approach

4.2.2.3.1 Single Baseline RTK Versus NRTK

It has to be remarked that similar positioning accuracies can be achieved with single baseline RTK and Network RTK approaches; however, the differences between the two RTK approaches are related to increased productivity, cost reduction, and operating range. The choice of RTK approach depends on the user operational requirements such as:

Base station:

Single baseline RTK approach using a personally/privately owned base station requires the purchase, maintenance, monitoring, and setup of base station by precisely estimating base station coordinates. This requires cost and related technical challenges for novice users. On the other hand, single baseline CORS or NRTK approach provides the end-user to avoid the base station installation and challenges associated with it at the cost of service subscription. In this regard, the single baseline CORS or NRTK offers plug-and-play service to the end-user thus avoiding the cumbersome issues. It has to be remarked that the user needs paid subscription to use NRTK. Section 5.3.2 enlists private networks that offer NRTK solution based on user subscription. In case of CORS, there are public networks available that offer free-of-charge service as discussed in Section 5.3.1

Communication link:

The communication link plays a vital role in base-rover RTK scenario since the raw carrier-phase observations or RTK correction (in case of NRTK) from base stations must be available anywhere anytime using a dedicated communication channel. Single baseline CORS and NRTK rely on the use of Internet (via cellular networks) for raw carrier-phase observations or correction broadcast, while single baseline personally/privately owned RTK approach opt for VHF/UHF radio link for raw carrier-phase observations transmission because, unlike cellular modem, UHF/VHF radio transceiver is cheap and offers plug-and-play solution. However, the use of radio links in single baseline personally/privately RTK approach limits the coverage and reliability of transmission and on top of that the end-user has to deal with spectrum licensing issues. Nevertheless, a single baseline personally owned RTK approach could be an optimal choice for users that do not find single baseline CORS or NRTK in the area of operation.

Operating range:

Operating range refers to the maximum separation between base and rover sites, which is termed as baseline length. The rover accuracy degrades and RTK initialization time increases when the range from the base station increases. Generally, factors such as distant-dependent errors determine RTK baseline length. NRTK approach aims to reduce the distance dependent errors using variety of techniques, and therefore supports larger baseline compared to single baseline RTK approach. Assuming a dual-frequency receiver, a single baseline RTK operates within 40 Km range, whereas *NRTK offers larger baseline length beyond 40 Km*. In case of single frequency receiver, the baseline generally reduces below 10 Km.

4.2.2.3.2 Critical factors affecting RTK accuracy

Base/rover receiver and antenna type

The receiver uses a state-of-the-art tracking scheme to collect carrier-phase pseudorange measurements. The quality of pseudorange measurements depends on the receiver processing and antenna type. Together with an appropriate receiver and antenna, carrier-phase measurement errors can be reasonably reduced, which would improve the RTK solution fix at the rover.

Base station coordinate accuracy

Because an absolute positioning is needed (see system requirement SR-0210 as in [RD 8]), therefore the base station coordinate accuracy directly impacts the rover accuracy. Incorrect or inaccurate base station coordinates degrade the rover position estimate [RD 20]. It is estimated that every 10 meters of error in the base station coordinates introduces one ppm error in the baseline vector. This implies that if the base station coordinates have a height error of 50 m, and the baseline vector is 10 km, then the additional error in the rover location is approximately 5 cm, in addition to the typical specified error. One second of latitude represents approximately 31 m on the earth surface; therefore, a latitude error of 0.3 seconds equals a 10 m error on the earth's surface. The same ppm error applies to inaccuracies of the base station's latitude and longitude coordinates.

Number of visible satellites

The number of available satellites for position estimation is tied to the quality of position estimate. The better the satellite geometry, the better would be estimated position solution. At least four satellites are required for 3-dimensional position coordinates. RTK initialization demands that at least 5 common satellites must be tracked at base and rover sites. Once initialization has been performed, a minimum of 4 continuously tracked satellites must be maintained to produce an RTK solution. Tracking additional satellites will aid in the RTK solution.

Environmental factor

Environmental factors, for instance, ionosphere and troposphere, strongly impact the quality of carrier-phase pseudorange measurement. These errors should be reduced to the best possible level to achieve better RTK accuracy and availability. In addition, errors local to rover receiver such as multipath and in-band interference, which cannot be removed using RTK, should be minimized and/or mitigated at the rover receiver to improve the rover positioning accuracy."

Baseline vector length

Generally, the RTK position solution accuracy degrades and initialization time increases when the baseline vector length between base and rover increases. The baseline vector length depends on distance-dependent error reduction. For dual-frequency receiver, typically 1 ppm of error in position adds up over a baseline vector of 1 km, this implies that position error of 1 cm adds up if the baseline vector is 10 km. More details are reported in [RD 64] and [RD 65]

4.2.2.4 Performance comparison of PPP and RTK

As stated in previous sections, both PPP and RTK techniques offers centimetre-level positioning accuracy under the conditions discussed in Section 4.2.2.5. The outlining difference between the two methods is that RTK provides position solution relative to a fixed reference station, whereas PPP provides position solution using globally applicable error corrections i.e. precise satellite orbit and clock products. This principle difference between the two techniques leads to varying error correction model used by RTK and PPP for position solution as outlined in Table 4-1. Consequently, the performance offered by these two techniques relies on several parameters as indicated in Table 4-2.

Table 4-1: PPP/RTK Error corrections and models requirement

Pseudorange error correction type	PPP	RTK
Space Segment Errors		
Precise Satellite orbit and clock corrections	Required	Not required
Group delay differential	Required for Single Frequency Receiver	Not Required
Satellite antenna phase wind-up error	Required	Not required
Relativity term	Required	Not required
Atmospheric Errors		
Ionospheric delay	Required (L1/L2 combination)	Required (L1/L2 combination)*
Tropospheric delay	Required	Not required
Geophysical Models		
Solid earth tide displacement	Required	Not required
User Segment Errors		
Receiver antenna phase wind-up	Required	Not required

*Due to ionospheric error elimination using dual-frequency combination, dual-frequency rover is would operate over longer baselines, whereas single-frequency rover would perfrom within shorter baselines.

4.2.2.5 Choosing the right solution

The choice of right solution between PPP and RTK depends on several factors, which is mainly a trade-off between the operational simplicity and global availability of PPP and the positioning accuracy and fast initialization of RTK.

4.2.2.5.1 Accuracy

The accuracy difference between RTK and PPP is narrowing over the period of time, however, when accuracy is the primary demand of the user application, RTK would be the right choice. Unlike RTK, PPP requires a dual-frequency receiver for decimetric-level positioning accuracy. A single frequency PPP approach achieves decimetric-level (< 1 m) accuracy at the cost of convergence time of several hours [RD 25].

4.2.2.5.2 Initialization Time

The convergence time required to achieve the desired user accuracy is referred to as initialization time. Typical initialization time for dual-frequency PPP receiver ranges from 20 to 40 minutes depending on satellite-receiver geometry, precise orbit and clock products quality, user receiver multipath conditions, and user accuracy requirements. For RTK, initialization time is relatively shorter than PPP, and it depends on baseline length between base and rover. The initialization time difference between PPP and RTK may or may not have a large impact, depending on the application and user requirements.

Table 4-2: PPP and RTK performance criteria

Performance Indicator	PPP	RTK
Position Accuracy	*dm - cm*	*cm*
Initializaton Period	*Determined by convergence time. 30 – 40 minutes approx*	*Determined by base station setup time*
Solution Availability	*Anywhere, Anytime*	*Within base station baseline effective limits*
Correction broadcast medium	*L-band satellites/Internet*	*Typically Internet*

4.2.2.5.3 Solution Availability

Due to the global validity of precise satellite and clock products, PPP based solutions can be obtained anytime anywhere. In case of RTK, the baseline length limits the solution beyond a certain range. For instance, typical range between base and rover is approximately 40 Km for dual-frequency receiver, whereas for single-frequency receiver this range drops down to less than 10 Km. The solution accuracy degrades and initialization time increases beyond the approximate ranges mentioned above. Therefore, the user should take notice of these factors before using RTK for field operations.

4.2.2.5.4 Operational complexity

In terms of operational complexity, PPP offers the simplest choice. The user receiver either uses L-band or Internet to receive precise satellite orbits and clock products to perform PPP. The operational complexity of RTK depends on the choice of underlying RTK approach. In case of single baseline CORS or NRTK, there is no such operational complexity for the end user. The user receiver needs service access to CORS or NRTK. Unlike CORS, NRTK and PPP, single baseline personally owned RTK user needs to go through setting up the base and data link for raw carrier-phase observation transmission to the rover, which in turn increases the operational complexity.

5 GNSS RECEIVERS MARKET SURVEY

This section provides a market survey of various OEM GNSS receivers and antenna that can be integrated in RPAS taking in to account deployment constraints of power, size, and cost. Various OEM receivers from world leading GNSS manufacturers as well as upcoming low-cost OEM receiver brands are presented in this study, which offers decimetre to centimetre position accuracies.

5.1 GNSS OEM RECEIVERS

5.1.1 TOPCON

Topcon manufactures various OEM GNSS receivers with wide range of functionalities on-board receiver. A list of the OEM receivers and related characteristics are outlined in Table 5-1.

Table 5-1: Topcon OEM GNSS receivers

	TOPCON OEM	Positioning Accuracy [RMS]					Signal Tracking							Miscellenous			
		Metre		Sub-metre		Centimetre											
		Single Point L1	Single Point L1/L2	SBAS	DGPS	RTK	GPS	GLONASS	Galileo	BeiDou	SBAS	QZSS	Number of channels	Weight	Dimensions	Power consumption	Price range
Dual-Frequency	**B110** Multifrequency, dual-frequency RTK, low power		H: 1.2 m V: 1.8 m	H: 80 cm V: 1.2 m	H: 30 cm V: 50 cm	H: 10 mm + 1 ppm V: 15 mm + 1 ppm	L1, L2, L2C	L1, L2, L2C			+	+	226	< 20g	40x55x10 mm	1 W	
	OEM-1 Multifrequency, dual-frequency RTK, low power			H: 1 m [1] V: 1.5 m	H: 40 cm [1] V: 60 cm	H: 10 mm + 1 ppm V: 15 mm + 1 ppm	L1, L2, L2C	L1, L2			+		72	60 g	60x100x13 mm	1.8 W	
	Euro-112 Multifrequency, dual-frequency RTK, in-band interference rejection, on-board data logging (2GB)		H: 1.2 m V: 1.8 m	H: 80 cm V: 1.2 m	H: 30 cm V: 50 cm	H: 10 mm + 1 ppm V: 15 mm + 1 ppm	L1, L2, L2C, L5	L1, L2			+		144		112x100x14.7 mm	5 W	

1 CEP

5.1.2 NOVATEL

Novatel offers various OEM GNSS receivers that offer both PPP and RTK based positioning solutions.

Table 5-2 and Table 5-3 briefly outline characteristics of Novatel OEM GNSS receivers currently available in the market.

Table 5-2: Novatel OEM GNSS receivers 1/2

	OEM6 Series	Positioning Accuracy [RMS]							Signal Tracking							Miscellenous			
		Metre		Sub-metre		Centimetre													
				Novatel Correct™															
						PPP [1]													
		Single Point L1	Single Point L1/L2	SBAS	DGPS	Terrastar-L	Terrastar-C	RTK	GPS	GLONASS	Galileo	BeiDou	SBAS	QZSS	Number of channels	Weight	Dimensions	Power consumption	Price range
Dual-Frequency	OEM615	1.5 m	1.2 m	60 cm	40 cm			1 cm + 1 ppm	L1, L2, L2C	L1, L2	E1	B1	+	+	120	< 24 g	46x71x11 mm	< 1 W	€1,500 – €6,000 approx.
Dual-Frequency	OEM617	1.5 m	1.2 m	60 cm	40 cm			1 cm + 1 ppm	L1, L2, L2C	L1, L2	E1, E5b	B1, B2	+	+	120	< 24 g	46x71x11 mm	< 1 W	
Dual-Frequency	OEM617D	1.5 m	1.2 m	60 cm	40 cm			1 cm + 1 ppm	L1, L2, L2C	L1, L2	E1, E5b	B1, B2	+	+	120	< 24 g	46x71x11 mm	< 2 W	
Dual-Frequency	OEM628	1.5 m	1.2 m	60 cm	40 cm	50 cm	4 cm	1 cm + 1 ppm	L1, L2, L2C, L5	L1, L2	E1, E5a, E5b, AltBOC	B1, B2	+	+	120	< 37 g	60x100x9 mm	1.3 W	
Dual-Frequency	OEM638	1.5 m	1.2 m	60 cm	40 cm		4 cm	1 cm + 1 ppm	L1, L2, L2C	L1, L2	E1, E5a,E5b, AltBOC	B1, B2	+	+	120	< 84 g	85x125x14 mm	2.8 W	
Single-Frequency	OEMStar	1.5 m		70 cm	50 cm				L1	L1			+		14	< 18 g	46x71x13 mm	0.36 W	
	OEM6 Dev Kit	OEM6 dev kit allows quick and easy evaluation (and integration) of OEM6 receivers in custom applications. The estimated price is €700																	

1 Requires subscription

Table 5-3: Novatel OEM GNSS receivers 2/2

	OEM6 Series	Positioning Accuracy [RMS]							Signal Tracking							Miscellenous			
		Metre		Sub-metre		Centimetre													
				Novatel Correct™															
						PPP [1]													
		Single Point L1	Single Point L1/L2	SBAS	DGPS	Terrastar-L	Terrastar-C	RTK	GPS	GLONASS	Galileo	BeiDou	SBAS	QZSS	Number of channels	Weight	Dimensions	Power consumption	Price range
Dual-Frequency	OEM615	1.5 m	1.2 m	60 cm	40 cm			1 cm + 1 ppm	L1, L2, L2C	L1, L2	E1	B1	+	+	120	< 24 g	46x71x11 mm	< 1 W	€1,500 – €6,000 approx.
Dual-Frequency	OEM617	1.5 m	1.2 m	60 cm	40 cm			1 cm + 1 ppm	L1, L2, L2C	L1, L2	E1, E5b	B1, B2	+	+	120	< 24 g	46x71x11 mm	< 1 W	
Dual-Frequency	OEM617D	1.5 m	1.2 m	60 cm	40 cm			1 cm + 1 ppm	L1, L2, L2C	L1, L2	E1, E5b	B1, B2	+	+	120	< 24 g	46x71x11 mm	< 2 W	
Dual-Frequency	OEM628	1.5 m	1.2 m	60 cm	40 cm	50 cm	4 cm	1 cm + 1 ppm	L1, L2, L2C, L5	L1, L2	E1, E5a, E5b, AltBOC	B1, B2	+	+	120	< 37 g	60x100x9 mm	1.3 W	
Dual-Frequency	OEM638	1.5 m	1.2 m	60 cm	40 cm		4 cm	1 cm + 1 ppm	L1, L2, L2C	L1, L2	E1, E5a, E5b, AltBOC	B1, B2	+	+	120	< 84 g	85x125x14 mm	2.8 W	
Single-Frequency	OEMStar	1.5 m		70 cm	50 cm				L1	L1			+		14	< 18 g	46x71x13 mm	0.36 W	
	OEM6 Dev Kit	OEM6 dev kit allows quick and easy evaluation (and integration) of OEM6 receivers in custom applications. The estimated price is €700																	

1 Requires subscription

5.1.3 Trimble and Ashtech

Trimble offers variety of GNSS OEM receiver and PPP services, which are outline in in Table 5-4 and Table 5-5.

Ashtech, now integrated in Trimble, produces a number of OEM receivers that offers centimetre-level RTK positioning as outlined in Table 5-6.

Table 5-4: Trimble OEM GNSS receivers 1/2

Group	Ashtech OEM (Ashtech is now *Trimble Integrated Technologies*)	Positioning Accuracy [RMS]					Signal Tracking							Miscellenous			
		Metre		Sub-metre		Centimetre											
		Single Point L1	Single Point L1/L2	SBAS	DGPS	RTK	GPS	GLONASS	Galileo	BeiDou	SBAS	QZSS	Number of channels	Weight	Dimensions	Power consumption	Price range
Dual-Frequency	**MB100** L1 RTK (GPS+GLONASS), L1/L2 RTK (GPS only), Advacned multipath mitigation			50 cm	30 cm + 1 ppm [1]	H: 1 cm + 1 ppm [1] V: 2 cm + 1 ppm	L1, L2, L2C	L1			+		45	< 22g	46x71x11 mm	0.95 W	
Dual-Frequency	**MB800** Multifrequency, multiconstellation, RTK, fast initialization, advanced multipath mitigation			60 cm	30 cm + 1 ppm [1]	H: 1 cm + 1 ppm [1] V: 2 cm + 1 ppm	L1, L2, L2C, L5	L1, L2	E1, E5		+	+	120	61 g	100x80x13mm	2.4 W	

1 Steady state values for baselines < 50 Km after sufficient convergence time

.

Table 5-5: Trimble OEM GNSS receivers 2/2

Trimble OEM			Positioning Accuracy [RMS] [1]							Signal Tracking							Miscellenous			
			Metre		Sub-metre				Centimetre											
							Trimble RTX													
							PPP [2]													
	Model	Description	Single Point L1	Single Point L1/L2	SBAS	DGPS	RangePoint RTX	CenterPoint RTX	RTK[5]	GPS	GLONASS	Galileo	BeiDou	SBAS	QZSS	Number of channels	Weight	Dimensions	Power consumption	Price range
Single-Frequency	BD910	Multiconstellation, compact design for mobile applications, on-board multipath mitigation, low elevation tracking			H: 50 cm V: 85 cm	H: 25 cm + 1 ppm V: 50 cm + 1 ppm			0.8 cm + 1 ppm[3] 1.5 cm + 1 ppm	L1	L1	E1	B1	+	+	220	19 g	41x41x7 mm	1.1 W	
Dual-Frequency	BD-920-W3G	Multiconstellation, equipped with Wifi, 3G, and Bluetooth, on-board multipath mitigation, low elevation tracking			H: 50 cm V: 85 cm	H: 25 cm + 1 ppm V: 50 cm + 1 ppm			0.8 cm + 1 ppm[4] 1.5 cm + 1 ppm	L1, L2, L2C, L5	L1, L2	E1		+	+	220	54g	60x55x19 mm	1.3 W	
Dual-Frequency	BD-970	Multiconstellation, on-board multipath mitigation, low elevation tracking, compact form factor, improved RTK initialization			H: 50 cm V: 85 cm	H: 25 cm + 1 ppm V: 50 cm + 1 ppm			0.8 cm + 1 ppm[4] 1.5 cm + 1 ppm	L1, L2, L2C, L5	L1, L2	E1, E5a, E5b, E5AltBOC	B1, B2	+	+	220	62 g	100x60x11.6 mm	1.5 W	
Dual-Frequency	BD-930	Multiconstellation, on-board multipath mitigation, low elevation tracking, compact form factor			H: 50 cm V: 85 cm	H: 25 cm + 1 ppm V: 50 cm + 1 ppm			0.8 cm + 1 ppm[4] 1.5 cm + 1 ppm	L1, L2, L2C, L5	L1, L2, L3 CDMA	E1, E5a, E5b, E5AltBOC	B1, B2	+	+	220	< 30 g	51x41x7 mm	2.2 W	
Dual-Frequency	BD-930-UHF	Integrated 403-473 MHz receiver, compact form, ideal for mobile applicatoins			H: 50 cm V: 85 cm	H: 25 cm + 1 ppm V: 50 cm + 1 ppm			0.8 cm + 1 ppm[4] 1.5 cm + 1 ppm	L1, L2, L2C, L5	L1, L2, L3 CDMA	E1, E5a, E5b, E5AltBOC	B1, B2	+	+	220	< 60 g	60x55x15mm	2 W	
Dual-Frequency	MB-ONE	Configurable from L1 RTK to L1/L2 RTK, Trimble RTX support, low power, small form factor			H: 50 cm V: 85 cm	H: 25 cm + 1 ppm V: 50 cm + 1 ppm	H: 50 cm + 1 ppm[6]	H: 4 cm + 1 ppm[6]	0.8 cm + 1 ppm 1.5 cm + 1 ppm	L1, L2	G1, G2	E1, E5a, E5b, E5AltBOC	B1, B2	+	+	240	< 24 g	71x46x11mm	< 1.2 W	

1 Using Zephyr-2 antennas
2 Requires subscription to Trimble RTX service
3 Single baseline RTK < 5 Km
4 Single baseline RTK < 30 Km
5 RTK range for Dual-frequency model greater than 40 Km, Single-Frequency model up to 10 Km
6 95%/2-sigma

Table 5-6: Ashtech OEM GNSS receivers

	Ashtech OEM (Ashtech is now *Trimble Integrated Technologies*)	Positioning Accuracy [RMS]					Signal Tracking							Miscellenous			
		Metre		Sub-metre		Centimetre											
		Single Point L1	Single Point L1/L2	SBAS	DGPS	RTK	GPS	GLONASS	Galileo	BeiDou	SBAS	QZSS	Number of channels	Weight	Dimensions	Power consumption	Price range
Dual-Frequency	**MB100** L1 RTK (GPS+GLONASS), L1/L2 RTK (GPS only), Advacned multipath mitigation			50 cm	30 cm + 1 ppm [1]	H: 1 cm + 1 ppm V: 2 cm + 1 ppm [1]	L1, L2, L2C	L1			+		45	< 22g	46x71x11 mm	0.95 W	
Dual-Frequency	**MB800** Multifrequency, multiconstellation, RTK, fast initialization, advanced multipath mitigation			60 cm	30 cm + 1 ppm [1]	H: 1 cm + 1 ppm V: 2 cm + 1 ppm [1]	L1, L2, L2C, L5	L1, L2	E1, E5		+	+	120	61 g	100x80x13mm	2.4 W	

1 Steady state values for baselines < 50 Km after sufficient convergence time

5.1.4 SEPTENTRIO

Septentrio, one of the leading manufacturers of GNSS receivers and OEM boards, offers various high-end GNSS OEM receiver boards with RTK capabilities as listed in Table 5-7 and Table 5-8

Table 5-7: Septentrio OEM GNSS receivers 1/2

Septentrio OEM	Positioning Accuracy [RMS]							Signal Tracking							Miscellenous			
	Metre		Sub-metre			Centimetre												
					PPP													
	Single Point L1	Single Point L1/L2	SBAS	DGPS	Veripos [1]	Terrastar [2]	RTK	GPS	GLONASS	Galileo	BeiDou	SBAS	QZSS	Number of channels	Weight	Dimensions	Power consumption	Price range
Dual-Frequency																		
AsteRx-m Dual-Frequency, multiconstellation, compact low-power		H: 1.3 m V: 1.9 m	H: 60 cm V: 80 cm	H: 50 cm V: 90 cm			H: 0.6 cm + 0.5 ppm V: 1 cm + 1 ppm	L1, L2	L1, L2			+	+	132	< 40 g	47.5 x 70 mm	600 mW	€1000 – €8,000 approx.
AsteRx4 Dual-Frequency, multiconstellation, L-band tracking		H: 1.2 m V: 1.9 m	H: 60 cm V: 80 cm	H: 40 cm V: 90 cm	H: 6 cm V: 10 cm	H: 6 cm V: 10 cm	H: 0.6 cm + 0.5 ppm V: 1 cm + 1 ppm	L1, L2, L5	L1, L2, L3	E5a, E5b, AtlBoc, E6	B1, B2, B3	+	+	544	55 g	77 x 120 mm	1.6 W- 2.6 W	
AsteRx-m-UAS Easy inegration in to UAS, Plug compatible with Pixhawk, Ardupilot, low power		H: 1.2 m V: 1.9 m	H: 60 cm V: 80 cm	H: 40 cm V: 90 cm			H: 0.6 cm + 0.5 ppm V: 1 cm + 1 ppm	L1, L2	L1, L2			+		136	40 g	47.5 x 70 mm	0.7 W	

1 Subscription to Veripos service is required
2 Subscription to Terrastar service is required

.

Table 5-8: Septentrio OEM GNSS receivers 2/2

Septentrio OEM	Positioning Accuracy [RMS]							Signal Tracking							Miscellenous			
	Metre		Sub-metre		Centimetre													
					PPP													
	Single Point L1	Single Point L1/L2	SBAS	DGPS	Veripos [1]	Terrastar [2]	RTK	GPS	GLONASS	Galileo	BeiDou	SBAS	QZSS	Number of channels	Weight	Dimensions	Power consumption	Price range
Dual-Frequency																		
AsteRx-m Dual-Frequency, multiconstellation, compact low-power		H: 1.3 m V: 1.9 m	H: 60 cm V: 80 cm	H: 50 cm V: 90 cm			H: 0.6 cm + 0.5 ppm V: 1 cm + 1 ppm	L1, L2	L1, L2			+	+	132	< 40 g	47.5 x 70 mm	600 mW	€1000 – €8,000 approx.
AsteRx4 Dual-Frequency, multiconstellation, L-band tracking		H: 1.2 m V: 1.9 m	H: 60 cm V: 80 cm	H: 40 cm V: 90 cm	H: 6 cm V: 10 cm	H: 6 cm V: 10 cm	H: 0.6 cm + 0.5 ppm V: 1 cm + 1 ppm	L1, L2, L5	L1, L2, L3	E5a, E5b, AtlBoc, E6	B1, B2, B3	+	+	544	55 g	77 x 120 mm	1.6 W- 2.6 W	
AsteRx-m-UAS Easy inegration in to UAS, Plug compatible with Pixhawk, Ardupilot, low power		H: 1.2 m V: 1.9 m	H: 60 cm V: 80 cm	H: 40 cm V: 90 cm			H: 0.6 cm + 0.5 ppm V: 1 cm + 1 ppm	L1, L2	L1, L2			+		136	40 g	47.5 x 70 mm	0.7 W	

1 Subscription to Veripos service is required

2 Subscription to Terrastar service is required

5.1.5 North RTKite

The RTKite GNSS RTK receiver is a one of its kind module that gives the power and accuracy of a full double frequency satellite positioning system on a single module that is simple to integrate into any kind of solution or device. The key features of North RTKite

- 444 channel Double Frequency GNSS RTK
- Bluetooth for Navigation and Configuration
- Integrated SD Card, SIM Card and Mobile Modem
- Lightweight and compact ready for UAV integration
- Works as RTK Rover by UHF or Mobile Network
- Transmits as RTK Base by UHF or Mobile Network
- Supports external UHF and RF communications
- Real time millimetric position at 1, 5 and 10Hz

They key performance specifications of North RTKite are enlisted in Table 5-8.

Table 5-8: North RTKITE OEM Receiver Specifications

		Positioning Accuracy [RMS]				Signal Tracking							Miscellenous			
		Metre		Sub-metre	Centimetre											
		Single Point L1	Single Point L1/L2	DGPS	RTK	GPS	Galileo	GLONASS	Beidou	SBAS	QZSS	Number of Channels	Weight	Dimensions	Power Consumption	Price
Dual Frequency	North RTKITE			H: 0.25 m + 1 ppm V: 0.50 m + 1 ppm	H: 8 mm + 1 ppm V: 15 mm + 1 ppm	L1 C/A, L1C, L1E, L2C, L2E, L5	L1, L2	L1 C/A, L1P, L2 C/A, L2P		+		444	55 g	740 mm x 540 mm x 254 mm	2.8 W	2000 USD

5.1.6 UBLOX

Ublox launched, the first of its kind, a low-cost L1 RTK receiver NEO-M8P. It supports base and rover modes and provides centimetre-level accuracy using GPS and GLONASS satellite constellations. The salient features of NEO-M8P are outlined in the following table.

ublox OEM	Positioning Accuracy [CEP]				Signal Tracking							Miscellenous			
	Metre		Sub-metre	Centimetre											
	Single Point L1	Single Point L1/L2	SBAS	RTK	GPS	GLONASS	Galileo	BeiDou	SBAS	QZSS	Number of channels	Weight	Dimensions	Power consumption	Price range
Single-Frequency: NEO M8P L1 RTK, GPS and GLOSNASS, supports rover and base modes. C94-M8P evaluation board is readily available for rapid prototyping	2.5 m			2.5 cm + 1 ppm	L1	L1				+	72	21 g	71 x46x 8.1 mm	300 mW	€359 approx.

Table 5-9: Ublox NEO-M8P

5.1.7 NVS TECHNOLOGIES AG

NV08C-RTK-A, produced by RTKNVS Technologies Ag, is a single-frequency dual-constellation GNSS receiver that supports L1 RTK. The receiver module supports both base and rover modes and offers low power and compact form factor. The key features of NV08C-RTK-A are listed in Table 5-10.

5.1.8 NAVSPARK

Navspark offers S2525-BD-RTK receiver module, which offers *GPS* and *BeiDou* L1 RTK positioning. The module supports both base and rover modes, and accepts RTCM or SkyTraq raw data, from a base station, to estimate position solution with centimetre level accuracy. The estimated price range of navspark RTK module is $150-$350.

5.1.9 PIKSI

Piksi, developed by Swiftnav, is a GPS-only L1 RTK receiver, which offers centimetre-level accuracy. Piksi works in a base-rover configuration and uses UHF communication link for correction transmission between base and rover. The estimated price of Piksi base-rover configuration is €935.

Table 5-10: NVS technologies RTK receiver

	INVS Technologies OEM	Positioning Accuracy [RMS]				Signal Tracking							Miscellenous			
		Metre		Sub-metre	Centimetre											
		Single Point L1	Single Point L1/L2	SBAS	RTK	GPS	GLONASS	Galileo	BeiDou	SBAS	QZSS	Number of channels	Weight	Dimensions	Power consumption	Price range
Single-Frequency	NV08C-RTK-A L1 RTK, GPS and GLOSNASS, supports rover and base modes	2.5 m		< 1 m	1 cm + 1 ppm	L1	L1			+		2 x 32	21 g	71 x46x 8.1 mm	300 mW	

5.2 GNSS ANTENNA

The choice of GNSS antenna strongly impacts performance of GNSS receiver. This choice is tied to user position accuracy requirements and environmental conditions. Multipath and interference rejection, stable antenna phase centre, and antenna gain are among the key factors in choosing antenna. EASY-PV certainly has power and size constraints, which must be considered in choosing GNSS antenna to be integrated with RPAS. The GNSS antenna ranges from a patch antenna to high performance geodetic antenna with varying size, power, and cost.

5.2.1 PATCH ANTENNA

Patch antennas are low power, low-cost, and very compact, thus making them ideal for products with size and power constraints. Various solutions of patch antennas are available depending on single and multiple frequencies/constellations. Novatel, Trimble, Tallysman offers good performance (multipath/interference rejection and stable phase centre) with multiple frequencies and multiple GNSS support.

5.2.2 COMPACT GNSS ANTENNA

In addition to patch antennas, there are several other antennas that are compact in size yet offering high performance such as Novatel ANT series, Trimble AV series, and Tallysman.

5.2.3 HIGH PERFORMANCE PINWHEEL ANTENNA

Pinwheel antennas from various manufacturers such as Novatel, Leica, and Trimble offers performance equivalent to that of professional survey-grade antennas but with low power and small form factor. The pinwheel antennas are resistant to multipath, interference, and antenna phase centre variations, thus supporting high positioning accuracies even in challenging user environmental conditions.

5.3 REAL-TIME RTK NETWORK

Real-time RTK network is a network of GNSS CORS that processes carrier-phase pseudorange measurements and provide RTK correction or raw carrier-phase observations to rover(s) in RTCM format [RD 26]. These corrections are either produced using a Network approach or a single base approach. This section focuses on the availability of real time networks that provides RTK correction and not on the RTK approach offered by the networks.

Real time RTK networks are maintained by both public and private organizations. The service offered by private organizations is based on subscription policy. The following subsections briefly discuss the details of public and several private RTK networks.

5.3.1 PUBLIC NETWORK

5.3.1.1 EUREF

The EPN is a voluntary federation of over 100 self-funding agencies, universities, and research institutions in more than 30 European countries. The EUREF set up and maintains a real-time GNSS infrastructure on the Internet using stations of its European GPS/GLONASS EPN. EUREF pilot-project EUREF-IP [RD 27] disseminates Differential GPS corrections (DGPS), raw GNSS data, and RTK correction using NTRIP. NTRIP is an HTTP based application-level protocol streaming GNSS data over the Internet [RD 28]. The primary entity of NTRIP is an Internet Broadcaster. EUREF broadcaster currently provides access to about 129 real-time data streams. The distribution map of the real time GNSS data streams from EUREF-IP NTRIP broadcaster is shown in Figure 5-1.

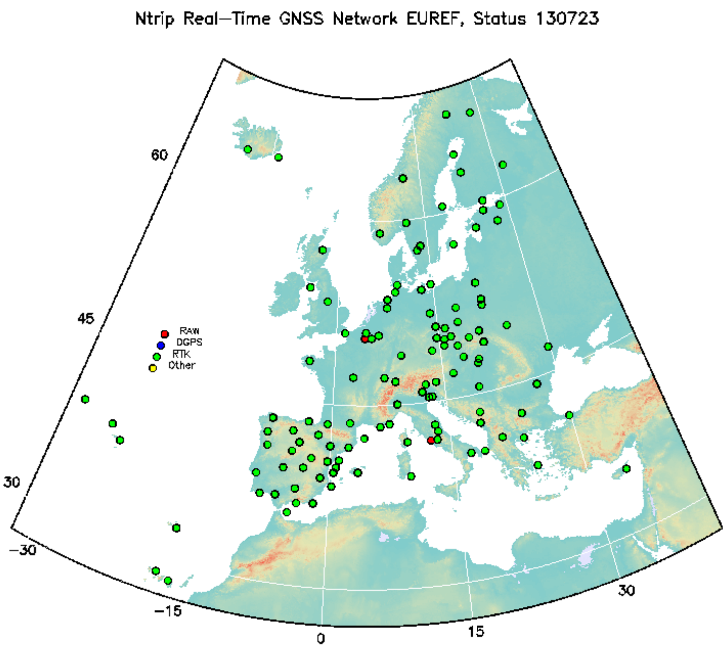

Figure 5-1: EUREF Real-time RTK Network. Source EUREF

5.3.1.2 EGNOS Data Access Service

EGNOS supports access of correction data in real time through its Internet based application EGNOS Data Access Service (EDAS) [RD 29]. It provides real time and historic data that include:

- The GPS, GLONASS, and EGNOS GEO observations and navigation data collected by the entire network of RIMS (A, B) and NLES. The location of RIMS and NLES is shown in Figure 5-2. The data collected by RIMS include dual-frequency GPS, GLONASS L1, and EGNOS L1 pseudorange observations, whereas the data collected by NLES includes only GPS data.
- Differential GNSS and RTK messages.
- EGNOS augmentation messages.

EDAS NTRIP service disseminates in real time GPS/GLONASS data collected from EGNOS network in RTCM format. Table 5-11 outlines the EDAS NTRIP message types provided in various RTCM formats.

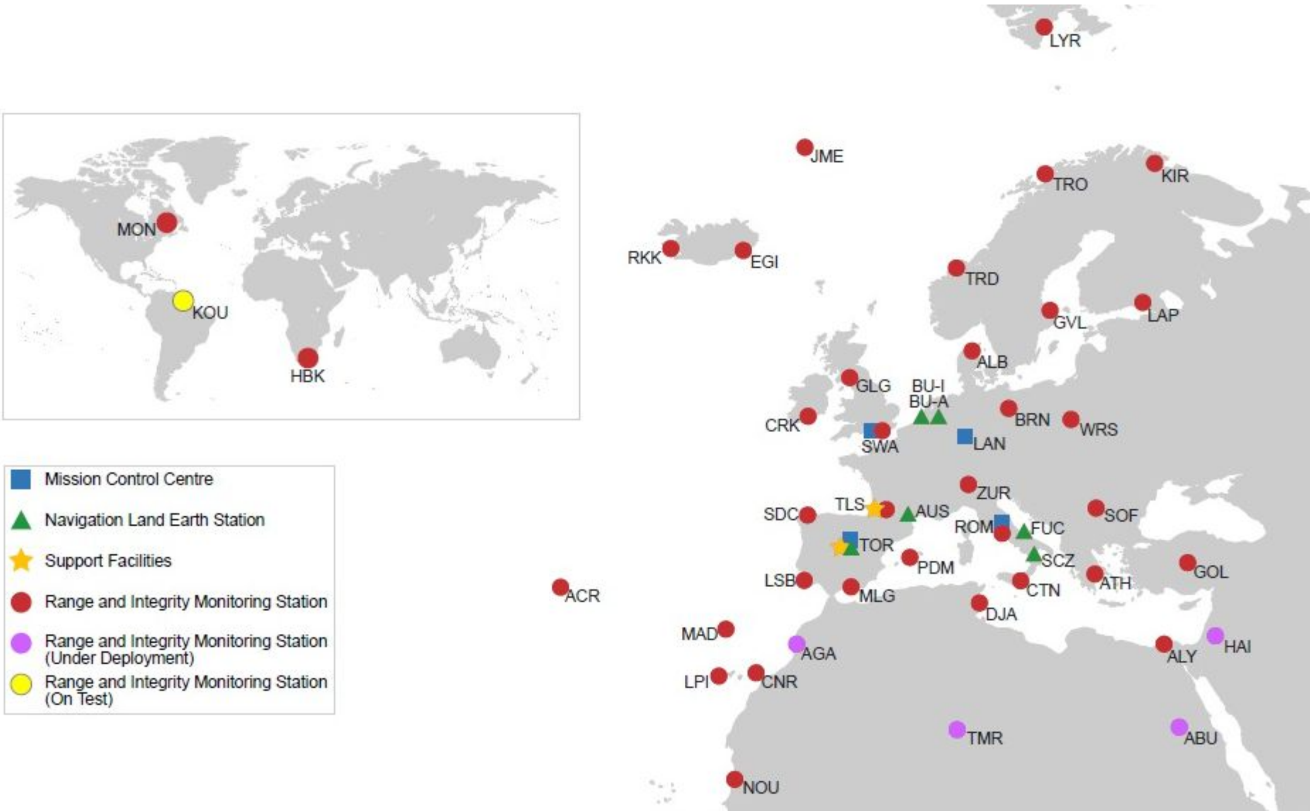

Figure 5-2: EGNOS Network. Source EGNOS SoL SDD v.2.0

Table 5-11: EDAS NTRIP RTCM Message Types

Message Description	RTCM Message Format		
	v. 2.1	v. 2.3	v. 3.1
Differential GPS Correction	1	1	N/A
GPS Reference Station Parameters	3	3	N/A
Reference Station Datum	N/A	4	N/A
RTK Uncorrected Carrier Phases	18	18	N/A
RTK Uncorrected Pseudoranges	19	19	N/A
Extended Reference Station Parameters	N/A	22	N/A
Antenna Type Definition Record	N/A	23	N/A
Antenna Reference Point (ARP)	N/A	24	N/A
Differential GLONASS Corrections	N/A	31	N/A
Differential GLONASS Reference Station Parameters	N/A	32	N/A
Extended L1 & L2 GPS RTK Observables	N/A	N/A	1004
Stationary RTK Reference Station ARP	N/A	N/A	1005
Antenna Description	N/A	N/A	1007
L1-Only GLONASS RTK Observables	N/A	N/A	1010
Auxiliary Operation Information	N/A	N/A	1013
GPS Ephemerides	N/A	N/A	1019
GLONASS Ephemerides	N/A	N/A	1020

5.3.2 PRIVATE NETWORK

5.3.2.1 Topcon TopNETLive

In addition to GNSS receiver, Topcon offers Network RTK, single baseline RTK, DGNSS correction services using TopNETlive. Topcon ToPNETlive is a subscription based, real-time GNSS reference network delivering high quality GPS/GLONASS correction data to a rover that accepts RTCM corrections. TopNETlive is available in majority of the European countries. In Italy, NetGEO, an Italian GNSS permanent stations network, set up by Geotop, provides the service.

5.3.2.2 Trimble

Trimble offers various RTK correction services such as VRSNow and CentrePoint based on user subscription. The GNSS receiver should be compatible with the RTK corrections provided through L-band or Internet. In case of VRSNOW, the corrections are compatible with any GNSS receiver accepting RTCM format, whereas

CentrePoint requires proprietary GNSS receivers. Trimble VRSNOW available in several countries, whereas, CentrePoint provides full coverage in all the European countries.

5.3.2.3 Leica

Leica SmartNet service offers GNSS RTK corrections based subscription policy. SmartNet users can expect centimeter-level accuracies tied to a common datum. Quality of service is guaranteed through our highly sophisticated data center and monitoring systems. Figure 5-3 shows SmartNet service availability in the Europe.

Figure 5-3: Leica SmartNet service availability in the Europe

6 SYSTEM SOURCES OF ERRORS

The aim of this chapter is to outline the possible sources of error envisaged at this stage for the algorithm design and implementation. Due to the complexity of the matter, an empirical evidence of the proposed approach will be provided by means of different end-to-end on-field tests to be presented in the next issue of the document.

Nevertheless, this chapter has been written to provide an internal assessment about possible sources of errors for internal understanding of the most critical items in case of further analysis. Therefore, when possible, for each source of error an expected value is reported from literature or datasheet of the COTS to be used.

In order to achieve a high degree of automation in EASY-PV project, all operations shall be automated as much as possible, from the inspection on the field up to the automatic generation of final report at service center side. The whole process encompasses different actors and tools across the whole system.

The most critical sources of errors are represented by the RPAS images acquisition on-field which may affect the final solution.

Potential sources of errors that might affect the final 2D horizontal accuracy needed for anomaly detection are hereafter reported:

1. Ground sampling distance estimation
    a. Height and Inclination PV Modules (non coplanarity)
    b. Height of the drone: altimeter resolution
2. Nadiral acquisition implementation: Gimbal Accuracy
3. Sensor Lens Distortion (focal length distortion)
4. Computer vision implementation
    a. Algorithm implementation detection and tracking in optical
    b. Algorithm quantization
5. GNSS Accuracy Positioning

Each source of error identified is detailed in the following paragraphs.

6.1 GROUND SAMPLE DISTANCE (GSD)

Ground sample distance (GSD) is the distance between pixel centers measured on the ground. For example, in an image with a one-meter GSD, adjacent pixels image locations are 1 meter apart on the ground. GSD is a measure of one limitation to image resolution, that is, the limitation due to sampling.

Table 6-1 shows the rectangular swath dimension and resolution, evaluated at different height with no sensor lens distortion; each pixel is assumed to have the same dimension at NADIR or at Swath limits.

			CAMERA RESOLUTION 640 pixel (9mm)	*CAMERA RESOLUTION 512 pixel (9 mm)*	
RPAS HEIGHT [m]	CAMERA FOV (half angle W) [°]	CAMERA FOV (half angle H) [°]	GROUND SWATH (l_W) [m]	GROUND SWATH (d_H) [m]	GSD RESOLUTION [m/pixel]
10	31	26	6,004873622	4,874478456	**0,01876523**
20	31	26	12,00974724	9,748956911	**0,03753046**
30	31	26	18,01462087	14,62343537	**0,05629569**
40	31	26	24,01949449	19,49791382	**0,07506092**
50	31	26	30,02436811	24,37239228	**0,09382615**

Table 6-1: Swath dimension and resolution

At a given height of 20 metres from panels the GSD resolution is about 3,7 cm/pixel and the swath is 24,02 x 19,48 m^2.

The PV panels, with the assumptions previously reported, exhibit a cross section of 133 cm x 100 cm for each panel (for longitudinal mount) or 83 cm x160 cm (for transversal mount).

6.1.1 NON COPLANARITY OF PV PANELS

The PV modules can be deployed in different configurations (e.g., on ground, on rooftop, …), therefore it is important to assess the difference in height from the PV panels and the height were the RPAS has been switched on (likely, on the ground). Also inclination impacts adding errors in the acquired image. These parameters

6.1.1.1 Height of PV modules

The height of PV modules from the ground may be affected by subjective estimation from the pilot if no information is provided before the RPAS operations.

However, it is very likely that the height of PV modules on the rooftop of a known height building, or on measurable structures on ground, can be reported with good accuracy.

The current analysis reported in §7.1.1.3.2 about panels form factor, mitigate the errors deriving from PV Panels and RPAS relative distance. Minimum and Maximum altitude shall be given for best GSD resolution.

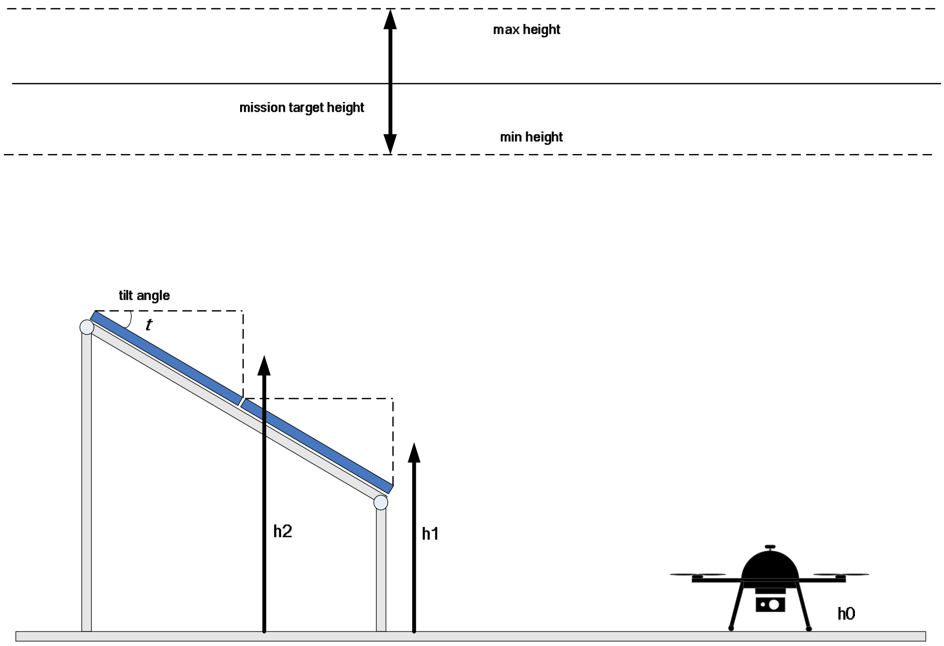

Figure 6-1: different PV Panels heights and Mission target height

A target height is suggested to the pilot from the Service Centre as ancillary information, when the Mission "Flight Plan" is defined.

6.1.1.2 Inclination (Tilt angle) of PV modules

Also Inclination causes both the surface of PV panels to be distributed ad different height (see also Figure 6-1) and a panel cross section reduction impacting the accuracy requirement SR.0210 as in [RD 8].

PV Panels are deployed with different installation strategies such as fixed (all year), adjustable (2 or 4 seasons) or trackable to maximize sun irradiation. The PV panels inclination is basically a function of the PV plant latitude. For medium latitudes (φ=40°), panels in a fixed configuration will be tilted of the following angle [RD 18], [RD 19]:

$$\beta = 0.76 * \varphi + 3.1^\circ = 33.5^\circ$$

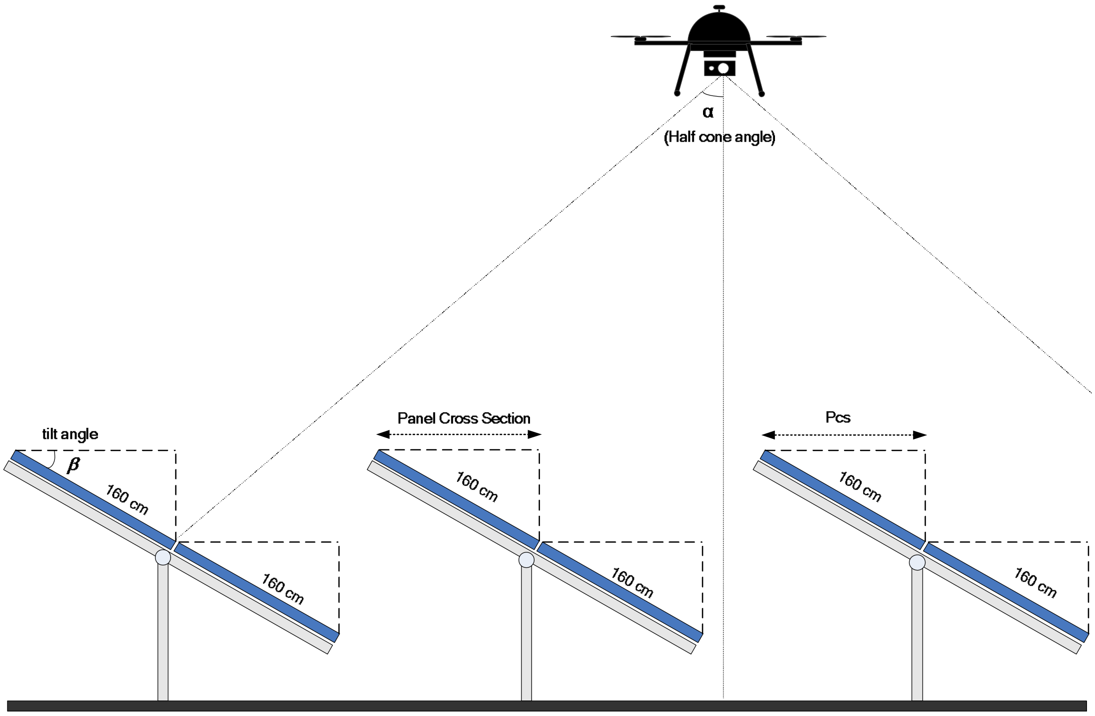

Figure 6-2: PV Panel cross section during RPAS operations

Different scenarios have been taken into account in the first error sources assessment (panels on rooftop with fixed tilt angle, trackable Panels, etc,…). The most likely configuration for the scenarios taken into account, in the two main target countries (**Italy** and **Germany**) is "fixed panels" whith φ varying from 38° to 50°.

The Panel Cross section seen by the RPAS (considering φ=40°) is:

$$Pcs = 160\ cm * \cos(\beta) = \ 133\ cm$$

if the Panel is mounted on longitudinal side, or

$$Pcs = 100\ cm * \cos(\beta) = \ 84\ cm$$

if the Panel is mounted on transversal side.
However the considerations performed in §2.3.2 about Panel's automatic inclination detection, simplify and mitigate the errors involved in this section.

6.1.1.3 Panel dimensions and inclination form factor

The panel dimensions and inclination form factor have been introduced to enhance panels positioning performances.
In fact, considering the dimension of a PV panel which has standard dimensions of 160 cm x 100 cm it is introduced:

$$\rho = \frac{160\ cm}{100\ cm} = 1{,}6$$

$$\text{Panel inclination index} \begin{cases} \rho < 1{,}6 \\ \rho = 1{,}6 \\ \rho > 1{,}6 \end{cases}$$

If $\rho = 1{,}6$, The panel has no tilt angle inclination.

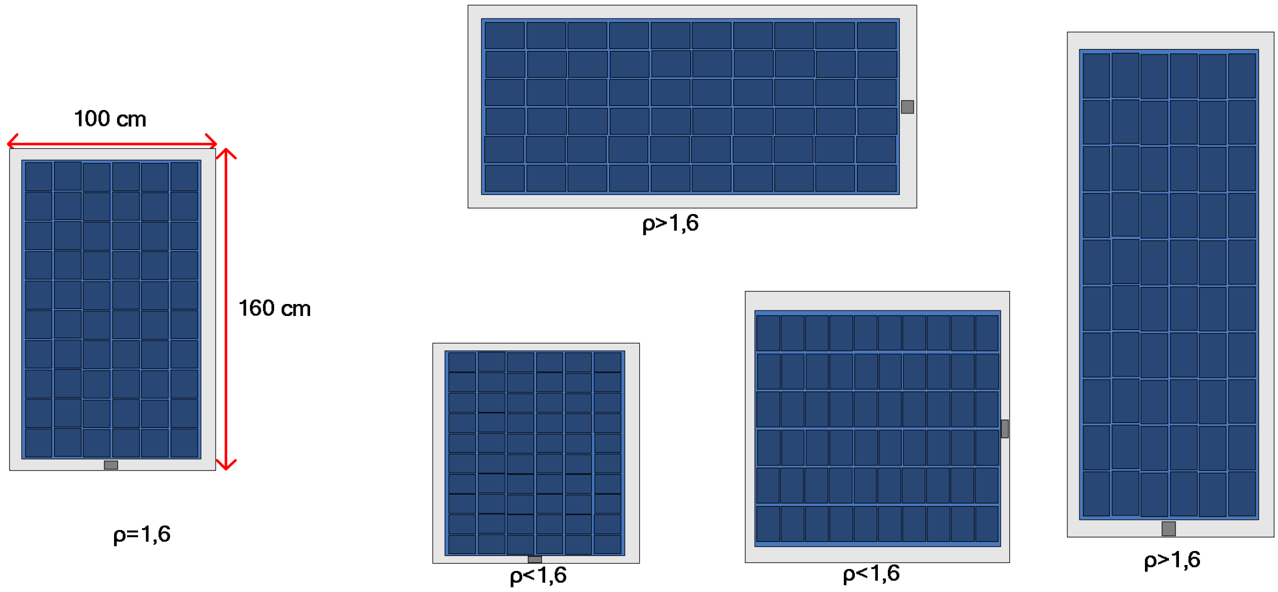

Figure 6-3: Panel inclination form factor

Panel dimensions can be always be configurable by user, by the default measure is 160x100 cm.

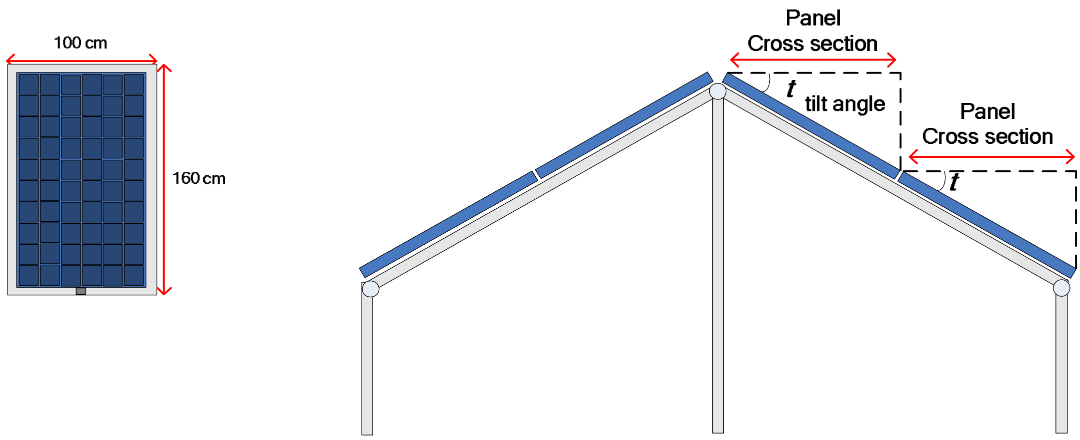

Figure 6-4: Automatic Panel inclination and cross section estimation.

The inclination (tilt angle) can be also calculated with the following formula:

$$\text{Tilt angle} \begin{cases} t = \arccos\left(\frac{\rho}{\rho_s}\right), & \rho < 1{,}6 \\ t = 0\,, & \rho = \rho_s = 1{,}6 \\ t = \arccos\left(\frac{\rho_s}{\rho}\right)\,, & \rho > 1{,}6 \end{cases}$$

where ρ_s is the panel inclination form factor of a standard panel with dimensions of 160 cm x 100 cm and 0° tilt angle.

Finally, we argue that the knowledge of actual panel dimensions allows to adjust the scale (i.e. the GSD parameter) of the acquired image so that height of PV module is no more a critical parameter. This theoretical outcome is analysed in section 7.1, where experimental evidences are documented.

6.1.1.4 Expected Impact

Following table summarises the expected impact of panel inclination and height as source of error for the EASY-PV algorithm.:

SOURCE	EXPECTED IMPACT SUMMARY
Inclination of PV panels	PV panels inclination is basically imposed by latitude constraint. Moreover, due to deployment aspects, this value may vary and it is not known in advance. Anyway, the knowledge of PV panel form factor allows the algorithm to be independent from PV panel inclination itself.
Height of PV panels	PV panels height is estimated with metric error. Anyway, the knowledge of PV panel dimensions allows the algorithm to be independent from PV panel height itself.

To experimentally confirm the above conclusion a specific test has been performed and described in section 7.1.1.3.1, where a comparison of the results obtained with the two different approaches is presented.

6.1.2 HEIGHT OR RPAS: ALTIMETER MEASUREMENT

The knowledge of RPAS height is important in the estimation of the WGS-84 2D positioning of PV Panels on ground as reported in chapter 2.3.1 and 2.3.2. RPAS multirotors uses barometer as primary sensor for height measurements. In normal RPAS operations when the RPAS is switched on, the Flight Management Unit handles the barometric pressure (e.g. 1015 hPa) value read by the barometer sensor as "height 0" (QFE – according to aeronautics Q codes*)*. The more the RPAS climbs, the less pressure is measured.

The altimeter in commercial civil RPAS (<25 kg) is typically composed by an analog barometric sensor with a 12 bit ADC converter which provides an overall resolution on the height of about 14 cm as raw measurement, apart from any other software improvement (Kalman filtering, ARMA techniques, etc…) performed by the FMU firmware. However, since altimeter is a very sensitive sensor some precautions shall be taken into account for the design of EASY-PV payload in case of pressure measurement on the payload:

- A temperature sensor shall be needed on the gimbal board for temperature calibration;
- The sensor shall be insulated from solar light and ventilation;
- A dual barometric sensor should be considered for the gimbal design phase in order to erase systematic errors on readings;
- In case of altitude readings from the primary RPAS communication bus, accuracy specification provided by the avionics constructor will be used.

6.1.2.1 Expected Impact

Following table summarises the expected impact of altimeter source of error for the EASY-PV algorithm.:

SOURCE	EXPECTED ACCURACY
Barometric sensor	Height (h) estimated with about 50 cm of accuracy (worst case). Anyway using the panel dimension information to adjust the acquired image scale (i.e. to evaluate the GSD), the knowledge of the altitude is no more a critical parameter

The current analysis performed on DJI SDK (Onboard SDK / Mobile SDK - [RD 4]) available on one of the target available RPAS platforms, allow direct reading of RPAS height on FMU primary communication BUS.

6.2 NADIRAL ACQUISITION IMPLEMENTATION: GIMBAL ACCURACY

EASY-PV payload shall be embarked on candidate compliant RPAS platforms [RD 5]; a 2 axis gimbal (Pitch and Roll) is sufficient to keep the thermal sensor at Nadiral position with respect to horizontal levelled alignment. (see § 2.3.1). The accuracy of gimbal is important to assess the WGS-84 positioning of PV panels on ground with a reasonable error.

Good COTS gimbals available on the market can reach fractions of degree spreading from 0.1 to 0.01° of accuracy.

6.2.1 EXPECTED IMPACT

Following table summarises the expected accuracy:1

SOURCE	EXPECTED IMPACT
Mechanical gimbal	Combined Pitch and Roll estimated with about 0.05° of accuracy (worst case). It causes an acceptable error in horizontal 2D accuracy when considering the drone flying at 20 meter altitude of about 20m*sin(0,05°)=2 cm

The usage of gimbal also makes the thermal sensor mass center (point A) moving w.r.t. the RPAS body including the GNSS antenna phase center (point B). Moreover, as a 2D positioning of thermal sensor is needed in order to geo-reference any acquired image, an offset between point A and B (also varying depending on the RPAs attitude) has to be considered.

6.3 SENSOR LENS DISTORTION

The distortion introduced by the IR and optical camera is reduced when using "narrow" FOV angles. At this stage a FLIR Vue Pro 640 camera (or FLIR TAU2) is foreseen to be embarked as primary sensor on the payload. The analysis cope with a TIR camera with 62° x 52° FOV and 9 mm lens optics. A rectangular swath on the ground is considered.

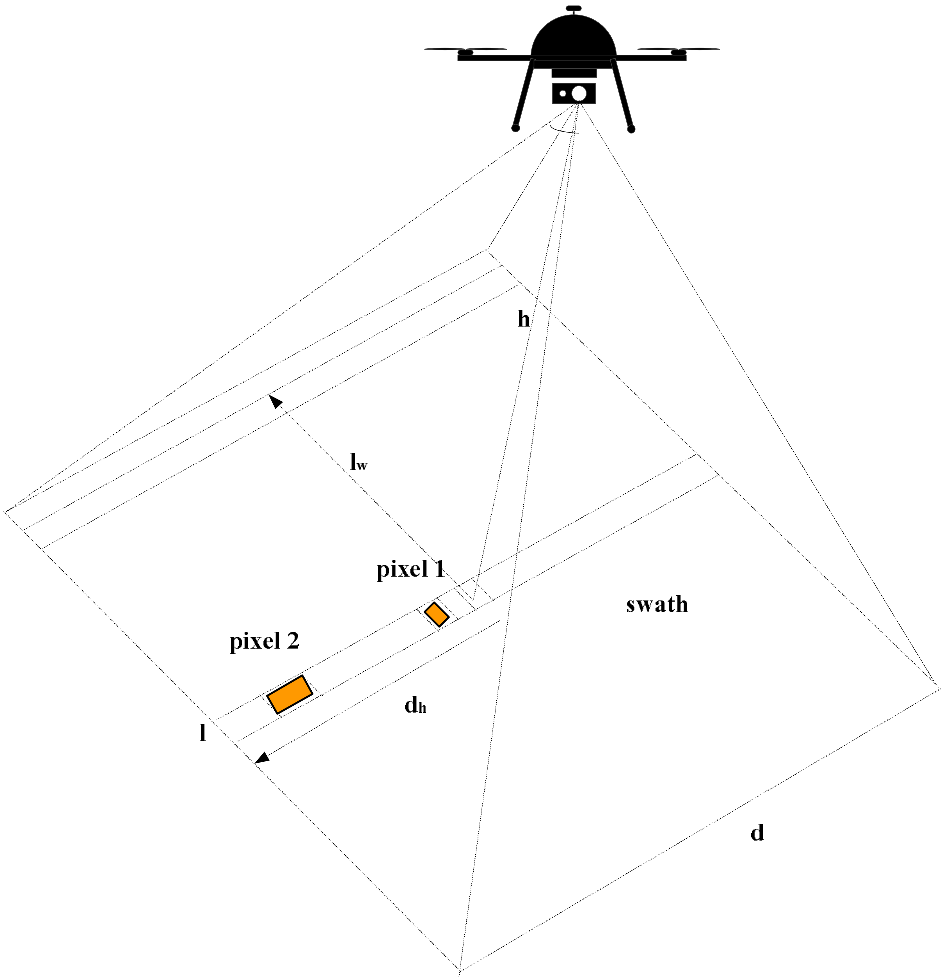

Figure 6-5: Rectangular Swath on the Ground

The swath is read (on the TIR sensor considered) on a CCD with a resolution of 640x512 pixel with a bit depth of 14 bit. The rectangular swath **l**x**d** on the ground has resolution expressed in cm/pixel (GSD) which is a function of the height of RPAS.

According with Figure 6-5, due to lens distortion, a pixel nearby the limits of SWATH (pixel 2) of RPAS may result in some distortion when compared to a pixel nearby the NADIR point (pixel 1).

The sensor lens distortion introduced is unknown at this stage (on-field experience suggests 9 mm or 13 mm lenses instead of 6.8 mm) and shall be further investigated in the test campaign. Additional specification from FLIR constructor such as CCD pixel distance expressed in micron, not included in commercial datasheet, can be used at this stage.

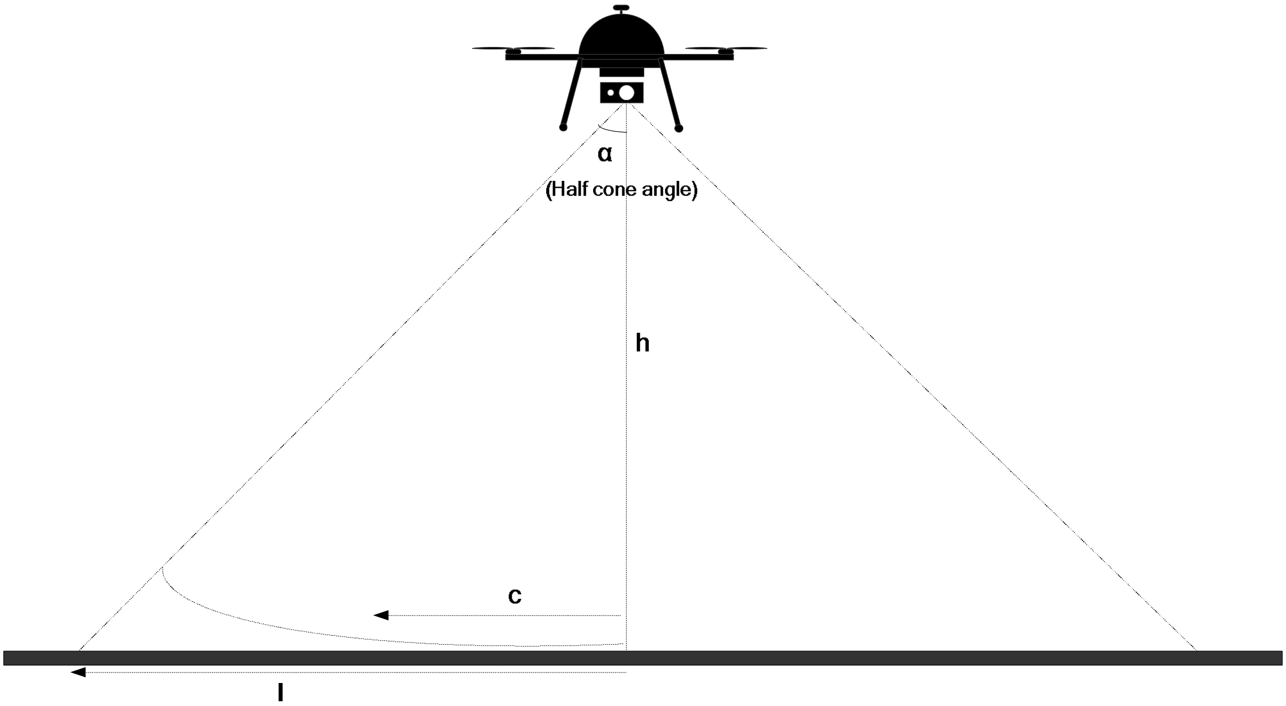

Figure 6-6: Lens distortion

From on-field operation experience, such distortion can be negligible or mitigated flying at low altitudes with narrow lens (e.g. 9 mm).

6.3.1 EXPECTED IMPACT

Following table summarises the expected accuracy:

SOURCE	EXPECTED ACCURACY
Lens distortion and resolution	Negligible. It is assumed to use only cameras after calibration process. Considering these operational configurations, error below order of cm are expected

The above assumption will be proven with a dedicated test where the calibration process will be performed with a specific SW.

6.4 COMPUTER VISION ALGORITHM

6.4.1 ALGORITHM DETECTION AND TRACKING

See section 3 with particular emphasis on 3.4 and 3.5 sections where the EASY-PV adopted solution is described.

6.4.2 ALGORITHM QUANTIZATION

At a given RPAS height of 20 meters from panel, the resolution of 1 pixel is given by the dimension of the rectangular swath on ground and the resolution of the sensor:

$$\delta_w = \frac{24{,}04\ m}{640\ pixel} = 3{,}7\ \mathrm{cm/pixel}$$

$$\delta_h = \frac{19{,}40\ m}{512\ pixel} = 3{,}8\ \mathrm{cm/pixel}$$

Therefore, the representation of a PV panel will appear on the sensor as:

$$Panel_w = \frac{100\ cm}{3{,}8\ cm/pixel} = 26\ \mathrm{pixel}\ ;\ Panel_h = \frac{133\ cm}{3{,}8\ cm/pixel} = 36\ \mathrm{pixel}$$

(PV Panels longitudinal mount)

$$Panel_w = \frac{83\ cm}{3{,}8\ cm/pixel} = 22\ \mathrm{pixel}\ ;\ Panel_h = \frac{160\ cm}{3{,}8\ cm/pixel} = 42\ \mathrm{pixel}$$

(PV Panels transversal mount)

The PV Panels are therefore represented, in the worst conditions with 22 pixels on the shortest side, with a transversal mount and an average inclination of 33,5°.

For better algorithm performances, lower heights shall be selected, resulting in a better PV Panels resolution and a lower number of Panels per frame (e.g. 15-20 PV Panels per Frame) which can reduce both pilot's workload and algorithm complexity of computations.

6.4.3 ANALYSIS OF THE COMPUTATIONAL LOAD

The second analysis is about the computational load needed by the computer vision algorithm and a suitable HW platform to run it. Such evaluation is required in order to assess the preliminary feasibility of the algorithm to process thermal images in real time.

The current version of the algorithm tested on a desktop computer and not yet integrated with the Panel Tracking module, consists of the steps previously described in the second chapter.

In this test it is analysed the time required by each processing phase in order to estimate the total computational load.

As described in §3, with respect to the normalization of the luminosity, the Canny algorithm for edge detection and the Hough transform (ref. §3.4) are applied on the whole image, so their computational complexity is an order of the image dimension **O(WxH)**, where W and H are respectively the width and the height of the image. On the other hand, the clustering of the lines has a computational load **O(L),** which increases linearly with the number of lines detected L.

Finally, the PV panels detection and tracking, along with the anomaly detection, require a processing time that grows linearly with the number of PV panels P in the scenes, so the computational complexity is **O(P).**

To be more accurate, we have to consider in this estimation also the time required by the Panel Tracking module for providing the coordinate translation between the image and the geocentric reference system. However, this time should be negligible (e.g. 100-200 ms) compared to the time required to process the image in order to detect the anomalies.

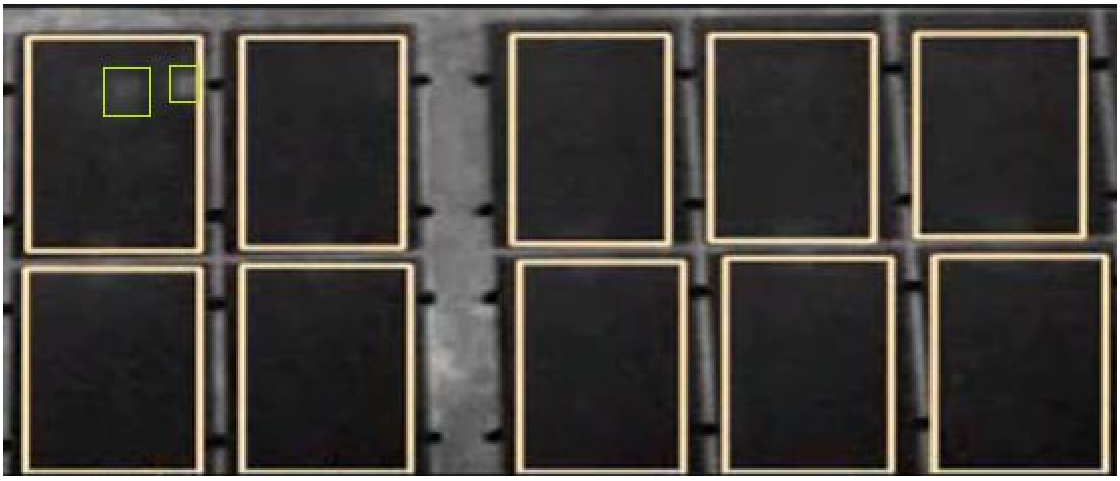

Figure 6-7: Example of anomaly detection in real time

The thermal video acquired during preliminary test activities have been used as input to carry out the following results.

The current version of the algorithm has been run with different video acquired with different resolutions and different RPAS heights, namely 1CIF (320x240) and 4CIF (640x480). The acquisition frame rate of the videos were about 9-10 fps. The processor used for the experiments is an Intel Core i5-3337U 1.8 GHz.

The experimental results, reported in Table 6-2, confirm that the computational load depends on both the image resolution and the number of detected panels. Moreover, we noted that the algorithm is able to process the images in real-time (10 fps) with a 1CIF resolution, but a drop in performance is reported when the algorithm deals with 4CIF images (5 fps).

Video resolution	Video frame rate	Processing frame rate (fps)	Thermal video maximum rate

(pixels)	(fps)		[Hz]
320x240	9-10	10	9
640x480	9-10	5	9

Table 6-2: *Preliminary Results of algorithm*

This encouraging results still suggest some more porting and testing activity of the algorithm on different HW boards (quad-cores, octa-cores, or GPU boards).

6.5 GNSS ACCURACY POSITIONING: COMPARISON OF POTENTIAL SOLUTIONS

KPIs as reported in section 4.1 are the key factors for considering the final GNSS solution for EASY-PV.

As discussed in Section 3, both PPP and RTK are two candidate GNSS solutions, which meet the 50 centimetre horizontal positioning accuracy requirement for EASY-PV as reported in [RD 8]. However, the cost associated with PPP solution is high compared to RTK. For instance, according to SR-0210 as in [RD 8], the prerequisites for PPP decimetric-level positioning include a dual-frequency GNSS receiver. Unlike PPP, RTK based centimetre-level positioning accuracy can be achieved even with single-frequency receivers.

In case of RTK based positioning, three different choices have been discussed, which are

- ✓ single baseline privately owned base station,
- ✓ single baseline CORS,
- ✓ NRTK.

Though, NRTK is a desirable choice due to its relatively large operating area (coverage) compared with single baseline RTK. However, it requires GNSS receivers, which are not low-cost, to operate NRTK algorithms stated in Section 4.2.2.3. Furthermore, users require paying for the NRTK service using a subscription-based policy. Thus, to reduce GNSS receiver cost and avoid user subscription fee, single baseline RTK privately owned and CORS are two potential GNSS solution which will be extensively examined for EASY-PV along with research activities proposed in the following section.

7 EXPERIMENTAL ACTIVITIES

This section includes experimental activities implemented in order to confirm theoretical outcomes and assumptions reported in chapter 6. Some critical items have been preliminary tested before to be injected in the EASY-PV target architecture. In other words, this section reports outcomes involving items under testing not yet integrated in the final EASY-PV architecture; such tests' results have a great importance as provide to the EASY-PV consortium the confidence that technical developments are under control. Moreover, this experimental activity anticipates the tests on EASY-PV architecture (planned from TRR to AR), contributing to reduce the criticality of such a phase.

According to the above logic, Table 7-1 summarises the experiments lead to confirm the theoretical sources of error analysis.

Error Sources		Test	Reference
GSD evaluation, ref section 6.1	Height and Inclination PV Modules (non coplanarity)	TEST_GSD.0010,	see section 7.1
	Height of the drone: altimeter resolution	TEST_GSD.0010, see section 7.1	
Nadiral acquisition implementation	Gimbal Accuracy	TEST_GIM.0010	see section 7.2
Sensor Lens Distortion (focal length distortion) and Resolution		TEST_SEN.0010,	see section 7.3
Computer vision algorithm	Algorithm implementation detection and tracking	TEST_VIS.0010	see section 7.4
	Algorithm quantization	No test	N.A.
	Analysis of computational load	No test	N.A.
GNSS Accuracy Positioning		TEST_GNSS.0010, TEST_GNSS.0020, TEST_GNSS.0030, TEST_GNSS.0040, TEST_GNSS.0050, TEST_GNSS.0060,	See section 7.5.

Table 7-1: Sources of error and relevant Experimental activities

7.1 GSD ESTIMATION

7.1.1 TEST_GSD.0010 PANELS DIMENSIONS ESTIMATION FROM RPAS

7.1.1.1 Objectives

A preliminary test was conducted on August 10th, 2016 in Castel Campagnano (CE) at "Centro L'Oasi" in order to verify the impact of errors foreseen in §4 and verify the correctness of the proposed approach.

The purpose of the first experiment is the validation of panel's dimensions using the only information available on the RPAS.

7.1.1.2 Activity description

A PV panel of known size (68 cm x 20,5 cm) has been placed at a given distance of 10,00 meters away from a reference point (a manhole) and various optical images have been taken at different heights.

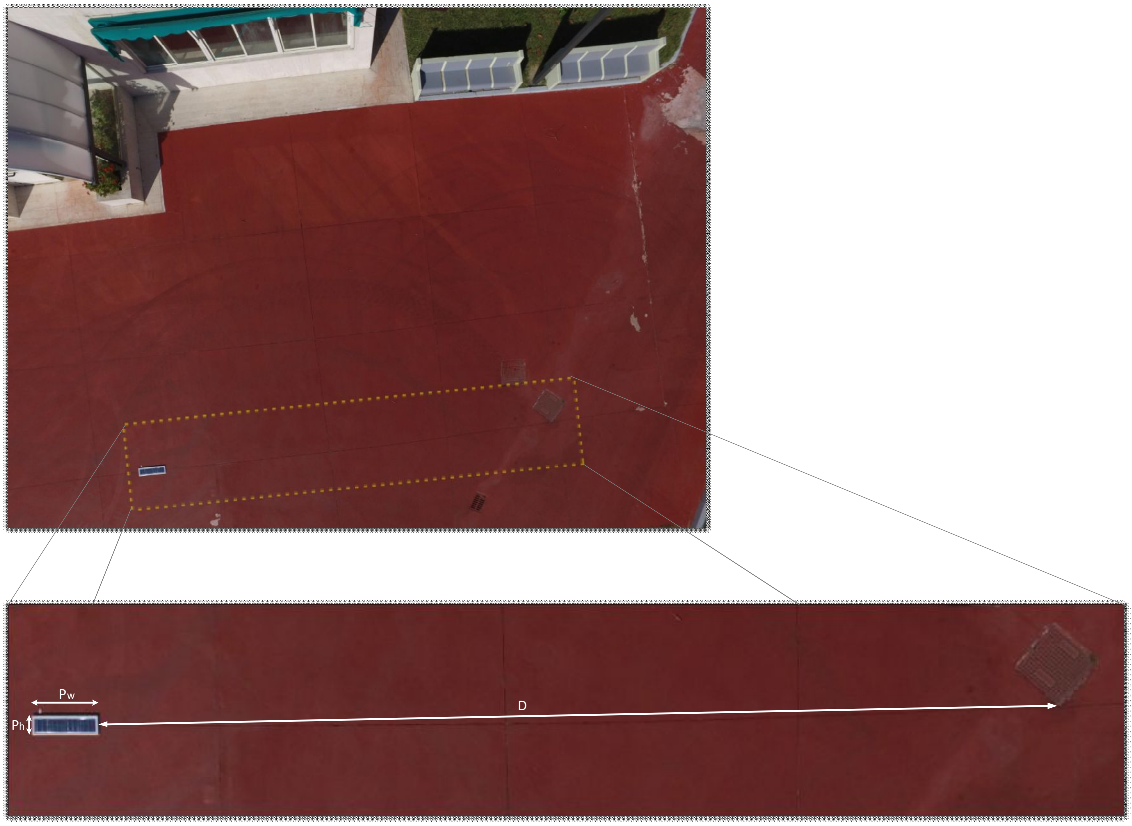

Figure 7-1: Test bed for the verification of the proposed approach

The RPAS used is the DJI Matrice 100 with a Zenmuse X3 gimbal and optical camera with a FOV of 84°, configured to record images with a resolution of 4000x3000 pixel in 4:3 format with the sensor in nadiral position.

Each picture is enriched with gimbal attitude metadata and GNSS position (Ublox M8N Multiconstellation only - no RTK) referred to the centre of the image.

Figure 7-2 : DJI MATRICE M100 with camera pointed in Nadiral position

7.1.1.3 Final Results

The performed test allowed to justify the theoretical assumption that knowledge about panels dimensions and form factor allow the EASY-PV algorithm to be independent to GSD parameter (varying as function of altitude and distance from the image center), generally needed to apply a scale factor to the acquired image.

Tests presented in the following 7.1.1.3.1 and 7.1.1.3.2 sections documents how the knowledge of GSD allow to evaluate the panel dimensions. Now if we image to know in advance the panel dimensions (as it is in the reality), GSD may be derived accordingly. According to the tests, even if GNSS RTK technique is not used nor the picture resolution has been corrected by SW, the approach to use the relationship $GSD = f(panel\ dimensions)$ seems to be reliable.

7.1.1.3.1 Estimation of PV panel dimension and distance from reference point

It is possible to find the GSD resolution using the field of view of the camera in combination with the image's dimensions, known a priori, and the RPAS height (extracted from the EXIF/XMP metadata embedded into images).

The size of the panel expressed in pixels and the distance from the reference point are detected; the equivalent dimensions in meters are calculated multiplying these values by the actual GSD. The results obtained for three images at different heights are illustrated in Table 7-2.

RPAS HEIGHT [m]	GROUND SWATH DIAGONAL (g) [m]	GSD RESOLUTION [m/pixel]	PANEL WIDTH (P_w) [pixel]	PANEL WIDTH (P_w) [m]	PANEL HEIGHT (P_h) [pixel]	PANEL HEIGHT (P_h) [m]	REF. POINT DISTANCE D [pixel]	REF. POINT DISTANCE D [m]
7,8	14,0463031	0,0028093	231	**0,6489392**	69	**0,1938390**	3179	**8,9306395**
12,6	22,6901819	0,0045380	153	**0,6943196**	45	**0,2042116**	2230	**10,1198211**
15,8	28,4527678	0,0056906	91	**0,5178404**	27	**0,1536449**	1370	**7,7960584**

Table 7-2: Estimated PV panel dimensions and distance from a reference point

According to the table, we noted that only for the second row (12,6 meter height) the relative error is acceptable (about 1% compared to the real distance measured). In fact, the dimensions calculated are close enough to the expected values, while the other results are significantly different from the real case.

These differences are partially due to two related factors

- ✓ the position of the target inside the image;
- ✓ the focal length of the camera.

Better performance can be achieved in the proximity of the centre of the image where the lens distortion is smaller with respect to the borders of the frame. To overcome the lack of accuracy in the results provided in Table 7-2: , another way to calculate the GSD is proposed.

7.1.1.3.2 GSD estimation using automatic panel's inclination recognition

This method takes only the required information from the images recorded by the RPAS and it is based on the automatic panel's inclination recognition.

To detect the potential inclination of the a panel, we calculate the ratio ρ of the height and the width (in pixel) of the panel, provided by the detected boundary box in the image.

Such value is compared to the default ratio of the panel (as explained in §6.1.1.3). For example, the default aspect ratio in a 160 cm x 100 cm PV panel is equal to:

$$\rho_s = \frac{160\ \text{cm}}{100\ \text{cm}} = 1{,}6$$

If the ratio ρ is less than the default ratio ρ_s and the absolute value of their difference is greater than a threshold value (which takes care of errors on boundary box detection), then the panel is mounted with an inclination angle on the transversal side. In this case, the length of the longitudinal side W can be used as reference in the calculation of the GSD:

$$\text{GSD} = \frac{\text{W[m]}}{\text{P}_\text{w}\text{[pixel]}}$$

In the opposite case, in which $\rho > \rho_s$ and $|\rho - \rho_s| > \nu$, the panel is inclined on the longitudinal side and we use the length of the transversal side H as reference:

$$\text{GSD} = \frac{\text{H[m]}}{\text{P}_\text{h}\text{[pixel]}}$$

The results obtained using this new approach for GSD calculation are illustrated in Table 7-3.

RPAS HEIGHT [m]	GSD RESOLUTION [m/pixel]	PANEL WIDTH (Pw) [pixel]	PANEL WIDTH (Pw) [m]	PANEL HEIGHT (Ph) [pixel]	PANEL HEIGHT (Ph) [m]	REF. POINT DISTANCE D [pixel]	REF. POINT DISTANCE D [m]
7,8	**0,0029437**	231	**0,6800000**	69	**0,2031169**	3179	**9,3580952**
12,6	**0,0044444**	153	**0,6800000**	45	**0,2000000**	2230	**9,9111111**
15,8	**0,0074725**	91	**0,6800000**	27	**0,2017582**	1370	**10,2373626**

Table 7-3: Estimated PV dimensions with new GSD calculation

7.1.1.4 PV Panel inclination and height

Several tests were conducted on height and PV panels inclination to verify if the data acquired from the drone at two different target heights, respected the form factor of the panels, providing a true indication about PV Panels inclination and GSD.

The final test was performed in "Lo Uttaro" PV in June 19th, 2017 in San Nicola la Strada (CE), after different configurations and tunings to the on-board software. The test was limited to a small portion of the Plant with panels placed over the canopy showed in *Figure 7-3* with a given inclination of 10° degrees.

Figure 7-3 : inclination of the Canopy where panels are placed

The camera used for this test is a FLIR Vue Pro camera (resolution: 336 × 256, FOV: 9 mm FOV 35 ° × 27°) installed on drone and pointing downwards to nadiral direction.
The following results refer to two acquisitions, the first done at 10 meters and the second at 15 meters above the PV Panels. In accordance with formula provided in §7.1.1.4, the inclination of the Panel (tilt angle) is:

$$\text{Tilt angle}\begin{cases} t = \arccos\left(\dfrac{\rho}{\rho_s}\right), & \rho < 1{,}6 \\ t = 0\,, & \rho = \rho_s = 1{,}6 \\ t = \arccos\left(\dfrac{\rho_s}{\rho}\right), & \rho > 1{,}6 \end{cases}$$

Such formula was applied by averaging all ρ_s related to each panel measurement of width and height expressed in pixel. In particular in *Figure 7-4* the panels recognized at different heights are showed.

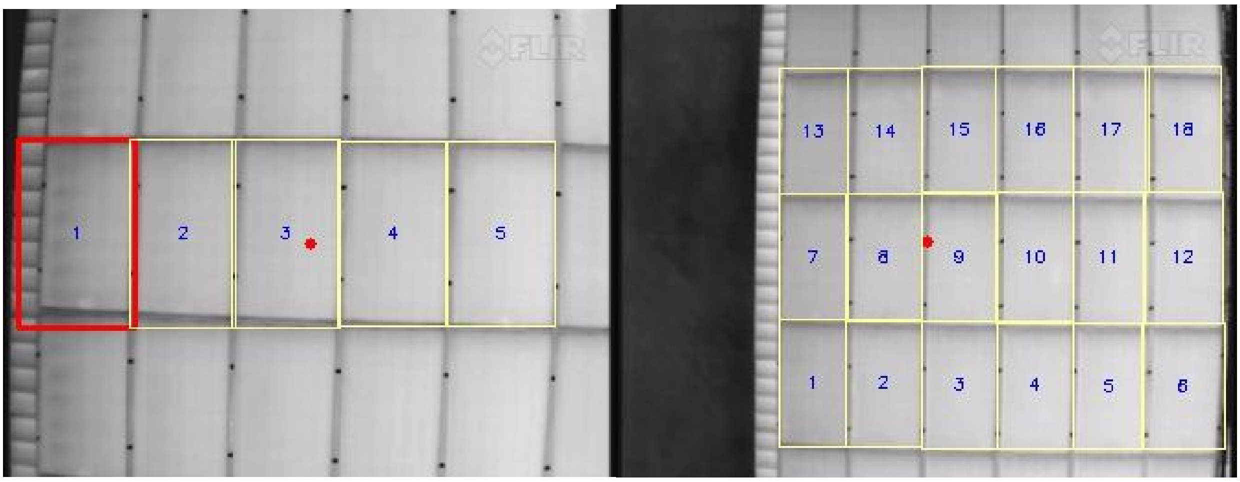

Figure 7-4 : Thermal images at 10 meters (left) and 15 meters (right) above the panels

During this test the Drone hovers exactly above the panels without moving horizontally. For each thermal photogram a certain numbers of panels are recognized and for each panel ρ_s is calculated and averaged by the number of Panels recognized in each photogram.
The Panels recognized are surrounded by the relative bounding boxes. In Table 7-4, 30 thermal photograms were considered for the test with the related ρ_s averaged for all the panels recognized in the photogram.

ρ_s (mean value of all boundary boxes detected)	height of drone above the panels [m]	ρ_s (mean value of all boundary boxes detected)	height of drone above the panels [m]
1,60461	10	1,668	15
1,64073	10	1,62795	15
1,62656	10	1,62891	15
1,62733	10	1,59449	15
1,60066	10	1,6188	15
1,58748	10	1,63827	15
1,66667	10	1,62467	15
1,63123	10	1,68371	15
1,62449	10	1,70937	15
1,61837	10	1,6303	15
1,60317	10	1,69154	15

ρ_s (mean value of all boundary boxes detected)	height of drone above the panels [m]	ρ_s (mean value of all boundary boxes detected)	height of drone above the panels [m]
1,64401	10	1,6855	15
1,59725	10	1,58635	15
1,63855	10	1,662	15
1,58786	10	1,61047	15
1,6092	10	1,6124	15
1,62893	10	1,66148	15
1,64765	10	1,66272	15
1,64154	10	1,68137	15
1,57113	10	1,67755	15
1,64065	10	1,65684	15
1,62459	10	1,55056	15
1,60359	10	1,72683	15
1,60543	10	1,67308	15
1,58632	10	1,67788	15
1,64522	10	1,72683	15
1,6743	10	1,61765	15
1,63445	10	1,68789	15
1,66463	10	1,74026	15
1,64012	10	1,68961	15

Table 7-4: Thermal photograms and mean value of ρ_s

This data show a mean value for ρ_s which is higher than the natural aspect ratio, comparing to panels placed levelled on the ground. In fact the panels are tilted on the longitudinal side (160 cm) as showed in *Figure 7-3*, causing a higher aspect ratio.

The tilt angle obtained is quite accurate at 10 meters from panels, but less accurate at 15 meters.

ρ_s (mean value of all boundary box detected)	t [°]	height above panels level [m]
1,623890	9,84	10
1,656776	15,04	15

Table 7-5: Panels inclination indirect measurement results

The aspect ratio introduced based on the well-known dimensions of PV panels, make in theory operations independent from the drone height; however, the less accurate result obtained at 15 meters be easily explained by the low resolution of the camera used (336x256 pixels) which introduce more quantization noise at 15 meters with respect to the dimensions of the panels, represented by less pixels considering the related bounding box.

Distance from Panels is always a trade-off between speed of operations versus accuracy of panel identification. Flying at a higher altitude provides less accurate results in terms of panels correct identification with the related anomalies, which might be always be improved by using more expensive equipment (e.g. 640x512 pixels resolution thermal camera). Moreover, flying at a greater altitude amplifies gimbal accuracy errors.

The results achieved at 15 meters are less accurate and the reason is due basically to the lower number of pixels representing the bounding box of the panel, which introduce a higher error on the determination of dimensions and inclination.

In conclusion this test suggested important indications about the optimal vertical distance that the drone shall maintain to the panels during inspections:

- ✓ 7-10 meters with 9 mm optics and 336x256 thermal camera equipment is a suggested configuration
- ✓ low cost thermal camera equipment (FLIR 336x256 pixel) can be also used for EASY-PV operations up to 10 meters of vertical distance from panels.

This test results were helpful to write the section of the RPAS user manual regarding on-site operations instructions.

7.2 NADIRAL ACQUISITION IMPLEMENTATION: GIMBAL ACCURACY

7.2.1 TEST_GIM.0010 → EVALUATION OF GIMBAL ACCURACY AND ANTENNA PHASE CENTER VS CAMERA CENTER OFFSET

7.2.1.1 Objectives

The aim of this test is to provide an assessment of the gimbal pointing error on nadiral acquisition during inspections taking into account also the fixed offset from the GNSS Rover antenna center of phase and the camera center.

7.2.1.2 Implementation

The evaluation of gimbal pointing error has been assessed in a second session of testing using a fixed structure due to difficulties encountered during the first session for keeping the drone stable in the air with centimetric precision control. The steel and wood structure helped the team to ensure the position of the thermal camera to be exactly perpendicular to the target on the ground.

Figure 7-5 Target and gimbal calibration test

The target was placed on the ground and the camera was perfectly aligned to the target by means of the thermal video stream video feedback, after placing the RPA on the structure (height of camera from the ground=2,80 meters).

Two sessions of 20 minutes testing were executed without restarting the system to evaluate possible misalignments over time. The RPA was placed on the structure and aligned on the Target as showed in Figure 7-14.

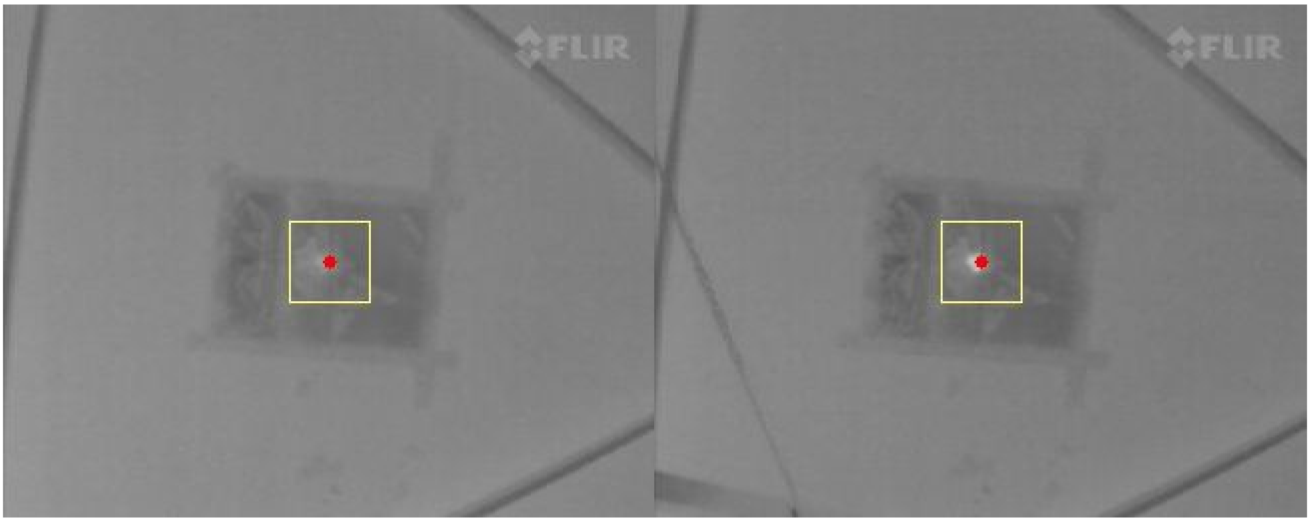

Figure 7-6 Gimbal maximum misalignment over time

7.2.1.3 Results

The maximum registered misalignment over time has been assessed with the difference of alignment from the first and the last image acquired. In the first image a perfect alignment on the center of target is achieved. After 20 minutes a negligible misalignment of less than 1 pixel from the target has been registered.

In fact at the given height from the specification of gimbal the pointing error is less than 3 mm on the horizontal plane and this is confirmed by comparing the two pictures where the maximum observed misalignment is less than 1 pixel. At the target flight height of 8 meters the impact of horizontal error due to gimbal misalignment is therefore still acceptable.

According to specification of gimbal and the preliminary assessment, the registered misalignment is negligible and contributes for less than 2 cm on the horizontal plane in the overall error budget.

7.3 TEST_SEN.0010 SENSOR LENS DISTORTION

The scope of this test is to evaluate the expected impact of lens distortion for thermal camera sensor.

7.3.1 *General approach*

After studying the state of the art for this kind of tests, we decided to use a practical approach without particular additional equipment, by building appropriate and simple tools able to give us an idea of the error magnitude introduced by the camera, to understand its contribution to the error budget.

7.3.2 *The environment*

The first FLIR thermal camera, equipped with 13 mm lens is used not only to reveal the thermal anomalies of the overflown photovoltaic panels, but also to aid the computer vision algorithm, running on the OBC, for the identification of the bounding box surrounding the PV panels. Especially in the border the lens distortion may introduce relevant errors impacting the estimation of GNSS coordinate of the bounding box surrounding the PV Panels.

The test consisted in creating, inside TopView laboratories, a static system able to calculate the distortion introduced by the camera on the peripheral pixels of the frame and to extend the result of it to the altitudes flown by the drones in the real environment.

7.3.3 *Test setup*

Usually the calibration of a camera lens is performed by using a chessboard pattern on a sheet of paper and capturing images of this pattern with the camera from several different angles. However, this is difficult to accomplish with a thermal camera, as the chessboard pattern will not show up clearly on the paper because the temperature of the paper is close to uniform.

To make the calibration process more in line with that of calibrating a regular camera, a 2 mm plastic plate with a matrix of 8x7 holes was made. The holes are exactly 3 mm wide and 20 mm apart from each other (center to center).

The custom plate has been realized by a 3d Printer (Ultimaker 2) as showed in Figure 7-7.

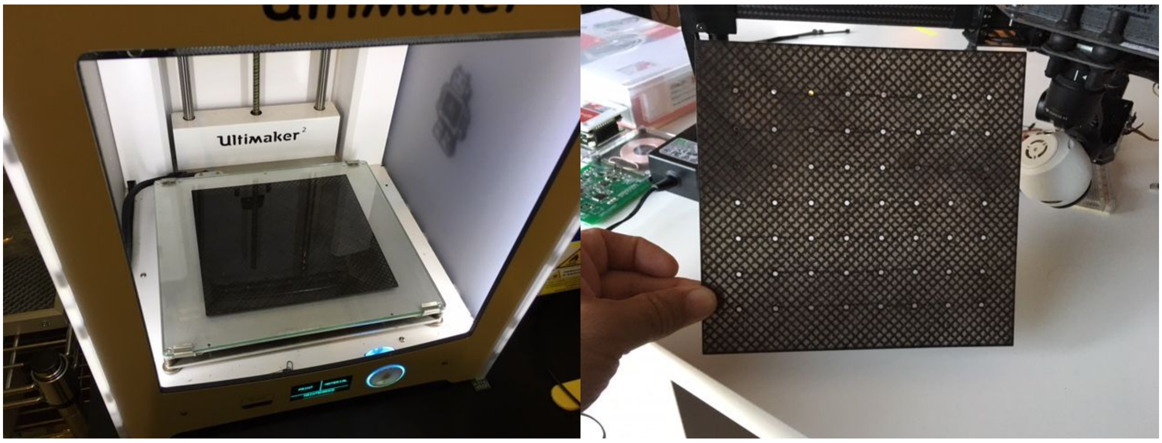

Figure 7-7 plastic plate with holes realized by 3D printer

The principle at the basis of the test is to capture the influence of a cold source positioned on the rear of the plate, maintained at environment temperature: through the calibrated holes, the cold temperature is detected by the thermal camera and a strong contrast is created to make the holes well defined and visible by the sensor.

The tool realized to produce a temporary cold temperature (for the time needed to take several snapshots) has been realized by a simple aluminium rectangular case filled with water, put in a refrigerator to reach ice temperature. Once the water has been transformed in ice, the case was used as the required temporary cold temperature generator. Figure 7-8 shows the realized tool.

Figure 7-8 Plastic plate cooled down

The last tool needed was a support for the camera, maintained at the height for which the frame is completely occupied by the holed plate: a tripod has been used with a custom support for the camera realized by the 3d printer. The thermal camera was positioned at the height from the target of 42 cm. Figure 7-9 shows the assembly.

Figure 7-9 Camera support

7.3.4 *Test Operation*

Several images of the plate from different angles and positions were taken at room temperature of 24°C. An example image is shown in Figure 7-10. The thermal camera was configured to be sensitive to the temperature range between 0 and 15°C effectively, creating an almost binary like image, hence making the plate pattern easily detectable.

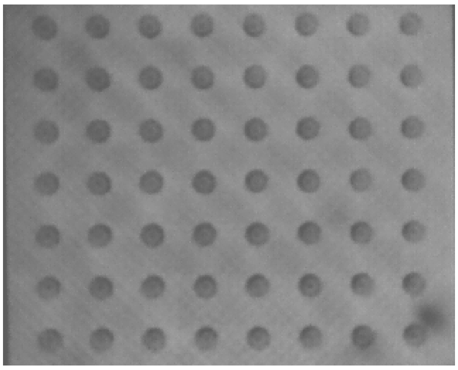

Figure 7-10 Thermal image of the holed plastic plate (177 mm x135 mm)

The analogic images have been converted, by Gimp software tool, into monochromatic frames with a small grey grade, as showed in Figure 7-11.

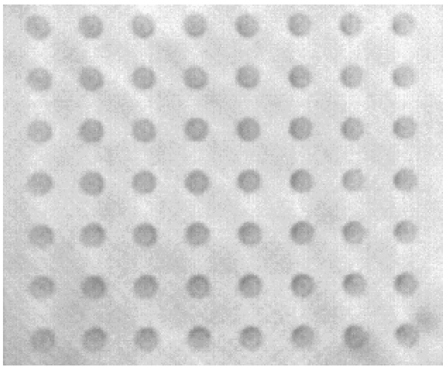

Figure 7-11 Thermal image of the holed plastic (grey scale image)

A successive elaboration was made with a cad software, superimposing to the thermal frames obtained, the geometric pattern reproduced into the original built plate, as showed in Figure 7-12.

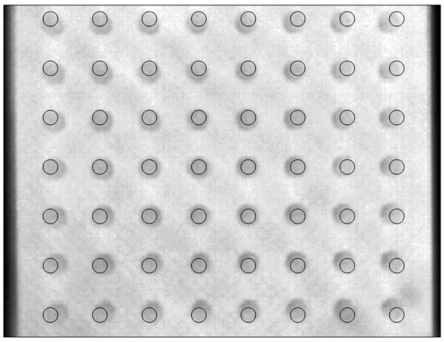

Figure 7-12 holes geometric pattern

The correct circle pattern has been compared with the scanned holes, resulting in a 3 mm. diameter circle included into the photographed cold hole, generally revealed as a larger circle (4,4 mm. diameter), due to the radiance caused by the temperature diffusion around the borders.

Finally the red circles were drawn manually around the corners and center holes. The precise distance was measured with the aid of the cad software tool between two contiguous red and black circles.

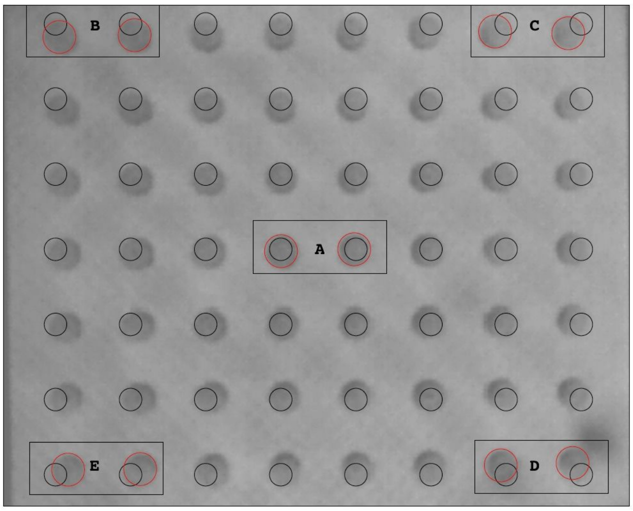

Figure 7-13 Thermal image Distortion and measure of it

7.3.5 *Results*

The results of the test are reported in Table 7-6, which shows the distortion of the image by detecting the alignment errors of the corner holes compared with those in the central holes.

		Left Hole	Right Hole
A	Center Holes	0,2431	0,2242
B	Top-Left Corner	1,8294	1,5916
C	Top-Right Corner	1,7826	2,1309
D	Bottom-Right Corner	1,4428	1,9458
E	Bottom-Left Corner	1,8191	1,4788

Table 7-6: measured distortion of the image holes (expressed in mm)

Table 7-6 reports, for the worst case (corner C), the following measured parameters and their comparison with the frame dimensions (all units in millimeters):

- ✓ Distance: the module of the vector between the centers of two contiguous circles;
- ✓ X projection: the component of x axis of the frame;

- ✓ Y projection: the component of y axis of the frame;
- ✓ X width: the width of the frame;
- ✓ Y width: the height of the frame;
- ✓ X Pixels: the number of pixels on the row;
- ✓ Y Pixels: the number of pixels on the column;
- ✓ Pixel inter-axis: distance between two (row or column) pixels.

	Module	X	Y
(C) Top-Right Corner (mm)	2,1309	1,7242	1,2522
(A) Center Holes (mm)	0,2242	0,1304	0,0231
Halo Compensation (mm)	1,9067	1,5938	1,2205
Frame length (mm.)		177	135
Frame (Pixel)		336	256
Pixel inter-axis (mm)		0,53	0,53

Max distortion vs. frame length (%)	0,90%	0,91%
Max distortion (# pixels mismatch)	3/336	2/256

Table 7-7: measured distortion of the image holes

Considering the halo effect which enlarges the reproduced holes in the picture (about 4,4 mm vs 3,0 mm), we can consider that the central holes, although affected by a small error, can be taken as reference to calculate the max distortion on the borders, in terms of error percentage compared to the frame dimension (height and width).

7.3.6 *Test reported in real scenario*

Taking into account the figures obtained during lab test, the real effect of the calculated distortion can be assessed during operations by considering the operative altitudes of the flight.
Considering that the FOV of the tested lens (13 mm.) is 45° (Width) x 37° (Height), the applicable rule that links the altitude to the ground swath area is:

- Ground-Width = [Altitude x tg (45°/2)] / 2
- Ground-Height = [Altitude x tg (37°/2)] / 2

The lab test has been made at a distance of 42 cm between the lens and the target, with an effective swath area of 177 x 135 mm. The plastic plate area has been also used successfully as cross check of the FOV specification of the camera.
The distortion measured at a distance of 42 cm is applied with acceptable approximation linearly with the operational altitude of flight. The rate of distortion resulting from laboratory test (Max distortion vs. frame length) is rougly 0,09% with respect of the total length of the frame. At different altitudes the error is evaluated approximately by the following table:

Ground-Width [m]	Ground-Heigth [m]	Altitude [m]	Ground-Width distrotion [m]	Ground-Heigth distortion [m]
0,087	0,0702	0,42	0,0016	0,0013
0,2071	0,1672	1,00	0,0037	0,003
0,4143	0,3344	2,00	0,0075	0,006
1,0357	0,836	5,00	0,0186	0,015
1,45	1,1704	7,00	0,0261	0,0211
2,0714	1,6721	10,00	0,0373	0,0301
3,107	2,5081	15	0,0559	0,0451
4,1427	3,3441	20	0,0746	0,0602
5,1784	4,1802	25	0,0932	0,0752
6,2141	5,0162	30	0,1119	0,0903

Table 7-8: distortion at different operational altitudes (vertical distance to PV Panels)

The operational altitudes suggested for PV panel inspections are 7-10 meters vertically from the Panels. At such distance the error of pixel mismatch generated by lens distortion is of few centimeters (with a 13 mm camera at 10 meters above the panels) therefore is still acceptable. However higher vertical distance or different lens which may introduce more distortion effect, requires video output calibration (configurable with the software developed) or the exclusion of the borders from algorithm calculations for PV Panels falling in the border of the frame

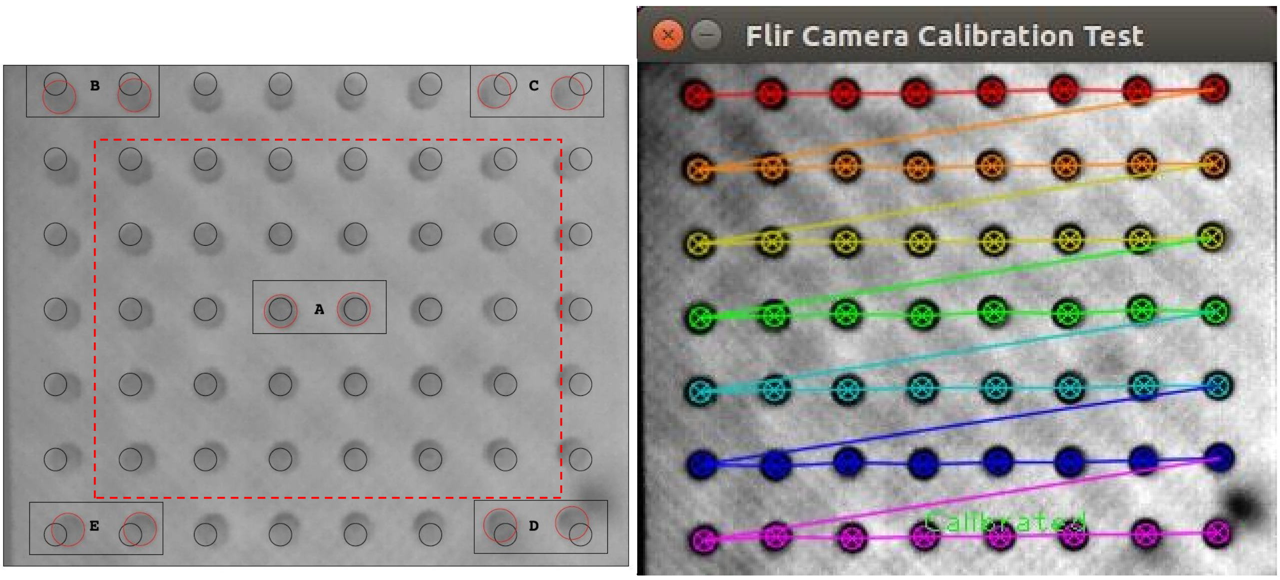

Table 7-9: Usable area with low distortion (left) - Full area usable after software calibration (right)

7.4 COMPUTER VISION IMPLEMENTATION

7.4.1 TEST_VIS.0010 CORE ALGORITHM PANEL DETECTION AND TRACKING WITHOUT GNSS SUPPORT

7.4.1.1 OBJECTIVES

The scope of this test is to verify the robustness and the tuning of the algorithm for Panels Tracking and anomaly discovery without GNSS support.

In this test, the first release of the tracking algorithm has been verified in order to collect data for further improvements in the next release of the software. The present release of the computer vision tracking algorithm is actually able to detect the PV panels shapes and assign them an identifier (not unique yet) based only on the image analysis; in fact, the GNSS accurate positioning information has not been used yet because not available at the time of test (pseudorange only).

7.4.1.2 ACTIVITY DESCRIPTION

In this test a dedicated architecture has been used on a real PV Plant to test the first release of the SW library developed.

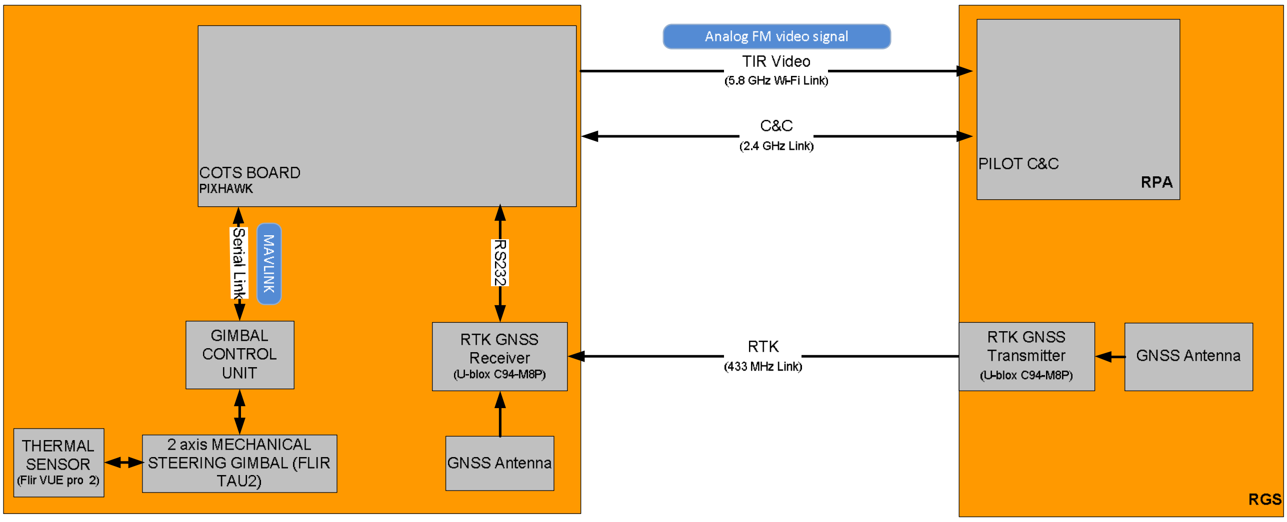

Figure 7-14: Used Testing Architecture

The testing architecture has been described in the figure above. The units insulated with the respective functional chains allowed to perform the following tests:

- ✓ Gimbal Accuracy pointing downwards
- ✓ Antenna Center of Phase offsets
- ✓ RTK Position with dynamic baseline
- ✓ Algorithm Accuracy aided by GNSS high accuracy positioning
- ✓ “Comparison” of GNSS high accuracy positioning by means of RTK (GPS+GLONASS) with GNSS positioning achieved by multiconstellation (GPS/GLONASS + Galileo) pseudorange receiver.

Figure 7-15: RPAS (Rover) and Base Station used for RTK Positioning functional Testing

The drone has been equipped with 3 different GNSS receivers

- ✓ 1 used for Navigation Purposes
- ✓ 1 used for RTK (Rover)
- ✓ 1 for Galileo pseudorange first assessment and comparison

The thermal Camera has been adapted with some modification on a COTS gimbal allowing the camera to point always downward even during RPAS maneuvers.

Figure 7-16: Gimbal and Thermal Camera pointing downwards.

Some expected EMC integration issues have been encountered; in fact the magnets inside COTS antenna provided with the U-Blox M8P development kit generated strong magnetic interference with the primary megnetometer (compass) used by RPAS for navigation purposes and also to keep a stable position for hovering (aided by GNSS). For this reason an experimental set up with a long vertical shaft to the GNSS antenna (used in the RTK Rover receiver) has been used to reduce magnetic interference to he primary RPAS compass. Another solution used consisted in keeping antenna shaft low (enhancing RPAS stability) and turining off some primary RPAS sensor such as magnetometer and GNNS receiver. For this reason the RPAS operations for the experimental set up have been handled by an experienced (CAA certified) RPAS pilot who managed the flight in full manual mode, without GNSS and navigation assistance.

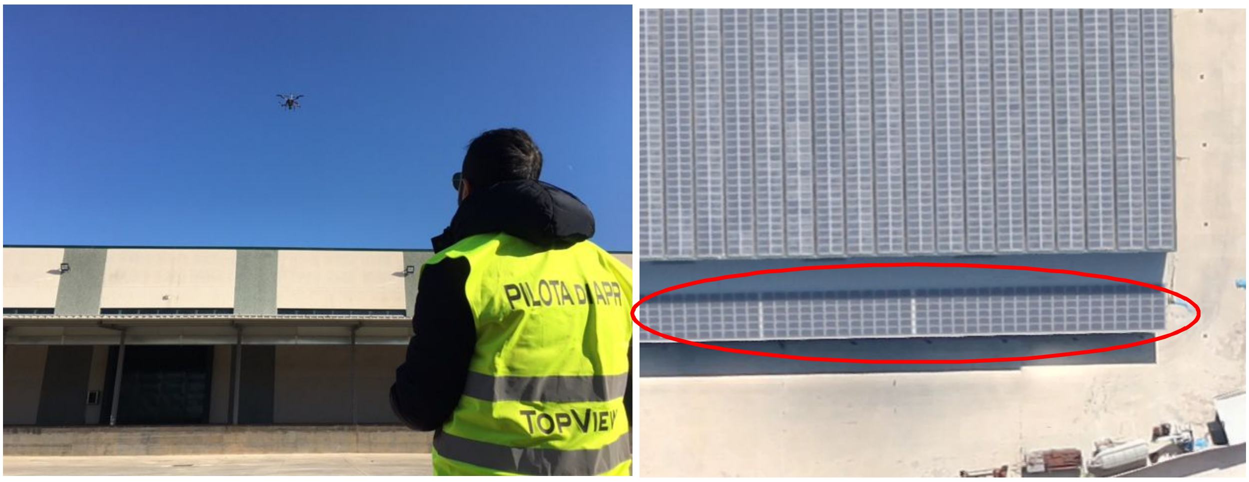

Figure 7-17: Flight Operations on a real PV plant.

The pilot has flown the RPAS over a row 6x72 PV panels, executing a lateral acquisition for the whole raw. The results were later evaluated in post processing.

7.4.1.3 FINAL RESULTS

This test provided very interesting feedbacks about detection and tracking capability of computer vision algorithm.

Each thermal image collected during the flight encapsulates, by means of the implemented architecture test-bed, the geographical position (latitude and longitude) and the height of the drone in the EXIF metadata. For each PV panel a yellow bounding box with the correspondent ID is overlapped on the thermal image as shown in *Figure 7-18*.

The dimensions of each panel are averaged and used to calculate the panel inclination index and to make an estimation the GSD (at the panel) as illustrated in *Figure 7-19*.

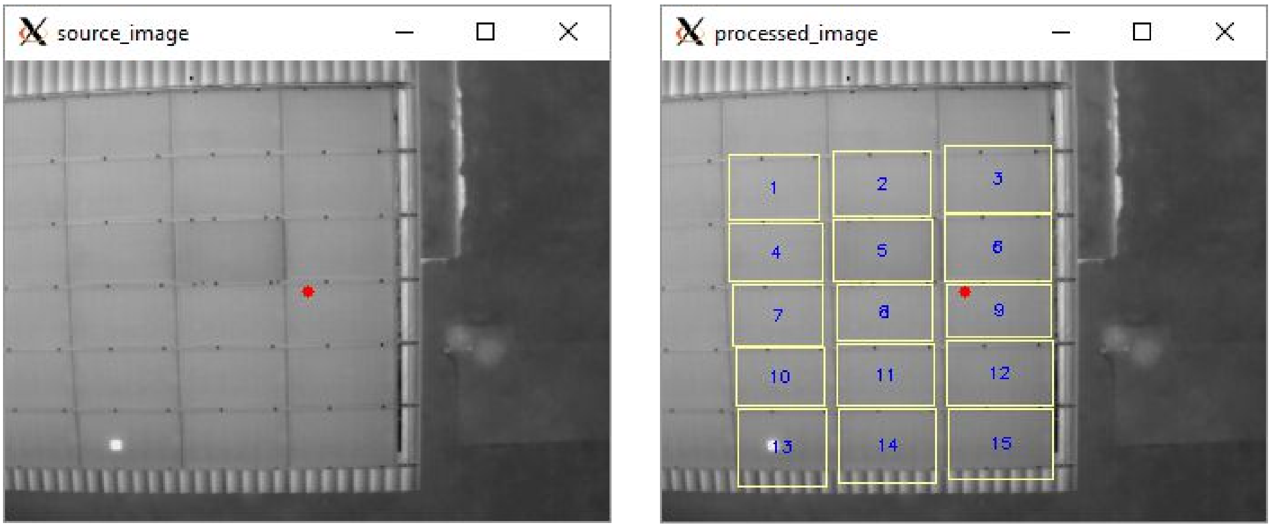

Figure 7-18: source frame (on the left) and processed image with PV Panels detected by the computer vision tracking algorithm (on the right); the red dot represents the center of the image.

```
Bounding box:  1 width: 50 height: 36
Bounding box:  2 width: 54 height: 36
Bounding box:  3 width: 59 height: 37
Bounding box:  4 width: 52 height: 32
Bounding box:  5 width: 55 height: 34
Bounding box:  6 width: 59 height: 37
Bounding box:  7 width: 50 height: 34
Bounding box:  8 width: 53 height: 31
Bounding box:  9 width: 58 height: 29
Bounding box: 10 width: 49 height: 32
Bounding box: 11 width: 54 height: 34
Bounding box: 12 width: 59 height: 36
Bounding box: 13 width: 49 height: 43
Bounding box: 14 width: 54 height: 41
Bounding box: 15 width: 58 height: 39
Width: 54.200000
Height: 35.400000
GSD: 0.029520
```

Figure 7-19: Output of the tracking algorithm: PV Panels detected inside the current frame with their respective dimensions, mean, dimension of panels in pixels (width and height), estimated GSD.

To transform the pixel position inside the frame to the associated geographical coordinates we need to know the distance (in meter) of the pixel from the image's centre and the azimuth angle. To overcome the lack of the compass reading, the required azimuth angle is calculated through the SW C++ interface for ExifTool using the geographical position of the current and the next frame. The software detects at the end, the coordinate of the mouse pointer and calculate the estimated geographical position as shown in Figure 7-20.

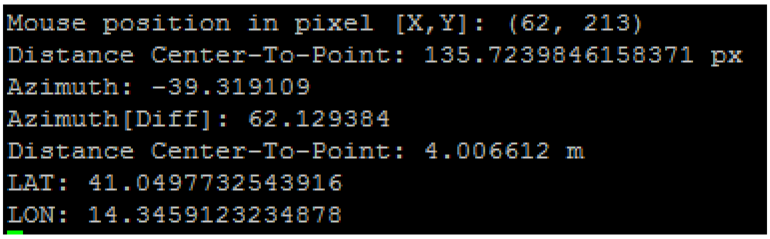

Figure 7-20: Geographical position estimation of the hotspot point visible in Figure 7-18.

At the current stage the algorithm can provide as output the PV Panel ID, the presence of a possible thermal anomaly and the position of the four vertexes of the detected bounding boxes as shown in Figure 7-21 and Table 7-10 for another section part of the same PV plant.

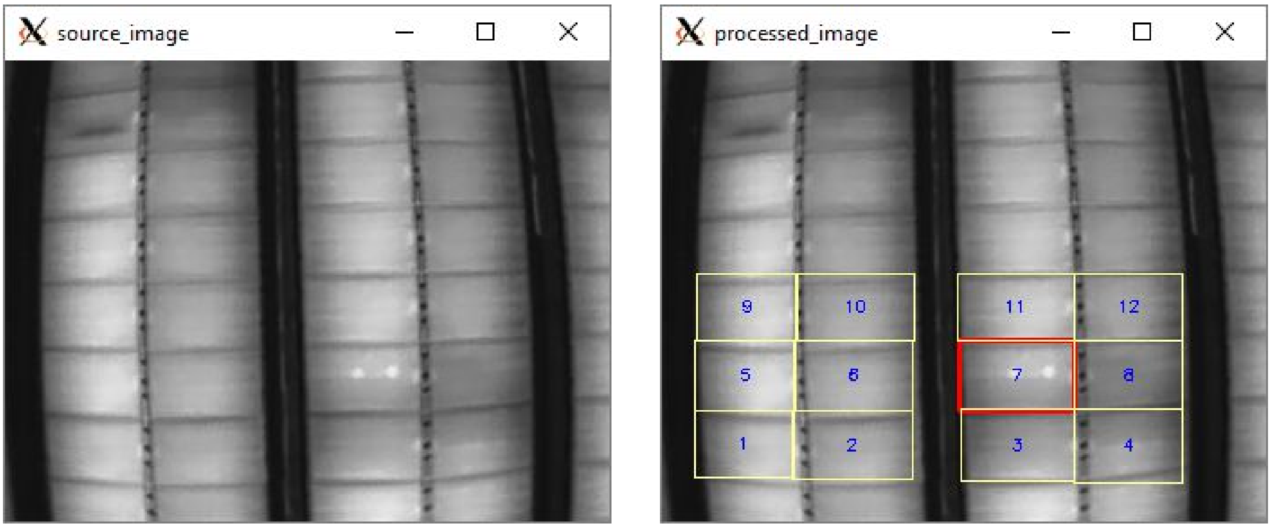

Figure 7-21:. Source frame (on the left) and processed frame by the Computer Vision tracking algorithm (on the right); detected PV panels are surrounded with a coloured bounding box: yellow for normal condition and red for the faulty panels with thermal anomaly.

Panel ID	10	Panel anomaly	0	Panel top-left	[74, 118]	Panel top-right	[140, 118]	Panel bottom-right	[140, 155]	Panel bottom-left	[74, 155]
Panel ID	1	Panel anomaly	0	Panel top-left	[18, 194]	Panel top-right	[73, 194]	Panel bottom-right	[73, 231]	Panel bottom-left	[18, 231]
Panel ID	7	Panel anomaly	1	Panel top-left	[165, 155]	Panel top-right	[229, 155]	Panel bottom-right	[229, 194]	Panel bottom-left	[165, 194]
Panel ID	11	Panel anomaly	0	Panel top-left	[164, 118]	Panel top-right	[229, 118]	Panel bottom-right	[229, 155]	Panel bottom-left	[164, 155]
Panel ID	9	Panel anomaly	0	Panel top-left	[19, 118]	Panel top-right	[75, 118]	Panel bottom-right	[75, 155]	Panel bottom-left	[19, 155]
Panel ID	4	Panel anomaly	0	Panel top-left	[229, 193]	Panel top-right	[289, 193]	Panel bottom-right	[289, 234]	Panel bottom-left	[229, 234]
Panel ID	6	Panel anomaly	0	Panel top-left	[73, 155]	Panel top-right	[139, 155]	Panel bottom-right	[139, 194]	Panel bottom-left	[73, 194]
Panel ID	8	Panel anomaly	0	Panel top-left	[229, 155]	Panel top-right	[289, 155]	Panel bottom-right	[289, 193]	Panel bottom-left	[229, 193]
Panel ID	3	Panel anomaly	0	Panel top-left	[166, 193]	Panel top-right	[229, 193]	Panel bottom-right	[229, 233]	Panel bottom-left	[166, 233]

Panel ID	5	Panel anomaly	0	Panel top-left	[18, 155]	Panel top-right	[74, 155]	Panel bottom-right	[74, 194]	Panel bottom-left	[18, 194]
Panel ID	2	Panel anomaly	0	Panel top-left	[72, 194]	Panel top-right	[139, 194]	Panel bottom-right	[139, 232]	Panel bottom-left	[72, 232]
Panel ID	12	Panel anomaly	0	Panel top-left	[229, 118]	Panel top-right	[289, 118]	Panel bottom-right	[289, 155]	Panel bottom-left	[229, 155]

Table 7-10 PV Panels detected by the algorithm for the image frame in Figure 7-21 with the associated information: panel ID, possible thermal anomaly, bounding box position.

Figure 7-22 shows the detected PV panels a few frames after those represented in Figure 7-21.

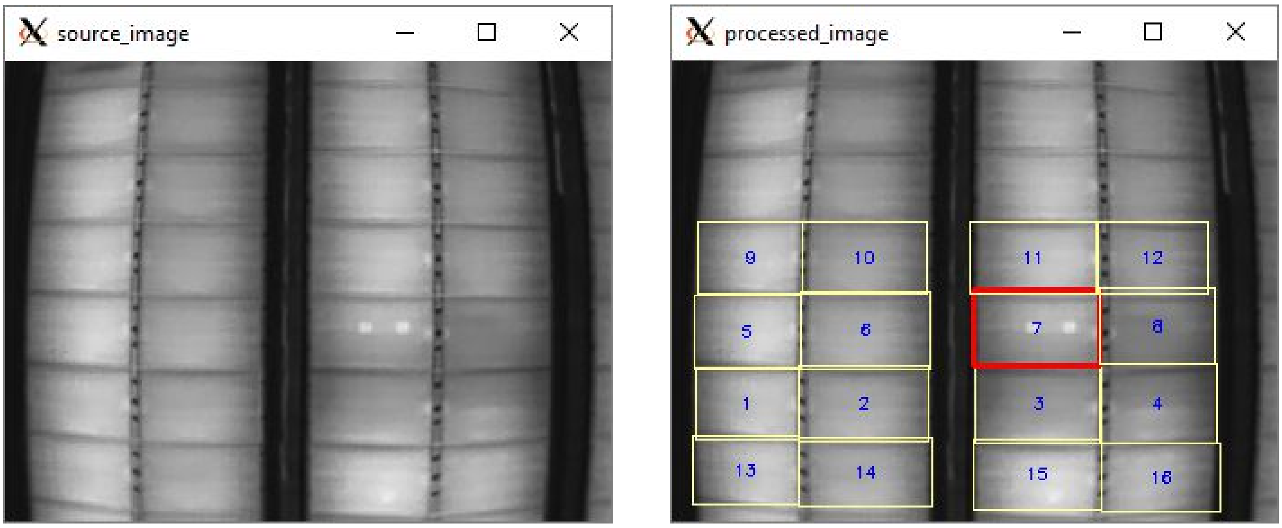

Figure 7-22: New Panels Detected (Local ID, not supported yet by GNSS information)

Panel ID	2	Panel anomaly	0	Panel top-left	[70, 169]	Panel top-right	[142, 169]	Panel bottom-right	[142, 211]	Panel bottom-left	[70, 211]
Panel ID	1	Panel anomaly	0	Panel top-left	[13, 170]	Panel top-right	[70, 170]	Panel bottom-right	[70, 210]	Panel bottom-left	[13, 210]
Panel ID	3	Panel anomaly	0	Panel top-left	[168, 168]	Panel top-right	[238, 168]	Panel bottom-right	[238, 212]	Panel bottom-left	[168, 212]
Panel ID	4	Panel anomaly	0	Panel top-left	[237, 168]	Panel top-right	[302, 168]	Panel bottom-right	[302, 212]	Panel bottom-left	[237, 212]
Panel ID	16	Panel anomaly	0	Panel top-left	[238, 212]	Panel top-right	[304, 212]	Panel bottom-right	[304, 250]	Panel bottom-left	[238, 250]
Panel ID	7	Panel anomaly	1	Panel top-left	[167, 127]	Panel top-right	[237, 127]	Panel bottom-right	[237, 169]	Panel bottom-left	[167, 169]
Panel ID	8	Panel anomaly	0	Panel top-left	[237, 126]	Panel top-right	[301, 126]	Panel bottom-right	[301, 168]	Panel bottom-left	[237, 168]
Panel ID	14	Panel anomaly	0	Panel top-left	[70, 209]	Panel top-right	[144, 209]	Panel bottom-right	[144, 247]	Panel bottom-left	[70, 247]
Panel ID	5	Panel anomaly	0	Panel top-left	[12, 130]	Panel top-right	[71, 130]	Panel bottom-right	[71, 171]	Panel bottom-left	[12, 171]
Panel ID	6	Panel anomaly	0	Panel top-left	[71, 128]	Panel top-right	[143, 128]	Panel bottom-right	[143, 171]	Panel bottom-left	[71, 171]
Panel ID	15	Panel anomaly	0	Panel top-left	[167, 210]	Panel top-right	[238, 210]	Panel bottom-right	[238, 249]	Panel bottom-left	[167, 249]
Panel ID	13	Panel anomaly	0	Panel top-left	[11, 208]	Panel top-right	[70, 208]	Panel bottom-right	[70, 246]	Panel bottom-left	[11, 246]

Panel ID	12	Panel anomaly	0	Panel top-left	[235, 89]	Panel top-right	[297, 89]	Panel bottom-right	[297, 129]	Panel bottom-left	[235, 129]
Panel ID	11	Panel anomaly	0	Panel top-left	[165, 89]	Panel top-right	[236, 89]	Panel bottom-right	[236, 129]	Panel bottom-left	[165, 129]
Panel ID	9	Panel anomaly	0	Panel top-left	[14, 89]	Panel top-right	[72, 89]	Panel bottom-right	[72, 129]	Panel bottom-left	[14, 129]
Panel ID	10	Panel anomaly	0	Panel top-left	[72, 89]	Panel top-right	[141, 89]	Panel bottom-right	[141, 129]	Panel bottom-left	[72, 129]

Table 7-11 PV Panels detected by the algorithm for the image frame 27 depicted in Figure 7-22 with the associated information: Panel ID, thermal anomaly, bounding box position..

It's possible to note how the tracking algorithm keeps the numeration for the already detected panels while it assigns different IDs to new panels.

7.4.1.4 Additional Test Results

In addition to the tests already performed, a small portion of a PV plant has been monitored exploiting the accurate positioning information provided by the GNSS rover receiver and the computer vision algorithm.

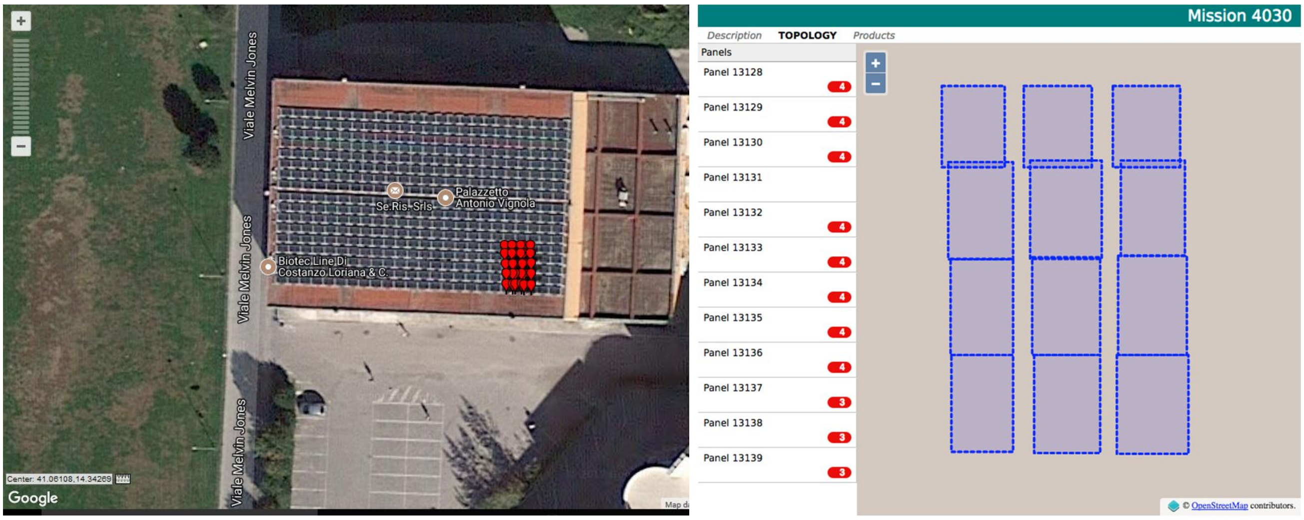

Table 7-12 PV Panels detected on PV plant and displayed on the Service center.

The test has been performed with the drone operating at the suggested horizontal speed for inspections (3-4 m/s) at vertical distance of 7 meters from panels. The thermography and picture acquired, processed by the algorithm, returned the panels corners showed on the User interface of the service centre.

7.5 GNSS SOLUTIONS

The RTK based positioning is supported by a number of receivers ranging from high-end dual frequency receives to low-cost L1-only receivers as described in Section 3. Though the high-end dual frequency is a desirable choice due fast initialization time, longer baselines, and relatively high accuracy then L1-only. However, keeping in view the low-cost constraint, L1-only RTK approach seems a potential solution as discussed in this section.

Test ID	Selected GNSS Test Receiver	GNSS Receiver Type		GNSS Constellation			RTK approach		Objective
		L1	L1/L2	GPS	GLONASS	Galileo	CORS	Private	
TEST_GNSS.0010	Navspark BD-RTK (*)	X		X				X	Performance assessment of single-frequency, single constellation: static positioning using private configuration
TEST_GNSS.0020	ublox M8P (**)	X		X	X	Waiting for FW update		X	Performance assessment of single-frequency, dual constellation: static positioning using private configuration
TEST_GNSS.0030	ublox M8P	X		X	X	Waiting for FW update	X		Performance assessment of EDAS service: static positioning using CORS network
TEST_GNSS.0040	ublox M8N	X		X	X	X		X	Preliminary test to evaluate new Galileo satellites (pseudorange measurement) in addition to GPS/GLONASS to have first outcomes after Galileo Initial Service declaration: static positioning
TEST_GNSS.0050	ublox M8P	X		X	X	Waiting for FW update		X	Performance assessment of single-frequency, dual constellation: dynamic positioning using private configuration
TEST_GNSS.0060	ublox M8P and North RTKite (***)	X		X	X	Waiting for FW update		X	Follow up of TEST_GNSS.0050, including comparison between single and dual frequency receivers.

Table 7-13: Performed Test activities

(*) http://navspark.mybigcommerce.com/s2525f8-bd-rtk-25mm-x-25mm-rtk-receiver-module/

(**) https://www.u-blox.com/en/product/neo-m8p

(***) http://northsurveying.com/index.php/instruments/gnss-rtk-receiver#datasheet

As reported in Table 7-13, We selected two low-cost L1-only RTK receivers, which are Navspark BD-RTK and ublox M8P, from the market survey we presented in Section 3. In particular, the single constellation Navspark BD-RTK was firstly selected for initial tests, but in a few months the market delivered the multi-constellation ublox M8P at a comparable cost. Finally, ublox M8P replaced Navspark in our test activities. As per datasheet, ublox M8P supports centimetre level positioning either using a CORS approach or local rover-base approach.

In the first phase of this study we performed static tests over a very short baseline in order to assess the positioning accuracy of the selected receivers. Based on the static positioning accuracy performance presented in this section, we preliminary confirmed the claimed performances and we prepared the configuration to perform more representative tests in a dynamic scenario.

Finally, in the last phase of the project, considering the solutions made available in the evolving market, a new RTK receiver has been selected for further tests as documented in TEST_GNSS.0060

7.5.1 TEST_GNSS.0010: PERFORMANCE ASSESSMENT OF RTK SINGLE FREQUENCY, SINGLE CONSTELLATION RECEIVER

7.5.1.1 Objectives

Objective of this test is to evaluate positioning accuracy performance of a single frequency single constellation RTK GNSS receiver. It is noted that precision is not in the scope of the test.

7.5.1.2 Activity Description

Positioning accuracy assessment of Navspark S2525-BD-RTK low-cost single-frequency (L1) receiver is presented in this section. It has to be remarked that Navspark supports both BeiDou and GPS, however, since not enough BeiDou satellites are visible in Europe, therefore GPS-only RTK positioning is enabled for use in the Europe.

For performance evaluation, one of the Navspark S2525-BD-RTK as a base and other as a rover with low-cost active patch antenna were set up over a very short baselines of few meters under clear-sky conditions. The positioning results are obtained with RTKNAVI application, which is a powerful open source tool for RTK missions analysis (see [RD 63]). The total test duration is approximately 11 hours.

This test has been performed in Sistematica's premises over Open Sky conditions

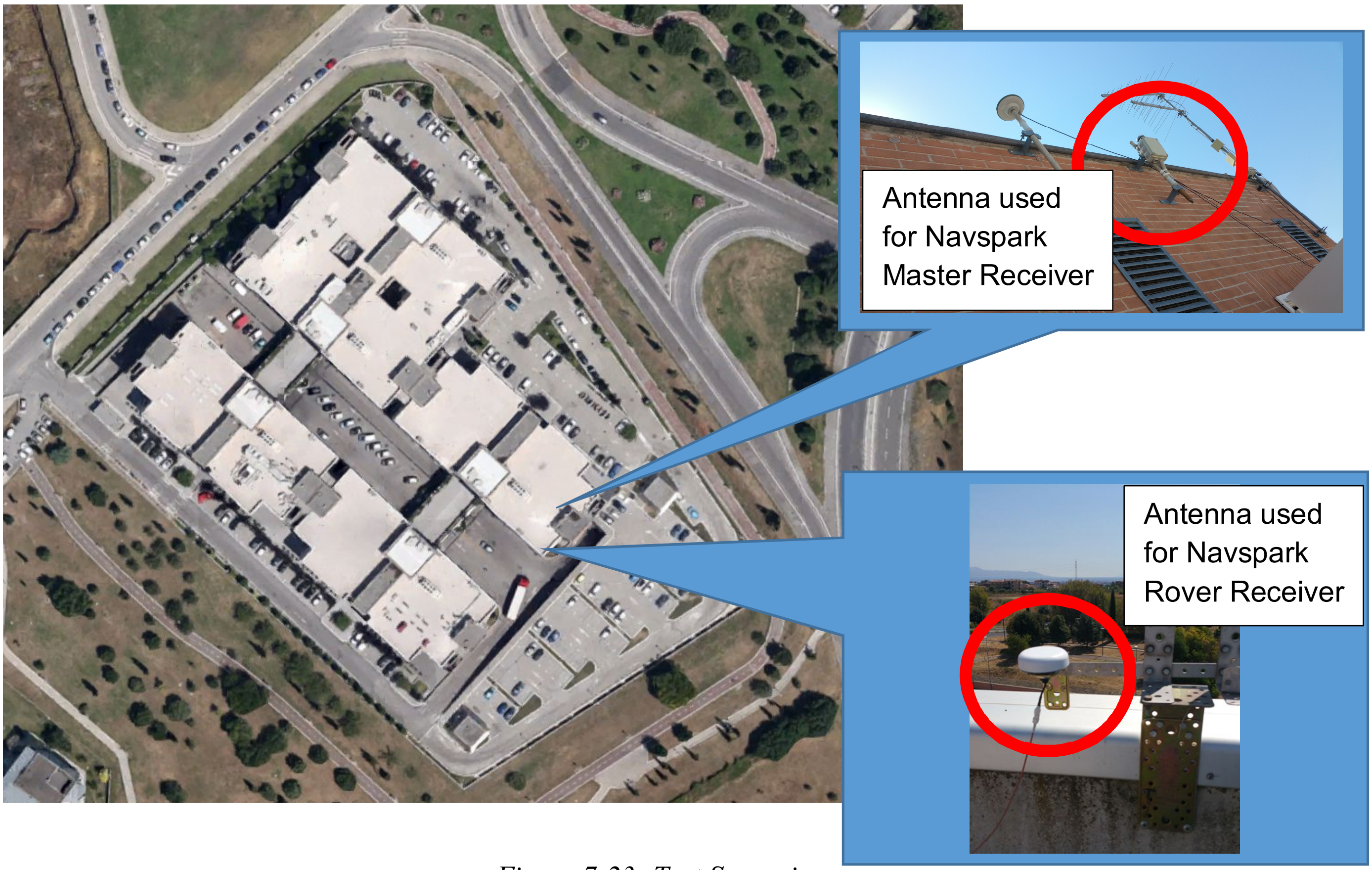

Figure 7-23: Test Scenario

7.5.1.3 Final Results

Figure 7-24 shows the RMS positioning accuracies of Navspark S2525-BD-RTK rover receiver.

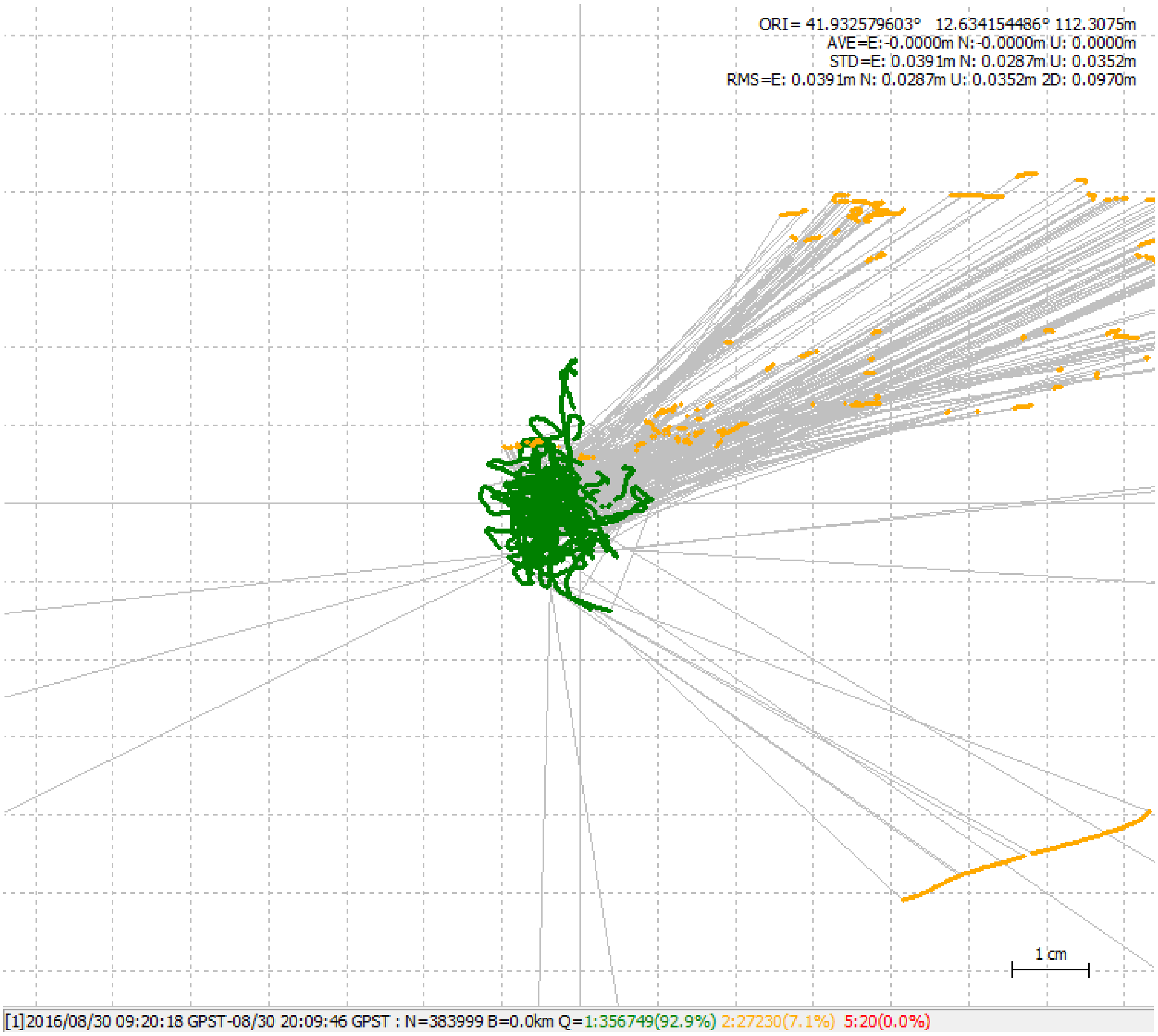

Figure 7-24: Positioning accuracy of Navspark rover receiver

The points in green colour indicate RTK Fix, yellow indicate RTK float, and red indicate single point position solutions. As shown in figure, Navspark single-frequency GPS-only achieves 2DRMS (denoted simply as 2D in top right corner of figure) positioning accuracy of 9.7 cm. Though the analysis is performed over a very short baseline, however, Navspark GNSS receiver seems a potential solution in meeting the EASY-PV accuracy requirements of 50 cm 2DRMS.

7.5.2 TEST_GNSS.0020: PERFORMANCE ASSESSMENT OF RTK SINGLE FREQUENCY, DUAL CONSTELLATION RECEIVER

7.5.2.1 Objectives

Objective of this test is to evaluate accuracy performances single-frequency dual-constellation GNSS RTK receiver. It is noted that precision is not in the scope of the test.

7.5.2.2 Activity Description

Positioning accuracy of ublox M8P RTK based GNSS receiver is evaluated by setting up base and rover receivers equipped with active patch antenna over a very short baseline of few meters. The evaluation was performed using RTKNAVI for a period starting from Aug 29 at 12:48 till 20:17 August 30, which makes a total of approximately 31 hours' evaluation time.

This test has been performed in Sistematica's premises over Open Sky conditions

Figure 7-25: Test Scenario

7.5.2.3 Final Results

Figure 7-26 shows positioning accuracy performance of ublox M8P rover receiver.

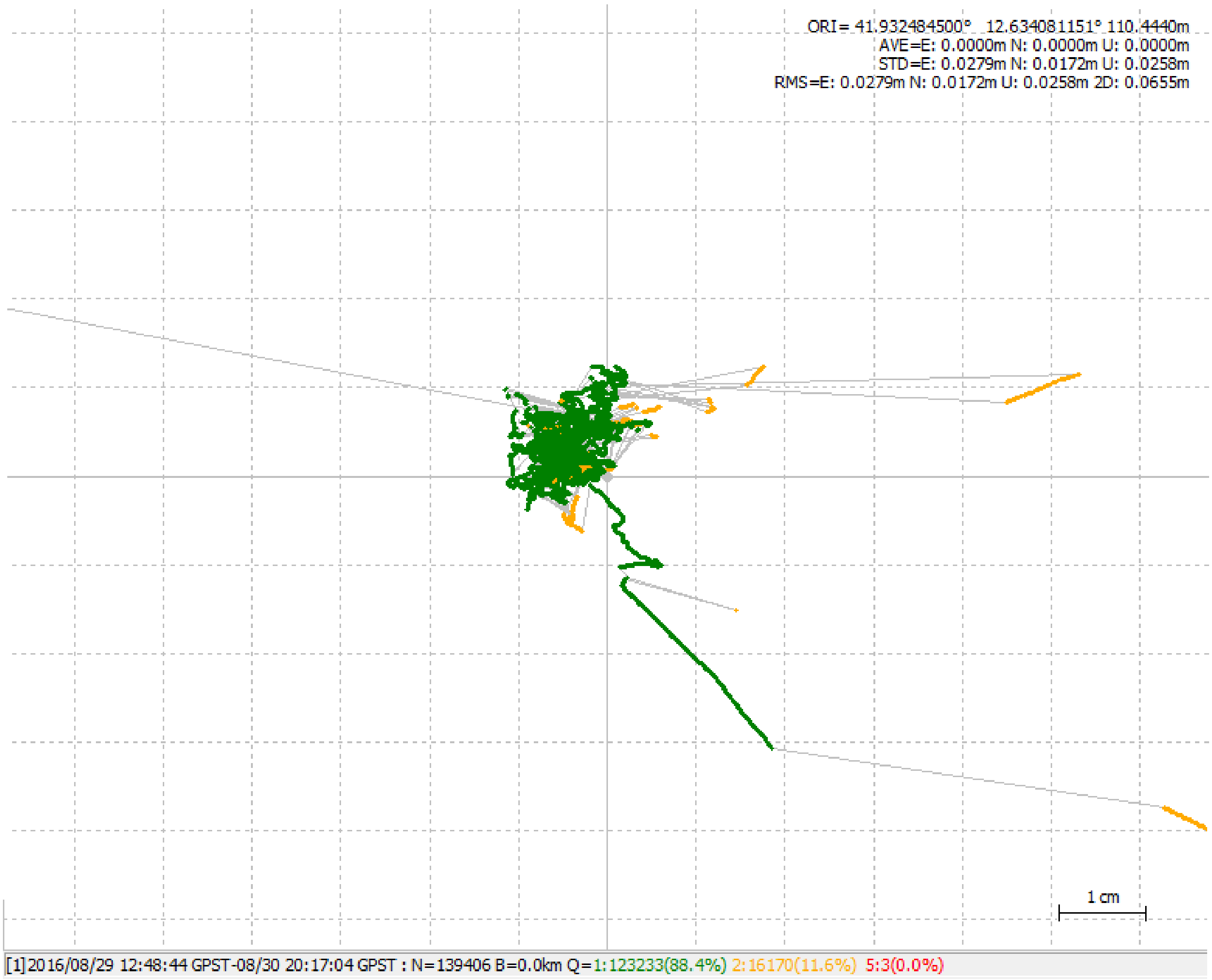

Figure 7-26: Positioning accuracy of ublox M8P rover receiver

It can be observed that ublox M8P rover receiver achieves 2DRMS positioning accuracy of 6.55 cm, which is relatively better than Navspark rover receiver mainly due to using dual-constellation configuration that allows more overhead satellites compared to single-constellation.

7.5.3 TEST_GNSS.0030: PERFORMANCE ASSESSMENT OF RTK SINGLE FREQUENCY, DUAL CONSTELLATION RECEIVER USING EDAS RIMS AS A BASE STATION

7.5.3.1 Objectives

The objective of this test is to evaluate the performance of ublox m8p receiver positioning accuracy considering a base-rover approach such that the base station in this case is a continuously operating reference station of EGNOS Ranging and Integrity Monitoring Station (RIMS). It is noted that precision is not in the scope of the test.

7.5.3.2 Activity Description

Ublox m8p (acts as a rover) is mounted on rooftop of Aalborg University building as shown in Figure 4-5. Using EDAS NTRIP interface, RTK messages in RTCM v3.1 (see Table 3-11) are provided to ublox m8p from Aalborg station (acts as a base) of EGNOS RIMS network. The effective baseline length between rover and base is 10.9 Km. The rover positioning data and statistics are collected for a period of 24 hours at a rate of 1 Hz.

Figure 7-27: ublox m8p acts as a rover mounted on the rooftop of Aalborg University building.

7.5.3.3 Final Results

The positioning statistics in Figure 4-6 show that ublox m8p achieves 2DRMS positioning accuracy of 10.8 cm such that 98.1% of the positioning fixes were RTK Float whereas 1.9% position solutions were RTK Fixed. Though, the static positioning accuracy and fix quality degraded due to larger baseline length of 10.9 km, however, the positioning accuracy is still acceptable as it is well below the overall positioning accuracy requirements of 50 cm. The use of CORS as a base station is a handy approach as it eliminates the need of setting up a local base station; nevertheless, the positioning accuracy might be traded-off for local base station set up taking in to account the accuracy requirements.

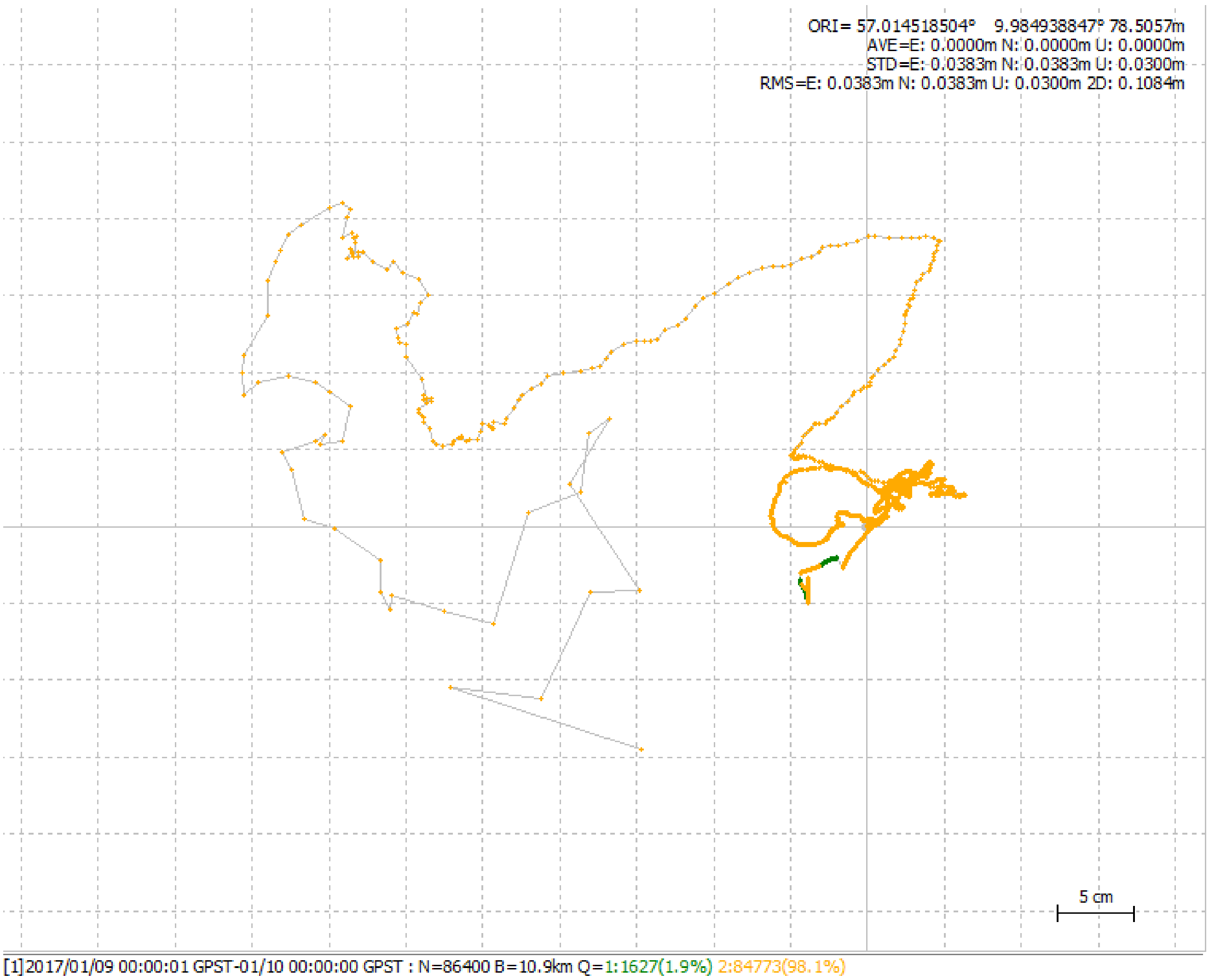

Figure 7-28: ublox m8p rover positioning accuracy. The base station used for RTK messages is Aalborg station (ALBB) of EGNOS RIMS network, which is spatially separated from rover by 10.9 km

7.5.4 TEST_GNSS.0040: GALILEO INITIAL SERVICES CHECK (PSEUDORAGE)

7.5.4.1 Objectives

This test has been conceived in order to check the availability of the Galileo SIS, according to the declaration of initial service) with the most popular low cost receiver (U-blox M8N) available at this time on the market for professional use.

7.5.4.2 Activity Description

This test has been performed using a development board designed in TopView labs to evaluate the U-Blox M8N chipset receiver.

In fact, the development boards used for other tests (U-Blox M8P) do not support GALILEO yet with the available Firmware FW3.01, therefore the team has made the choice to test also some popular low cost multi-constellation pseudorange receiver available on the market. Unfortunately, the first 2 receivers procured online did not allow to upgrade the firmware to FW3.01 required to the receiver to enable Galileo SIS acquisition. Indeed, the Ublox itself declares a lot of "fake U-Blox receivers" not upgradable to the latest firmware supporting Galileo as stated in the U-Blox forum:

https://forum.u-blox.com/index.php?qa=2365&qa_1=does-this-look-like-a-genuine-ublox-device

The team has therefore made the choice to design in-house a HW breadboard, procuring the main Receiver chip directly from the U-Blox to be sure to have a genuine product.

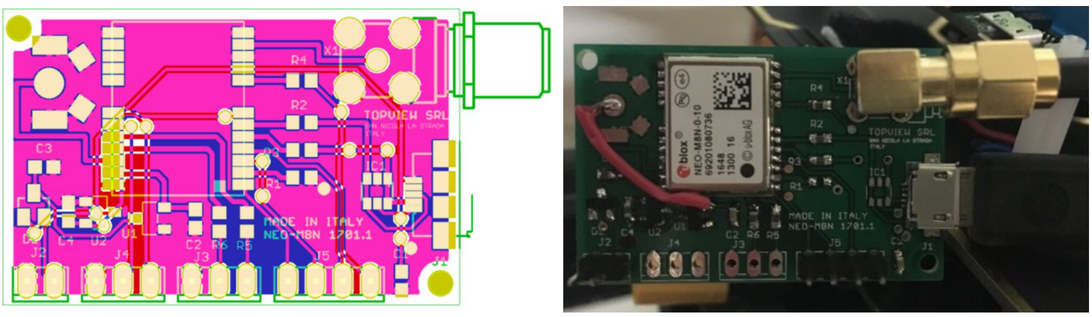

Figure 7-29: – HW Design vs first breadboard prototype of Ublox M8N Galileo enabled Receiver

This experience has been very useful for the team because it allowed a deeper understanding of the UBlox chipset configuration and the low level HW signals to drive a more efficient integration.

7.5.4.3 Final Results

During the test up to 6 satellites have been tracked by the UBlox M8N receiver, however just 1 SV resulted "Healty" and has been used for position calculation together with some GPS satellites in visibility.

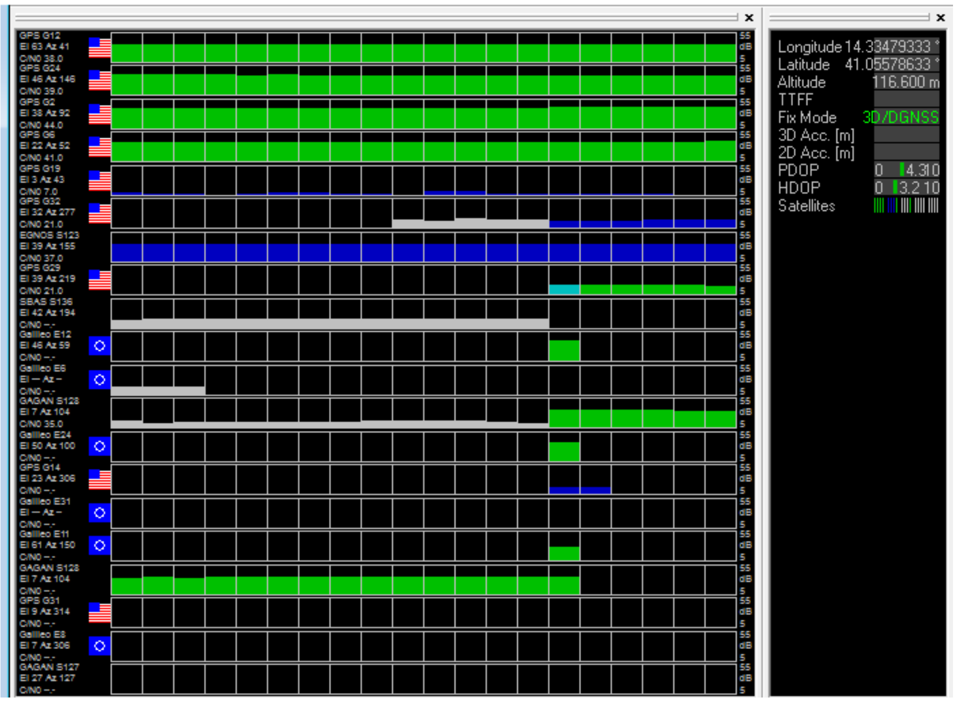

Figure 7-30: Galileo Satellites in field of view during acquisition test

This test is deemed as very preliminary as the acquisition time is very limited and performed only during a part of the day (in the morning). Moreover, along with the operational phase of the project (estimated to start in Q2 2018) the configuration of state of the art receivers will be always analysed taking into account further Galileo satellites development. This is expected to improve the GNSS performances in terms of accuracy having the possibility to use more satellites in field of view.

7.5.5 TEST_GNSS.0050: RTK DYNAMIC SCENARIO

7.5.5.1 Objectives

This Test aims at verifying both availability and positioning accuracy with RTK technique considering a dynamic baseline in a suitable scenario, comparable to the one of operations. The baseline considered for the test spreads from 10 to 500 meters with Master Station and Rover always in radio link visual line of sight.

7.5.5.2 Activity Description

This is the first non-static test performed and has provided important information to the team for the achievement of the final solution. Indeed, the most of the effort has been spent by the team in the set-up and integration of the test-bed, with intense activities of hardware and software integration and GNSS receiver optimal configurations findings and tuning.

The scenario represented in the test considers normal conditions:

- ✓ the typical configuration used during inspections (e.g. 40-50 meter distance from RPAS to RGS including Master Station)
- ✓ The typical RPAS velocity with respect to ground during inspections (e.g. GS up to 2-3 m/sec)

and also “stress conditions”:

- ✓ RPAS up to 500 meters from RGS/Master station;
- ✓ RPAS velocity up to 6-7 m/sec (GS);

The testing architecture used for this test include the RPAS equipped with GNSS Multi-constellation u-blox M8P receiver (rover) and the RGS equipped with a tripod with GNSS antenna and U-blox M8P receiver (Master) installed.

This test is performed without a real RPAS flight in order to separate horizontal GNSS from other source of errors such as gimbal vertical pointing (TEST ID: TEST_GIM.0010).

The file used for the Configuration of GNSS receivers (Rover and Master) and the results obtained (raw data) are stored and kept under configuration control.

File Name	Version and date
GNSS_Configuration_BaseStation_9600_workingv1.0.txt	V1.0 27/01/2016
GNSS_Configuration_Rover_v1.1_UBX+NMEA_9600_Dynamic2G_working.txt	V1.1 02/02/2017
COM12_170202_172037_dynamic.ubx	(Results file) 02/02/2017
COM12_170202_172037_dynamic_stress_test.ubx	(Results file) 04/02/2017

The procedure implemented for the test simulates a real operation and can be summarized in the following steps:

1. Initialization of Master Station and Rover GNSS Receiver

For this test the Master station has been configured in “Survey-in” mode; In this configuration the station is placed in an unknown position. With the present configuration the Master station will start to send RTCM correction to Rover when the following 2 conditions are contemporary met:

- ✓ Observation time > 300 seconds;
- ✓ Mean 3D Survey < 2.0 meters (stdDev)

The “Fixed Mode” configuration is also available on M8P u-blox GNSS, but not used so far in the tests because it requires the knowledge at decimetric level of a given Ground Control Point where to place the Master Station Antenna Center of Phase

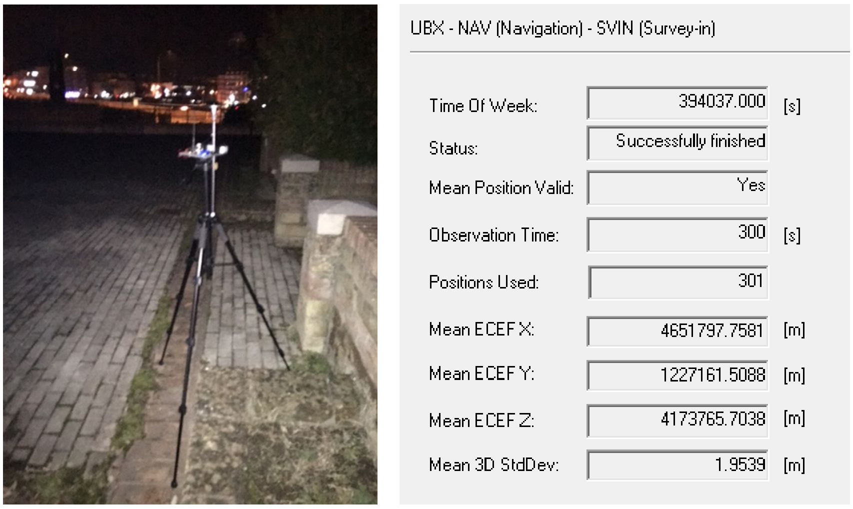

Figure 7-31: – Master Station in Survey-in mode during test

In the same way the RPAS has been placed on a marked point (about 2 meters away from the Master station) and the GNSS Receiver has been switched on few seconds after the Master station.

Figure 7-32: – RTK Rover receiver integrated on RPAS during initialization phase

In about 7-8 minutes (2-3 minutes after float solution achieved) the RPAS resulted "ready to fly" after the pilot has checked the real time visual feedback (solid green led) indicating "fixed mode" for Rover; this result has been confirmed also during data post processing analysis.

Float Solution has been also registered, but only during initialization phase.

2. Start Simulation of mission

The RPAS has been moved manually by a person over a pre-planned course; the site selected is close to TopView laboratory inside "University of Sannio" (Benevento - Italy). The test has been executed in "open sky" with no obstacle above 20° of elevation from the home point of testing.

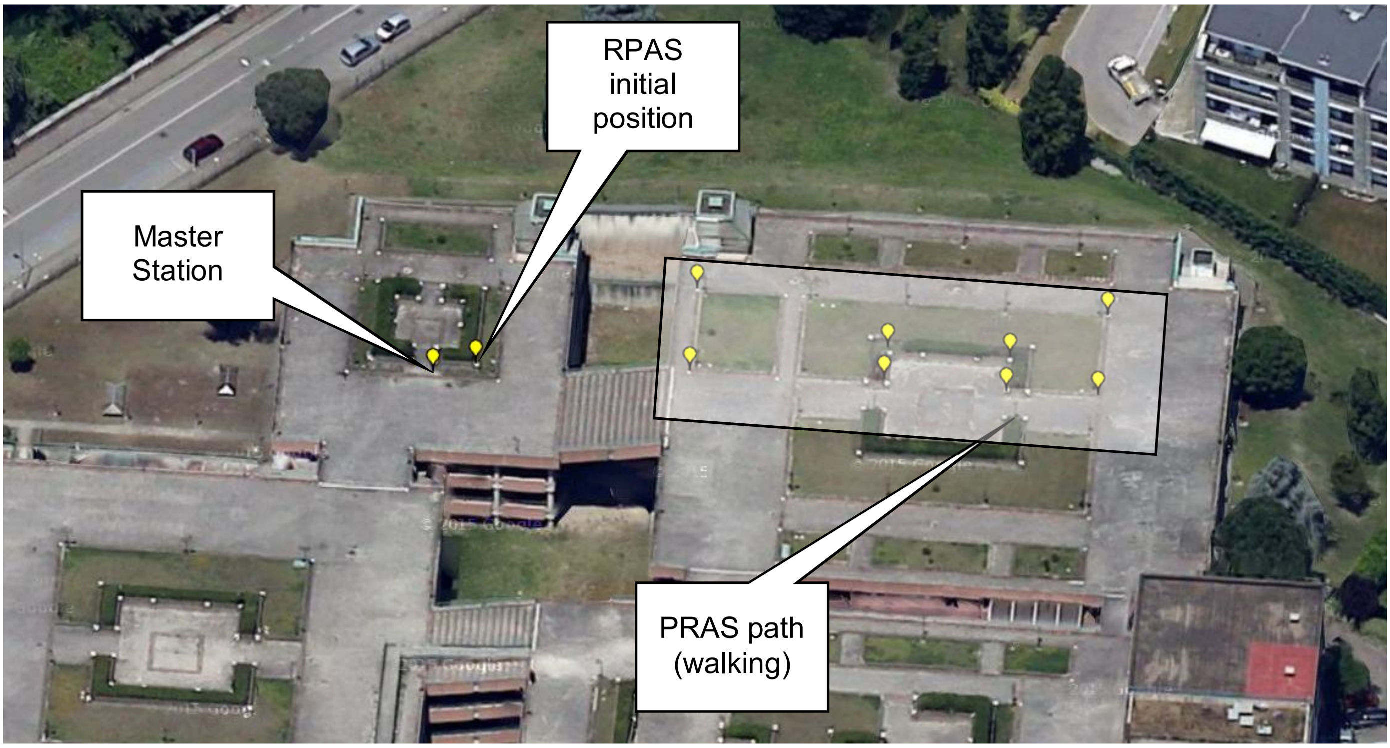

Figure 7-33: – Pre planned path for the test

In the figure are reported the Master station position, the initial position of RPAS and the points of the path walked.

The drone has been moved by a person on a straight line, following terrain constraints and garden's shapes, with the antenna center of phase as much as possible aligned to the lines. This has been done to eventually georeference in the future (by means of another measurement system) the points marked for a more accurate accuracy analysis in the next months with the data already logged and stored for this test.

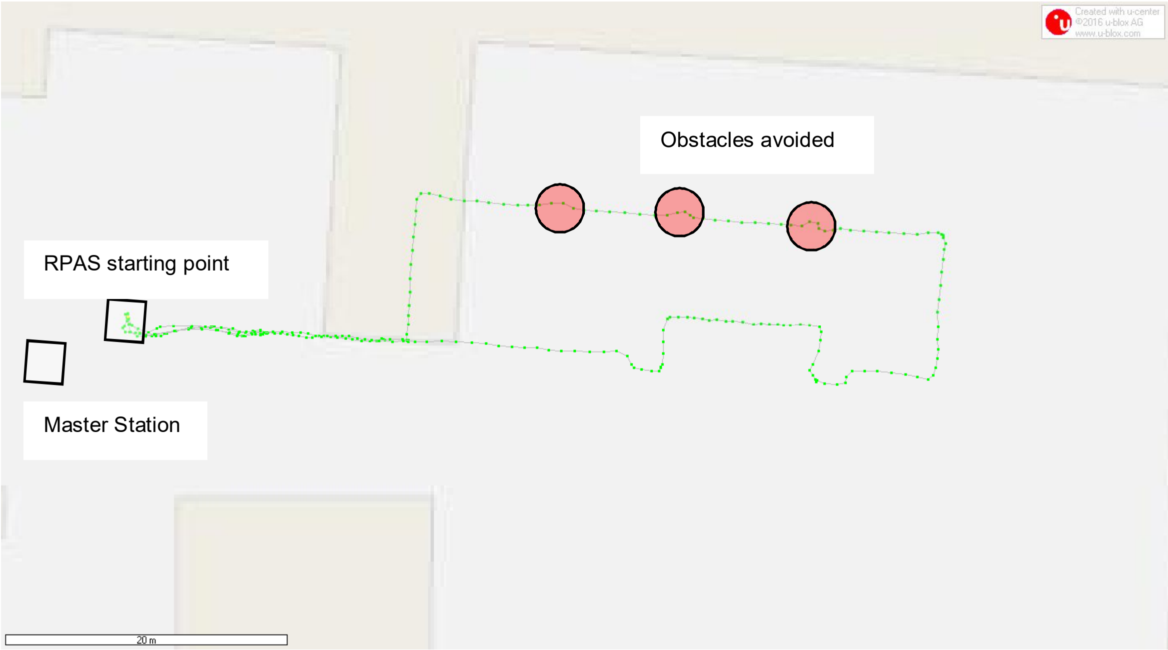

Figure 7-34: –recorded path of the test from post processing analysis

The second part of the test has been performed in another session with a different configuration in order to test "stress conditions" (e.g. higher velocity and distance).

Figure 7-35: –Initialization phase of Rover and Master during dynamic baseline stress test

The Rover antenna has been mounted on the top of a car and a path of roughly 1 km has been driven.

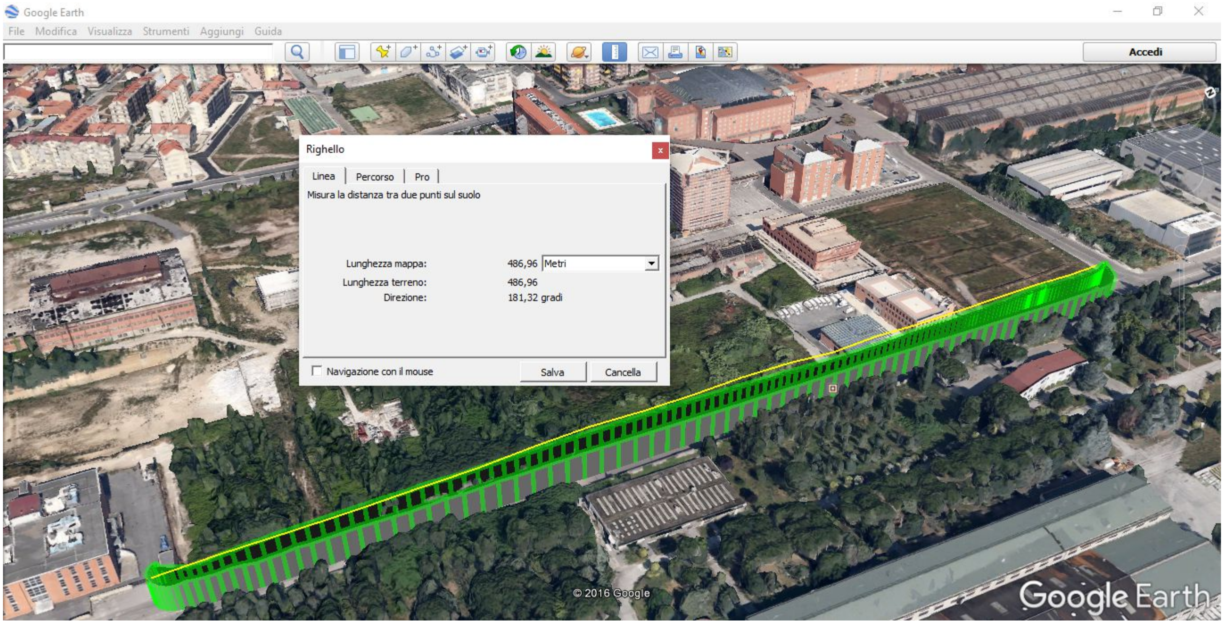

Figure 7-36: –Path driven by car for the dynamic baseline stress test

The maximum distance achieved has been about 485 meters with a measured speed of 30 km/h (about 8,3 m/s). During the whole test the RTK fixed solution positioning has never been lost. This data has been confirmed even during post processing data analysis.

7.5.5.3 Final Results

From this test, the team acquired different significant indicators. In fact, from our experience on field we understand RTK initialization is quite fast and the convergence time for a valid fixed solution of the rover is about roughly 6-7 minutes with the configuration provided and with an initial short distance (2 meters) from the Master Station to the Rover. The distance is representative and compliant to the operational procedures of EASY-PV application to minimize time of the inspections on field. The result is also remarkable for EASY-PV operations.

Main tests results are:

- ✓ No single outage of fixed solution has been reported in these tests;
- ✓ Initialization period is compliant to operations
- ✓ It is expected a decimetric accuracy in dynamic conditions, but this result shall be confirmed with a more rigorous test and with longer times of observations

In particular, it is noteworthy that we observed a 100% availability of RTK fix. According to theoretical indications, we argue that we should expect a centimetric accuracy. Further investigation are started to be provided in a dedicated test new test (see section 7.5.6)

7.5.6 TEST_GNSS.0060: RTK DYNAMIC SCENARIO (GNSS RECEIVER INSTALLED ON BOARD THE RPAS)

7.5.6.1 Objectives

The objective of this test is to thoroughly assess the positioning accuracy comparing single frequency ublox M8P and dual frequency North RTKite [RD 67] rover on-board RPAS that would hover at a velocity of about 1 m/s. Furthermore, this test would also assess the RTK fix quality in terms of RTK availability and effective baseline length to satisfy the EASPV accuracy requirement.

7.5.6.2 Activity Description

Both ublox M8P and RTK receivers are mounted on-board RPAS to generate a reference trajectory for the sake of performance comparison with the one obtained with ublox M8P rover. A block diagram of the RPAS payload for this test is shown in Figure 7-38.

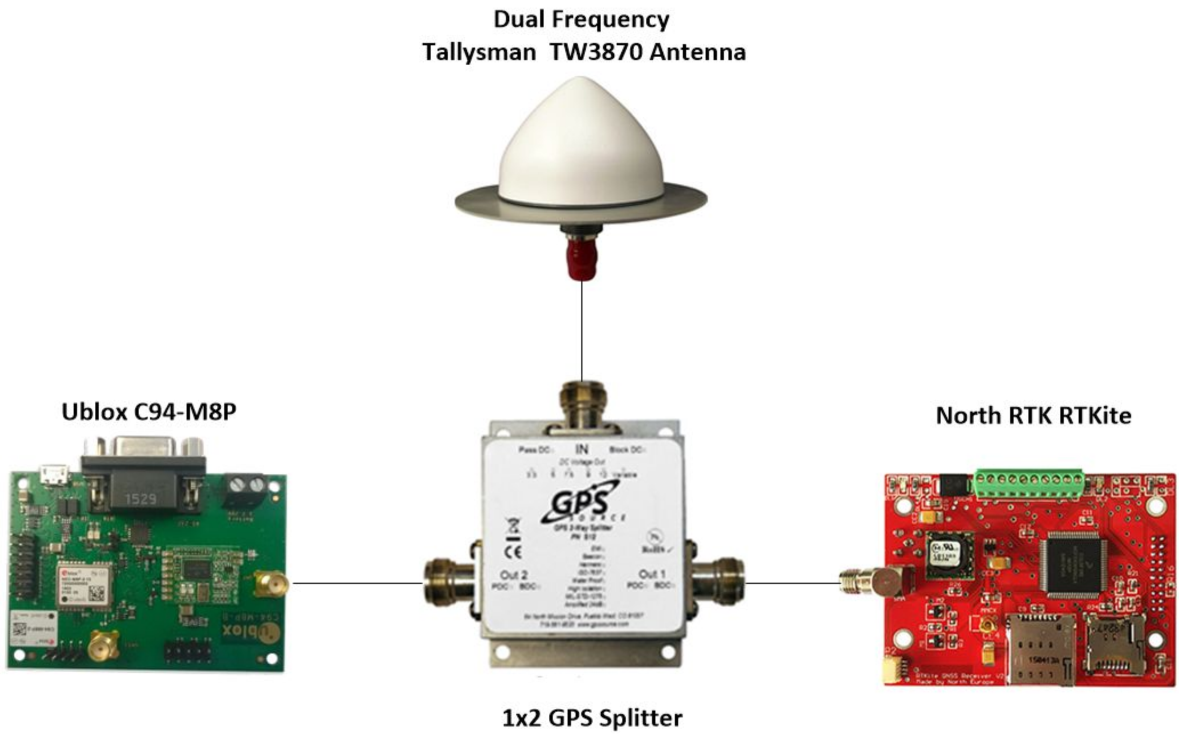

Figure 7-37: –RPAS Payload for the performance assessment of ublox M8P under dynamic conditions

As shown in Figure 7-37, 1x2 GPS splitter splits the signal from a common antenna, which is the dual-frequency Tallysman TW3870 patch antenna designed specifically for mobile RTK applications. The signal processed by ublox C94-M8P is L1-only as it's a signal frequency RTK receiver, whereas the signal processed by North RTKite receiver are L1 and L2.

7.5.6.3 Final Results

During the dynamic test campaign, raw measurement data is obtained from both the ublox and North RTKite receivers. The data is then processed using RTKPost utlility to generate the respective trajectories of the RPAS. To obtain RTK position fix, a nearby CORS station maintained by Regione Campagna is used as a base station.

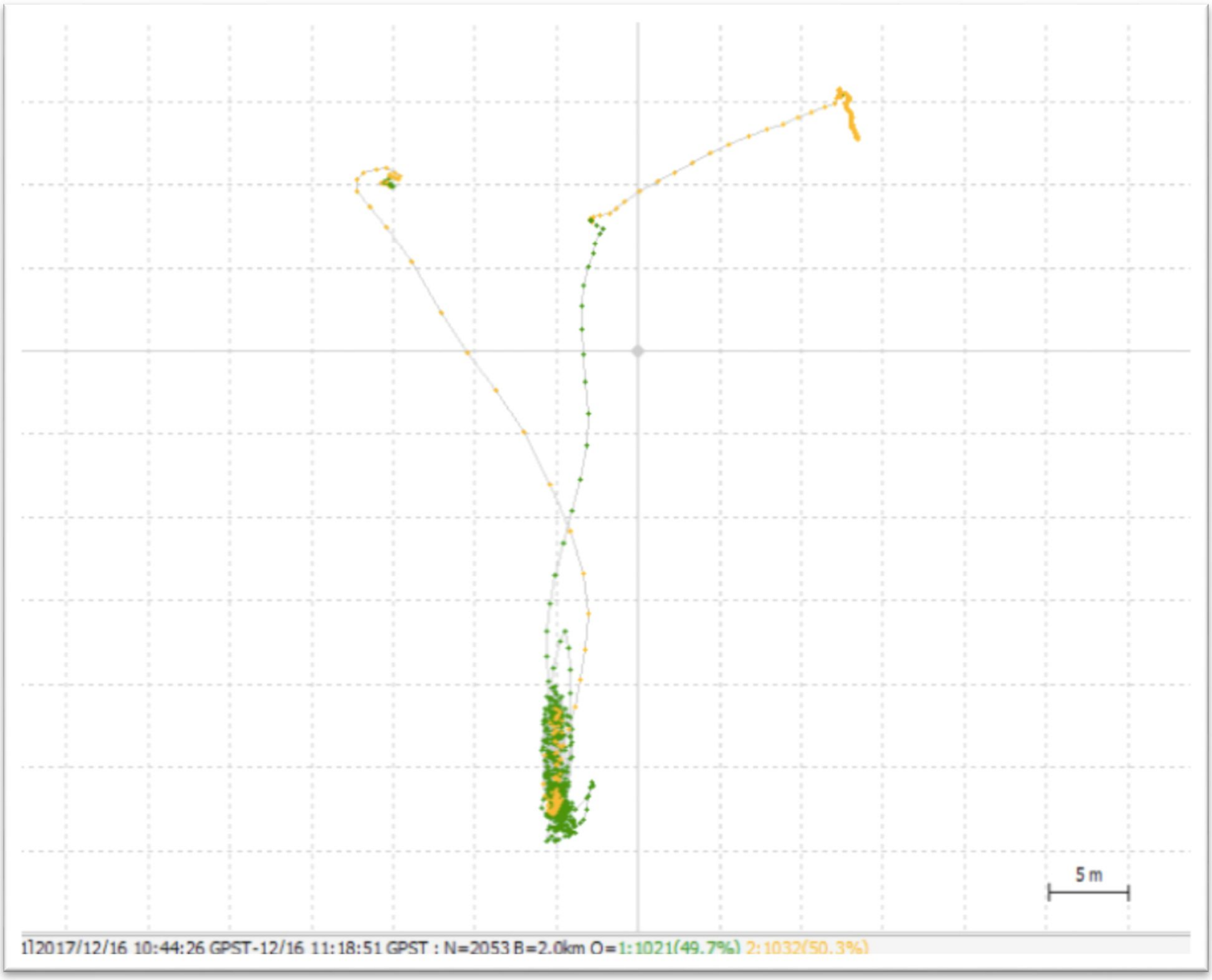

Figure 7-45: RPAS trajectory using C94-M8P

Figure 7-45 shows the RPAS trajectory obtained by processing the raw data of ublox C94-M8P. It can be observed at the bottom of the image that the RTK Fix positions (shown in green) are 49.7%, whereas the RTK Float Fix (shown in yellow) are 50.3%. One of the reasons for ublox M8P bad performance under dynamic condition could be the sensitivity of the carrier phase loops to measurement noise, which results in non-convergence to RTK Fix. The main reason of the measurement noise, such as multipath, is the drone body itself. A preliminary analysis covering this specific issue on the performance of ublox M8P on-board drone is reported at the end of this chapter.

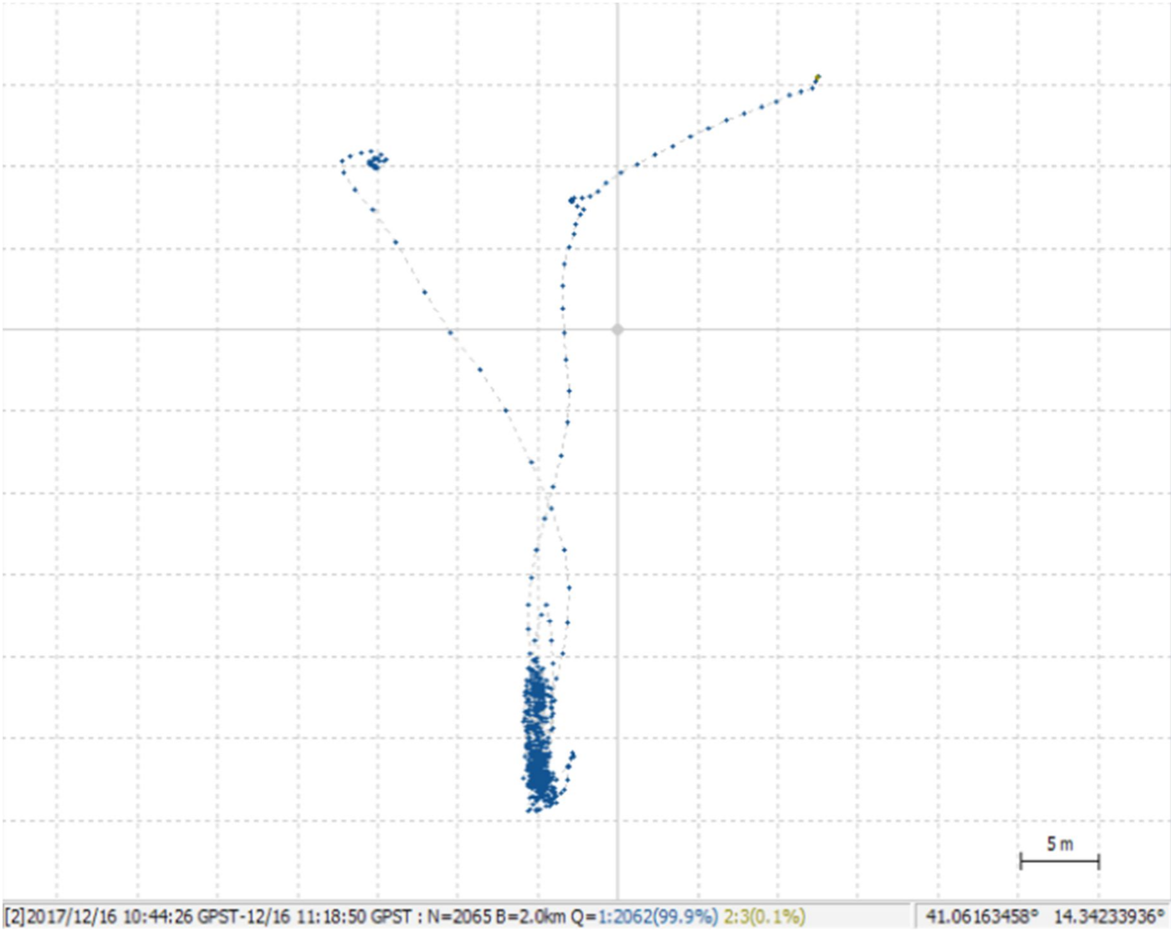

Figure 7-46: RPAS trajectory using North RTKite

In order to compare the RPAS trajectory obtained using ublox M8P with the reference trajectory, we first obtained the trajectory of RPAS using the North RTKite as shown in Figure 7-46, and finally we take the difference of the two trajectories as shown in Figure 7-47(b). It can be observed at the bottom of the image that the RTK Fix positions (shown in blue) are 99.9%, whereas the floating position fix (shown in yellow) are 0.1%. This shows the superior performance of the dual-frequency North RTKite receiver.

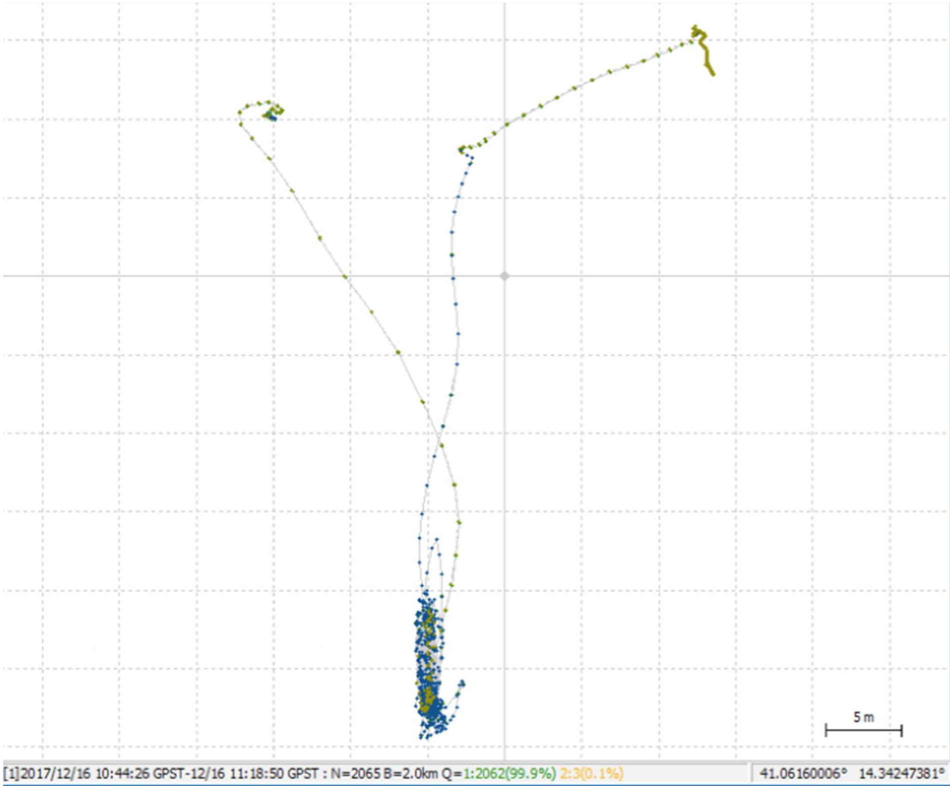

(a)

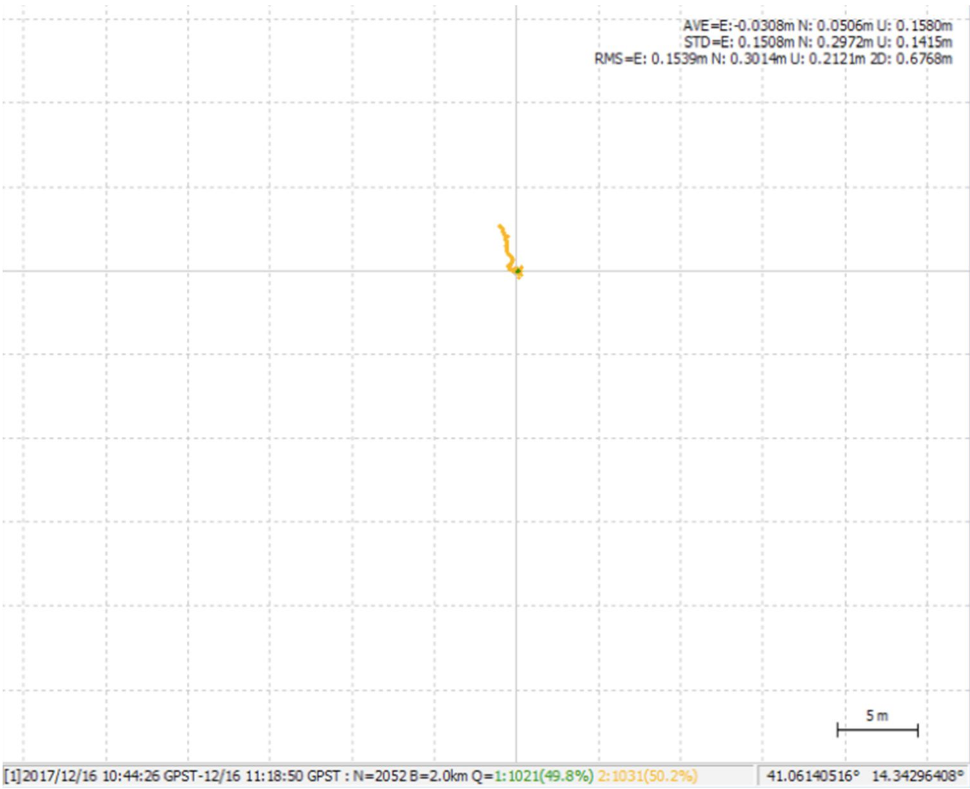

(b)

Figure 7-47: (a) RPAS trajectories from ublox and North RTKite on top of each other. (b) Difference of the two RPAS trajectories. .

Figure 7-47 shows that the difference between ublox and North RTKite trajectories. The difference of the trajectories is 2DRMS 67.68 cm, which is yet comparable (even greater) to the end to end accuracy.

Moreover, for sake to completeness, a further stressing test is performed to provide further evidences about quality comparison between Ublox M8P and North RTKite

Such receivers are then compared in static conditions on-board drone placed in the ground to simulate a noisy environment (above all in terms of multipath) also considering a limited dimension of the antenna ground plane used in order to cope with available dimensions. The same configuration given in Figure 7-45 is used. The raw data is recorded from both the receiver and processed by RTKPost utility The Regione Campania CORS is used as a base station (baseline of about 1 km). The drone is at placed as shown in Figure 7-48 to acquire data for about 15 minutes.

Figure 7-48: RPAS in static condition. ublox M8P and North RTKite receivers are installed on RPAS following the configuration shown in Figure 7-45.

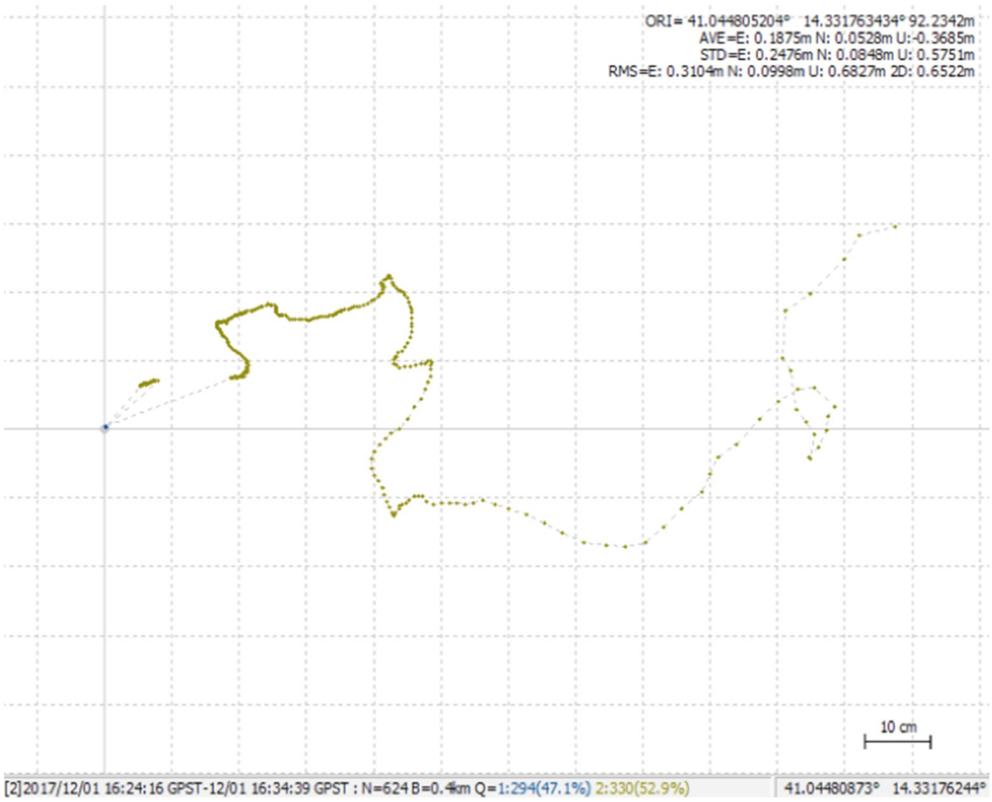

Figure 7-49: Ublox M8P position fixes under static conditions while installed on RPAS.

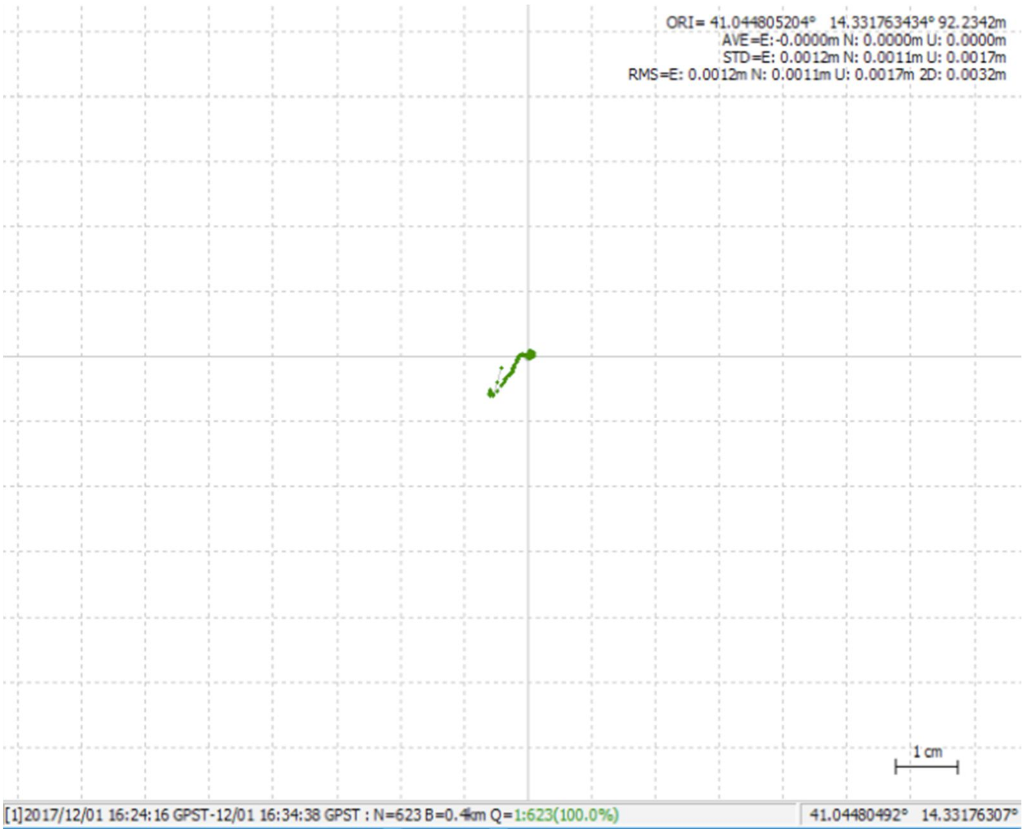

Figure 7-50: North RTKite position fixes under static conditions while installed on RPAS.

Figure 7-49 shows the positioning performance of ublox M8P under static conditions. It can be observed that the RTK Fix position (in blue color) percentage is 47.1, whereas the float position fix (shown in yellow color) is 52.9. The 2DRMS positioning accuracy is 65.22 cm, which is higher than the overall accuracy requirement of EASY-PV. The position performance of North RTKite is shown in Figure 7-50. It can be observed that North RTKite position performance is by far superior with 100% RTK Fix position providing the 2DRMS positioning accuracy of 0.3 cm.

The performance degradation in the ublox M8P is due to the measurement noise, such as multipath, from the RPAS body. The measurement noise can be somehow reduced either by installing a bigger ground plane or a high-performance antenna with integrated ground plane. This, however, is not feasible due to the deployment constraints, such as size and weight, on the RPAS.

Finally, based on the above session, we argue that lower cost to be afforded to buy the ublox M8P cannot be accepted to cope with EASY-PV solution; on the contrary a reasonable choice (also considering market aspects described in section 5) should be the dual-frequency North RTKite receiver instead.

7.5.7 RECOMMENDATION FOR GNSS SOLUTION TO BE ADOPTED IN EASY PV SOLUTION

A performance assessment of high accuracy receivers in terms of positioning accuracy has been performed. Indeed, the limited availability relevant to CORS networks suggests to employ RTK with privately owned base station and rover configuration. Figure 7-38 depicts one of the recommended RTK approaches for EASY-PV. As shown, privately owned base station and rover using RTK receiver equipped with patch antenna with ground planes shall be used for centimetre-level positioning of RPAS. The RTK correction would be transmitted either using UHF radios or UMTS/HSPA modem. The base station coordinates would be estimated a first time using survey-mode functionality offered by the base station software, which allows the base station receiver estimate its position considering averaging over several hundred epochs, typically 300. Further acquisitions will be performed in Fixed-mode paying attention to place the master antenna at the same physical position and to configure it with the same geographical position used in the first acquisition performed in survey-mode.

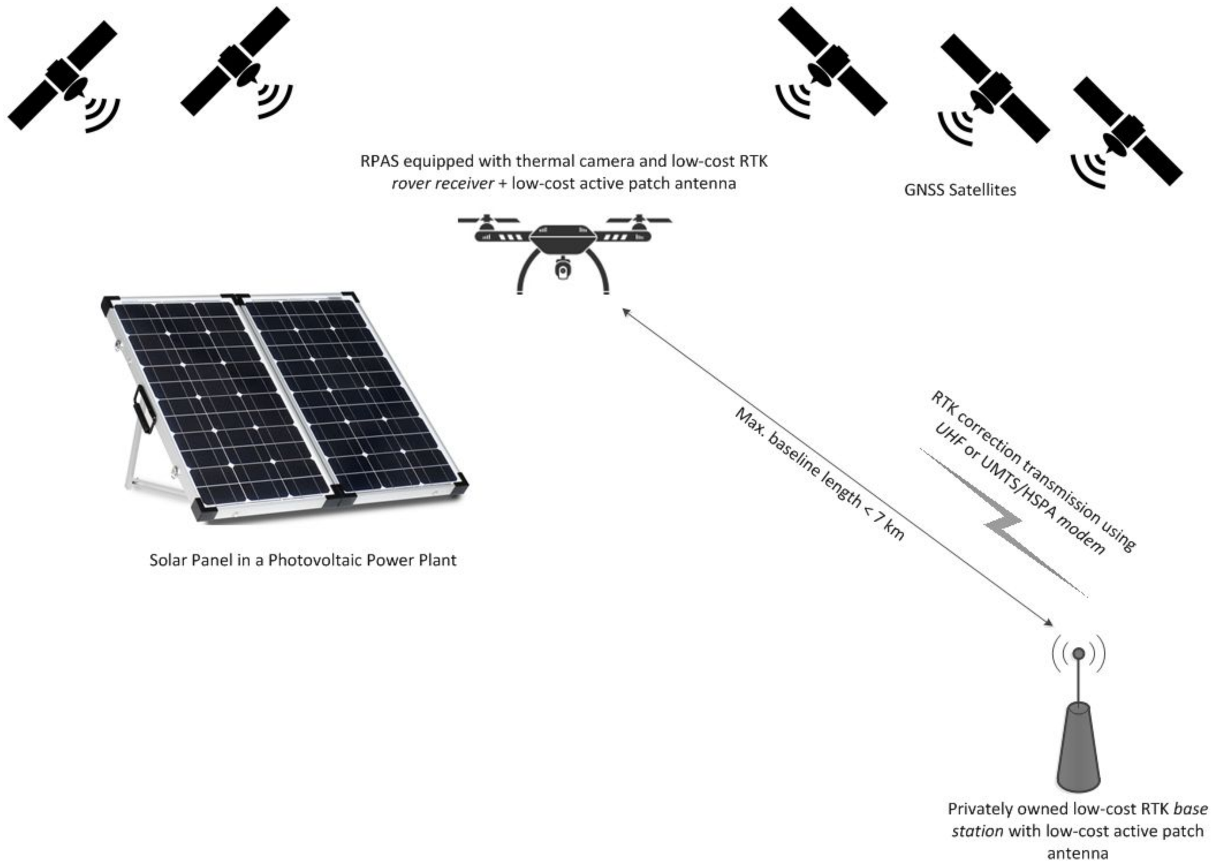

Figure 7-38: Proposed RTK privately owned base and rover set up for EASY-PV

Several tests have been performed to evaluate the correct receiver selection by performing a trade.off in terms of performances and costs. Considering the evolving market, along eth the last phase of the project two multi constellations receivers were selected to be compared: single frequency ublox M8P and dual frequency North RTKite.

Based on the above session, we argue that lower cost to be afforded to buy the ublox M8P cannot be accepted to cope with EASY-PV solution; on the contrary, a reasonable choice (also considering market aspects described in section 5) should be the dual-frequency North RTKite receiver instead.

7.6 END TO END ALGORITHM PERFORMANCE

Following table summarises theoretical deductions and experimental activities outcomes for each identified source of errors.

Error Sources		Value	Notes
Image center geo referencing	GNSS Receiver Precision Positioning	Order of 1 cm in static condition	2DRMS positioning accuracy of 1 cm is experienced, RTK dual frequency in static conditions. See section 7.5.6.
	RPAS velocity	Worst case 10 cm	The RPAS Ground Speed is typically 1 m/s. GNSS receiver is sampling at 10Hz. This implies that in worst case scenario even an offset of 10 cm can be experienced
Nadiral acquisition constraint	Gimbal Accuracy	Order of 1 cm	Combined Pitch and Roll estimated with about 0.05° of accuracy (worst case). It causes an acceptable error in horizontal 2D accuracy when considering the drone flying at 10 meter altitude of about 10m*sin(0,05°)=1 cm. See section 6.2 also confirmed by test reported in section 7.2.1
GSD evaluation In remote sensing, ground sample distance in a digital photo of the ground from air or space is the distance between pixel centers measured on the ground. For example, in an image with a one-meter GSD, adjacent pixels image locations are 1 meter apart on the ground.	Height and Inclination PV Modules (non coplanarity)	Less than 5 cm at altitude of 10m	Using panel dimension information, it is also possible to evaluate GSD not dependent from RPAS height. Test reported in section 7.1 confirmed the feasibility of the approach.
	Height of the drone: altimeter resolution		
Sensor Lens performances	Focal length distortion	Less than 5 cm	Cameras are used after calibration process. Considering these operational configurations, error are order of several cm are expected See section 6.3 and 7.3.

Error Sources		**Value**	**Notes**
Computer vision algorithm performances	Algorithm quantization	Less than 5 cm	At a given RPAS height of 20 meters from panel, the resolution of 1 pixel is given by the dimension of the rectangular swath on ground and the resolution of the sensor: δ_w=(24,04 m)/(640 pixel)=3,7 cm/pixel δ_h=(19,40 m)/(512 pixel)=3,8 cm/pixel
	Analysis of computational load	No impact	No major impact experienced

Table 14 end to end algorithm performance

The above table **doesn't take into account how the quality of functionality of computer vision algorithm in performing recognition and detection.** Indeed, vertices of panels may be also recognised in wrong positions causing a potential effect in geo-referencing error.

As a conclusion of this analysis, we may state the end to end global error is limited, even considering the worst case conditions. However, a definitive confidence about reaching the overall precision requirement may be achieved by only performing an end to end test where for a given panel identified in a picture a position is univocally evaluated. This test is performed in [RD 10], document which includes tests on actual EASY-PV equipment (see TEST_EASY.0070)

8 CONCLUSIONS

The document provides a detailed explanation of the GNSS core algorithm, augmented by Computer Vision techniques for the automatic recognition of PV panels and thermal anomalies.

The detailed mechanism and design has been tailored on both user's needs analysis provided in [RD 7] and operational needs gathered from pilots already involved in manual inspection with RPAS on large PV plants.

A particular emphasis has been devoted to GNSS as deemed as the key enabling technology.

Various GNSS technological solutions for centimetre-level accuracy are discussed in this document. These GNSS performances are requested in order to fulfil SR-0210 as reported in [RD 8]. Indeed, GNSS error source is only a component to be considered in the final error budget s reported in annexed note "End to end EASY-PV algorithm".

A market survey of OEM manufacturers and service providers has been provided offering a wide range of GNSS receivers and services to enable high accuracy GNSS solutions. Two distinct GNSS positioning methodologies – PPP and RTK - offer decimetric-level accuracy, which allows to fulfil SR-0210 as reported in [RD 8].

Among the existing methods and receiver configurations two potential solutions are analysed as deemed more economically viable:

- ✓ Privately owned RTK base and rover.
- ✓ CORS as a base station and RTK as a rover.

Anyway, CORS network exhibits problems in terms of availability, so that private solution is deemed as the more appropriate configuration although it requests an initialisation period before usage to allow the rover to achieve decimetric accuracy.

After providing a theoretical approach with detailed focus on GNSS and computer vision, some critical items have been tested before in order to be confident about the EASY-PV algorithm implementation along with the development phase.

As a final result, a summary table has been reported based on theoretical deductions and experimental activities outcomes aiming at identifying major error sources and relevant impact. Every contribution is deemed as limited to centimetric value so that, even though the quality of computer vision algorithm in performing recognition and detection has not been measured, we may presume that the overall accuracy requirement may be achieved using dual frequency and robust receiver. However, only performing a dedicated end to end test a final statement can be claimed. This test is performed in [RD 10], document which foresees tests on actual EASY-PV equipment including usage of North RTKite receiver.

END OF DOCUMENT